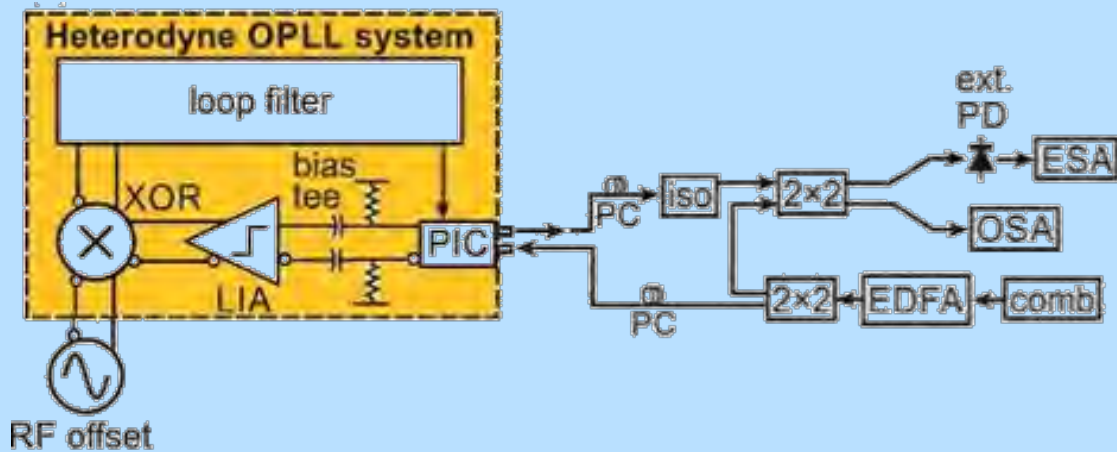


Research in Optoelectronics (A)



2016 Reprints of
Professor Larry A. Coldren
and Collaborators

ECE Technical Report 17-01
Department of Electrical & Computer Engineering
University of California, Santa Barbara

Research in Optoelectronics (A)

Reprints published in 2016

by

Professor Larry A. Coldren

and Collaborators

Published as

Technical Report # ECE 17-01

of

The Department of Electrical & Computer Engineering

The University of California

Santa Barbara, CA 93106

Phone: (805) 893-4486

Fax: (805) 893-4500

E-mail: coldren@ece.ucsb.edu

<http://www.ece.ucsb.edu/Faculty/Coldren/>

Introduction:

The attached contains papers published by Professor Coldren and collaborators in various journals and conferences in calendar year 2016. Any publication on which Prof. Coldren is named as a co-author is included. The work has a focus on III-V compound semiconductor materials as well as the design and creation of photonic devices and circuits using these materials. The characterization of these devices and circuits within systems environments is also included.

As in the past, the reprints have been grouped into several areas. This year these are all within the **Photonic Integrated Circuits** (PICs) category. Subcategories called out are *A. Reviews of Applications*, *B. SOAs and Phase-Sensitive Amplifiers*, and *C. Signal Processing with Active Micro-ring Filters*.

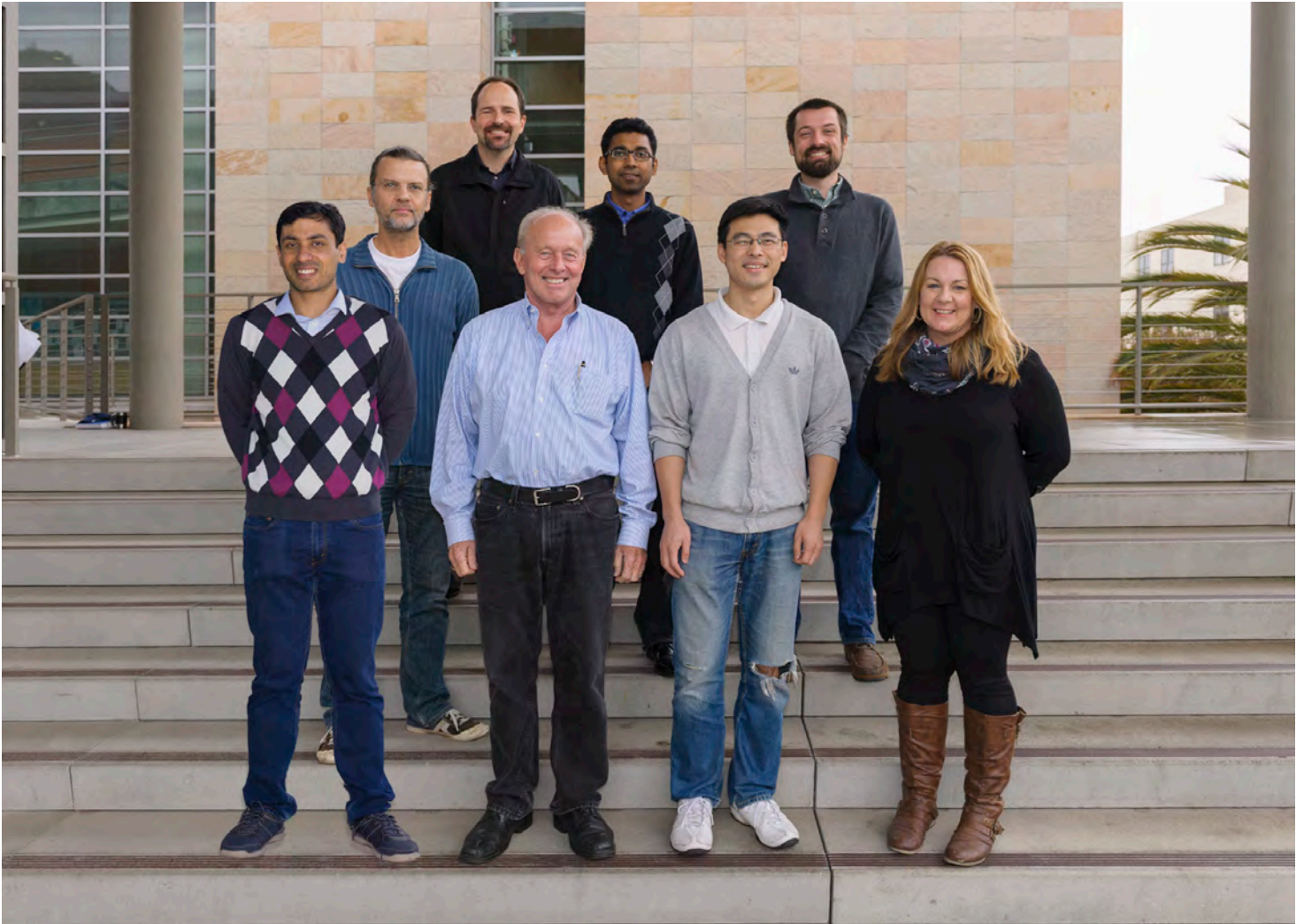
The work was performed with funding from a couple of federal grants, some gift funds from industry, and support from the Kavli Endowed Chair in Optoelectronics and Sensors. Some of the PIC work was funded by the MTO Office of DARPA via a subcontract from UC-Davis and a GOALI from NSF together with support from Freedom Photonics. The PIC fabrication was performed in the UCSB Nanofab facility partially supported by the NSF.

Sub-section (A.) contains three invited conference papers. The first discusses progress toward accurate optical frequency synthesis from both a DARPA and NSF project; the second outlines plans for coherent lidar using our PICs, based upon a new project with Lockheed Martin funded by DARPA; and the third summarizes the development of monolithic widely-tunable semiconductor lasers and their evolution into active PICs over the past 35 years. Slides from this latter presentation are included.

The second section (B.) contains two journal papers and a conference paper, all on semiconductor-optical-amplifiers (SOAs). The first journal paper and conference paper focus on the use of saturated SOAs as Phase-Sensitive amplifiers. The second journal paper gives an improved analysis of SOA characteristics, including an accurate semiconductor gain and carrier recombination modeling, saturation effects, and multi-wavelength mixing.

The third section (C.) contains two journal papers describing experiments with programmable active micro-ring filters that we constructed several years ago. The work was carried out in Prof. Yao's group at Ottawa. The *Nature-Photonics* paper discusses several signal processing experiments that were performed using energy storage in the rings to integrate signals. The second paper focused on an optical buffer based on self-pulsation in the active micro-ring.

Professor Coldren's Group



**Back Row: Leif Johansson, Milan Mashanovitch, Shamsul Arafin, Danilo Dadic
Front Row: Aditya Malik, Professor Larry Coldren, Wangzhe Li, Amanda Miller**

Professor Coldren's Group

I. Researchers

L. Johansson	Associate Research Engineer, UCSB
M. Mashanovic	Associate Project Scientist, UCSB
S. Arafin	Assistant Project Scientist, UCSB
W. Li	Postdoctoral Scholar, UCSB
A. Malik	Postdoctoral Scholar, UCSB

II. Students

D. Dadic	Graduate Student Researcher
----------	-----------------------------

III. Staff

D. Cohen	Principal Development Engineer, reports to Prof Nakamura
----------	--

A. Miller	Center Assistant, OTC
-----------	-----------------------

Collaborators

I. Faculty

J. Bowers	UCSB
M. Rodwell	UCSB
J. Yao	University of Ottawa
M. Li	China Academy of Science
A. Mecozzi	University of L'Aquila via Vetoio 1, L'Aquila, Italy
M. Vasilyev	University of Texas at Arlington
B. Yoo	UC Davis

II. Researchers

M. Lu	Infinera (former Postdoctoral Scholar)
E. Norberg Student)	Member of Staff, Aurrion, Inc. (former Graduate
J. Parker (former	Photonic Device Scientist, Freedom Photonics Graduate Student)
R. Guzzon	Photonic Systems Engineer, Aurrion, Inc.

III. Collaborating Students

C. Antonelli	University of L'Aquila via Vetoio 1, L'Aquila, Italy
W. Liu	University of Ottawa, Canada
Bruno Romeira	Eindhoven University of Technology, Netherlands

Table of Contents:

I. Photonic Integrated Circuits

A. Reviews of Applications

L. A. Coldren, M. Lu, John Parker, Leif Johansson, Shamsul Arafin, Danilo Dadic, and Mark Rodwell, "Toward Hz-level Optical Frequency Synthesis Across the C-band," *Proc. Integrated Photonics Research Conference (IPR)*, paper JM1A.2, Vancouver, British Columbia, Canada (July 18-20, 2016) INVITED 1

Paul J. M. Suni, John Bowers, Larry A. Coldren, and S.J. Ben Yoo, "Photonic Integrated Circuits for Coherent Lidar," *Proc. 18th Coherent Laser Radar Conference (CLCR)*, paper T12, Boulder, Colorado (June 26-July 1, 2016) INVITED 4

L. A. Coldren, "Thirty-five years of widely-tunable single-chip lasers: A pathway to active PICs," *Proc. International Semiconductor Laser Conference (ISLC)*, paper AWS11, Kobe, Japan, (September 12-16, 2016) INVITED (Slides included.) 10

B. SOAs and Phase-Sensitive Amplifiers

Wangzhe Li, Mingzhi Lu, Antonio Mecozzi, Michael Vasilyev, Shamsul Arafin, Danilo Dadic, Leif A. Johansson, and Larry A. Coldren, "First Monolithically Integrated Dual-Pumped Phase-Sensitive Amplifier Chip Based on a Saturated Semiconductor Optical Amplifier," *IEEE Journal of Quantum Electronics*, **52**, (1) pp. 1-12 (January 2016) 29

Cristian Antonelli, Antonio Mecozzi, Wangzhe Li, and Larry A. Coldren, "Efficient and Accurate Modeling of Multiwavelength Propagation in SOAs: A Generalized Coupled-Mode Approach," *Journal of Lightwave Technology*, **34**, (9) pp. 2188-2197 (May 2016) 41

Wangzhe Li, A. Mecozzi, M. Vasilyev, M. Lu, L. Johansson, and L. A. Coldren, "Investigation of an Integrated Photonic Dual-Pumped Phase-Sensitive Amplifier based on a Highly Saturated Semiconductor Optical Amplifier," *Proc. Conference on Lasers and Electro-Optics (CLEO)*, paper STh4F.3, San Jose, CA (June 5-10, 2016) INVITED 51

C. Signal Processing with Active Micro-ring Filters

Weilin Liu, Ming Li, Robert S. Guzzon, Erik Norberg, John S. Parker, 53
Mingzhi Lu, Larry A. Coldren, and Jianping Yao, “A fully reconfigurable
photonic integrated signal processor” *Nature-Photonics* **10**, pp. 190-195
(March 2016)

Weilin Liu, Bruno Romeira, Ming Li, Robert S. Guzzon, Erik J. Norberg, 60
John S. Parker, Larry A. Coldren, Jianping Yao, “A Wavelength Tunable
Optical Buffer Based on Self-pulsation in An Active Microring Resonator”
Journal of Lightwave Technology **34**, (14) pp. 3466-3472 (July 2016)

I. Photonic Integrated Circuits

A. Reviews of Applications

Toward Hz-level Optical Frequency Synthesis Across the C-band

Larry A. Coldren¹, Mingzhi Lu², John Parker³, Leif Johansson⁴, Shamsul Arafin¹, Danilo Dadic¹, Mark Rodwell¹

¹ECE Department, UC-Santa Barbara, Santa Barbara, CA 93106

²now with Infinera Corp, Sunnyvale, CA 94089

³now with Aurion Corp, Santa Barbara, CA 93117

⁴Freedom Photonics,LLP, Santa Barbara, CA 93117

coldren@ece.ucsb.edu

invited talk

Abstract: By using a stable comb as an input reference to an integrated heterodyne optical-phase-locked-loop consisting of a coherent receiver photonic IC with a widely-tunable laser, high-speed feedback electronics, and an RF synthesizer, accurate optical frequencies across multiple comb lines can be generated. Initial results will be presented.

OCIS codes: (250.0250); (250.5300); (250.5960); (250.3140)

Beginning with a single stable optical reference tone, it has been shown that a broad comb of lines with similar stability and linewidth can be generated. This has been done by phase locking one line of a mode-locked InP-based photonic IC laser to such a reference with an integrated high-bandwidth optical phase-locked loop (OPLL) [1]. Variations of the mode-locked laser (MLL) also contained a gain-flattening filter that broadened the optical comb into the multi-terahertz range [2]. This comb source is then used as a reference for a second heterodyne OPLL, which contains a widely-tunable laser that can be tuned across the C-band [3,4]. Tuning between comb lines is accomplished with a tunable RF synthesizer for offset locking. Two techniques of offset locking have been demonstrated: (a) the RF was applied to an optical modulator following the tunable laser and an optical sideband was used for locking [5]; (b) the RF was applied to an electronic mixer following optical detection in the heterodyne receiver and the RF difference frequency used for locking [6]. Figure 1 illustrates this system. In this case the MLL is also actively mode locked with a fixed f_{RF1} for more stability. The tunable frequency f_{RF2} is varied from a low value to at least half of the comb line spacing for full wavelength coverage.

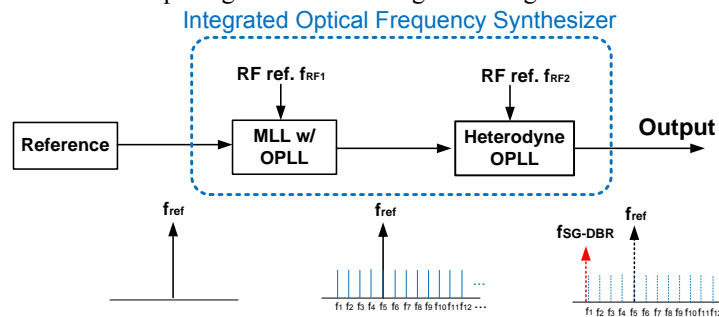


Fig. 1. Integrated optical frequency synthesizer system. The components within the dashed box could be on one chip, although initially they have been separate.

Figure 2 gives a schematic of the integrated MLL/OPLL using a ring MLL geometry along with results. Results from both a ring and linear MLL are shown, but only the linear MLL included the OPLL in the fabricated chips. The actively mode-locked ring MLL had about 70 useful comb lines spaced by 29.6 GHz. The electrical spectrum after detection shows a frequency deviation in the mode-spacing of < 10 Hz across ~ 2 THz with no phase locking. The linear MLL (24 GHz comb) after phase locking to a Rock laser (~ 200 Hz linewidth) shows no measurable center frequency deviations relative to the reference Rock laser (line is phase locked), but has a phase error variance of $< 0.12 \text{ rad}^2$ (integrated from 1 kHz to 10 GHz) and a relative linewidth for adjacent lines across the spectrum < 1 kHz. That is, the phase locked optical waves ‘wiggle’ back and forth a small amount, but never deviate by any significant fraction of π radians in phase from their proper value—standard deviation is $< 20^\circ$ over time periods of hours.

An alternative to the MLL/OPLL approach for stable comb generation is to use a self-referenced comb that does not require a reference tone. This involves the generation of an octave-wide comb, usually by nonlinear interactions in a high-Q resonator. A line from the low frequency end is frequency-doubled and phase-locked to a line on the high

frequency end of the same frequency by adjusting the parameters of the resonator. At this point the comb is ‘self-referenced’ and very stable [7].

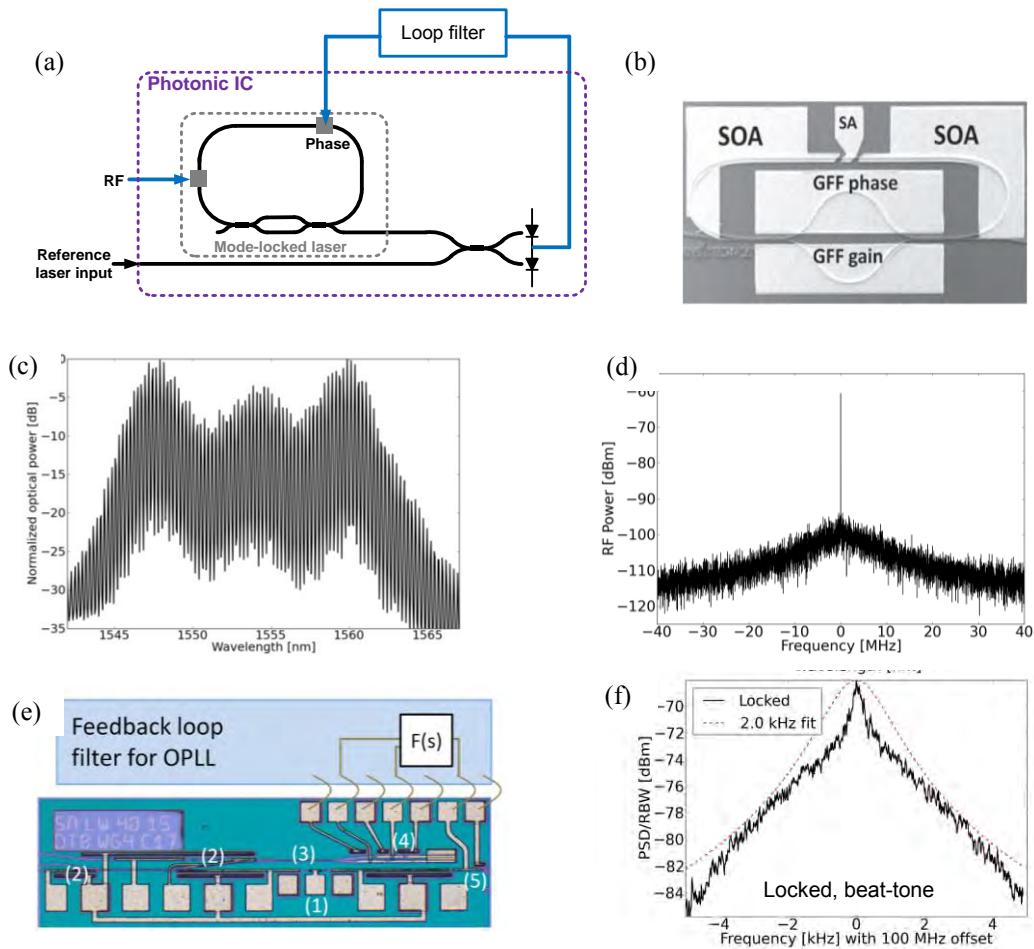


Fig. 2. (a) Comb generator schematic and results consisting of a MLL with OPLL. The double coupler geometry shown in the schematic can be used for gain flattening. RF is applied to an intensity modulator for active mode locking; the OPLL feedback is applied to a phase modulator to dynamically adjust the lasing frequency. (b) Photo of ring MLL with gain flattening filter (GFF). (c) Optical output of ring MLL. (d) Detected electrical spectrum of ring MLL. (e) Linear MLL/OPLL. (f) Detected electrical spectrum of linear MLL/OPLL. [1,2]

Figure 3 gives a schematic of the second heterodyne OPLL that accepts the input from the comb generator and provides a tunable optical output between comb lines. As mentioned in the first paragraph above the offset locking is achieved either with a tunable RF input to (a) an optical modulator following the integrated widely-tunable laser (SGDBR) or (b) an electronic mixer following detection in the feedback electronics. In either case, the procedure is to acquire lock to the difference frequency between the comb line and the RF line, and then tune the RF from a low value up to at least half way to the next comb line, where one can then use the opposite side band from the modulator or mixer from the next comb line and tune the RF down to near that next comb line.

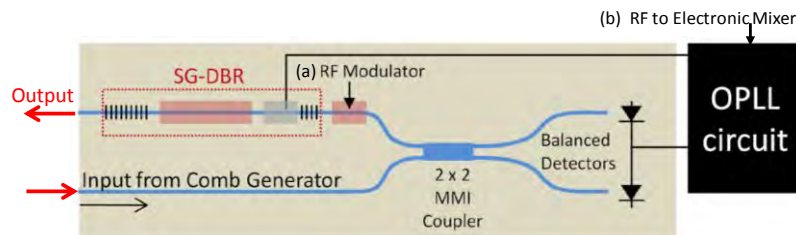


Fig. 3. Heterodyne OPLL with tunable RF offset locking of a widely-tunable laser to the generated comb.

The SGDBR also needs to be adjusted so that its center frequency is moved to the next comb line to repeat the process in order to avoid mode-hops. Then the process can be repeated across the entire comb. As shown in Fig. 2 relatively flat, strong combs extending over half of the C-band have already been accomplished, and it is anticipated that full C-band will be possible with these techniques.

The first experiments performed used a double modulator pulse carving configuration following an external-cavity laser with a ~ 100 kHz linewidth to generate a 40 GHz comb for use with the coherent receiver PIC and OPLL circuit illustrated in Fig. 3 [8]. The results are summarized in Fig. 4, where tuning across four comb lines is illustrated for a total of ~ 160 GHz. In this case a 4-photodiode I-Q coherent receiver was also employed instead of the simple 2-photodiode geometry illustrated in Fig. 3. Although the SGDBR laser unlocked had a linewidth >5 MHz, once locked, its linewidth 'cloned' that of the external cavity laser at ~ 100 kHz. No retuning of the SGDBR was used in order to illustrate how much tuning could be accomplished by only tuning of the phase tuning section from the feedback circuit.

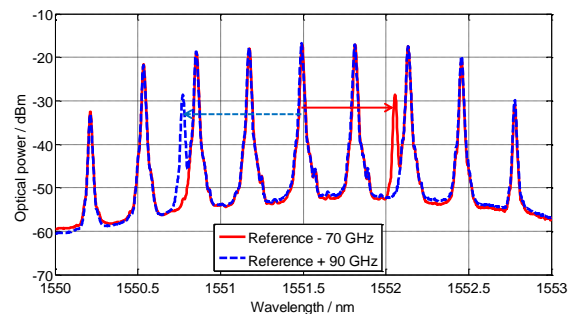


Fig. 4. Superposition of comb input and two output spectra from an optical spectrum analyser. Actual linewidths here ~ 100 kHz. The initial locking was to the central line at 1551.5 nm. Then, the SGDBR was tuned -70 GHz and $+90$ GHz to the output lines shown by using a 26 GHz synthesizer and tuning the sum and difference frequencies formed with the nearest comb lines to and away from them. [8]

References

- [1] J. Parker, et al, "Highly-stable integrated InGaAsP/InP mode-locked laser and optical phase-locked loop," *PTL* **25** (18) 1851-1854 (2013).
- [2] J. Parker, et al, "Integrated phase-locked multi-THz comb for broadband offset locking," *Proc. OFC*, paper OM3E.5, Los Angeles (2012).
- [3] M. Lu, et al, "Highly-integrated optical heterodyne phase-locked loop with phase/frequency detection," *Opt. Exp.*, **20** (9) 9736-9741 (2012).
- [4] M. Lu, et al, "A heterodyne optical phase-locked loop for multiple applications," *Proc. OFC*, paper OW3D.1, Anaheim (2013).
- [5] S. Ristic, et al, "An optical phase-locked loop photonic integrated circuit," *J. Lightwave Tech.*, **28** (4) 526-538 (2010).
- [6] E. Block, et al, "A 1-20 GHz all-digital InP HBT optical wavelength synthesis IC," *IEEE Trans. Mic. Theo. & Tech.*, **61** (1) 570-580 (2013).
- [7] T. J. Kippenberg, et al, "Microresonator-based optical frequency combs," *Science*, **332**, 555-559 (2011).
- [8] M. Lu, et al, "A highly-integrated optical frequency synthesizer based on phase-locked loops," *Proc. OFC*, pap W1G.4, San Francisco (2014).

Photonic Integrated Circuits for Coherent Lidar

Paul J. M. Suni^(a), John Bowers^(b), Larry Coldren^(b), S.J. Ben Yoo^(c)

(a) Lockheed Martin Coherent Technologies, Louisville, CO, USA

(b) University of California Santa Barbara, California 93106, USA

(c) University of California, Davis, CA 95616, USA

Lead Author e-mail address: paul.suni@lmco.com

Abstract: A decade ago integrated photonic devices typically consisted of single components that fulfilled one specific function, such as phase modulation or splitting into N beams. In the intervening years, photonic integrated circuits (PICs) have undergone a revolution in terms of component functions, loss reductions, and high level functional integration. This has in part been driven by the development of device designs compatible with conventional CMOS fabrication processes. We are now at a point where component diversity, low losses, and low cost fabrication enables us to consider development of coherent laser radar systems based around PIC technology. In this talk we will highlight some of the current developments in the PIC domain, with an emphasis on technology elements applicable to coherent laser radar systems. Examples include narrowband lasers, frequency shifters, beam distribution networks, and large angle photonic beam steering.

Keywords: Photonics, Photonic Integrated Circuits, PIC, Silicon Photonics, Coherent Laser Radar, Lidar, Ladar

1. Introduction

The reduction of optical devices to microscopic dimensions has been underway for decades in the form of fiber optics, CMOS detector arrays, and components like modulators, micro-ring filters, and splitters. The past decade has seen an explosion of development that goes beyond single devices and now encompasses subsystems and systems with hundreds of components [1-4]. The technology typically falls under the name of Photonic Integrated Circuits (PICs). Silicon Photonics is a form of PIC that uses silicon substrates and silicon waveguides for the platform. .

A key enabler in the silicon photonic revolution has been the development of technologies compatible with conventional CMOS fabrication processes and foundries. In an extraordinary coincidence the multi-billion dollar investments in CMOS foundries enable the same fabrication infrastructure to produce devices that propagate light at wavelengths ideally suited for many electro-optic communications and sensing applications. Low propagation losses (<0.5 dB/cm) in waveguide dimensions smaller than the wavelength (220 nm \times 300 nm cross-section for 1550 nm wavelength) have enabled integration of large numbers of components in small footprints. The large index step between silicon ($n_{\text{Si}} \sim 3.5$) and waveguide cladding materials like silica glass ($n \sim 1.45$) and silicon nitride ($n \sim 2$) enables tight mode confinement and small bend radii (<10 μm), while supporting low loss and low crosstalk between closely-spaced waveguides.

Silicon is excellent as a materials system for passive components, but is non-ideal for active components like laser sources and detectors. Fortunately heterogeneous integration techniques are maturing, whereby high-performance active components made using InP, GaAs, Ge, and other materials can be integrated with silicon.

In tandem with the development of optical devices, great progress is also being made in the integration of optics with CMOS electronics and efficient thermal management. Flip-chip bonding of PICs with CMOS

chips (also known as “2.5D” integration) is routinely done today and full 3D integration of complex photonic/electronic circuitry is undergoing rapid development [3]. These advances enables us to consider construction of lidar systems on a chip.

Figure 1 shows a generic coherent lidar architecture. Aside from the signal processor, the only functional element that has not been demonstrated in PIC form is a high peak power oscillator or amplifier, because of the peak power handling limits of small waveguides. Silicon photonics offers the possibility of fabricating complete coherent lidar systems at the chip level by tailoring components to lidar needs. Until high peak power systems are developed, perhaps based on large arrays of parallel coherent amplifiers, chip-based coherent lidar systems are likely to be developed around modulated CW architectures.

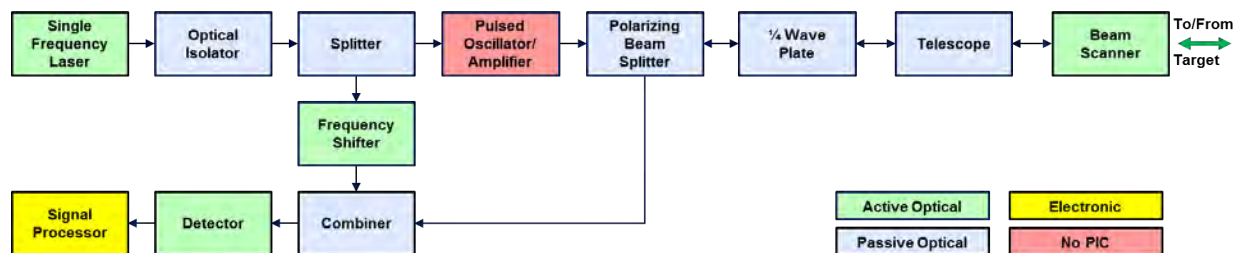


Figure 1. Generic coherent lidar architecture.

2. Device Examples

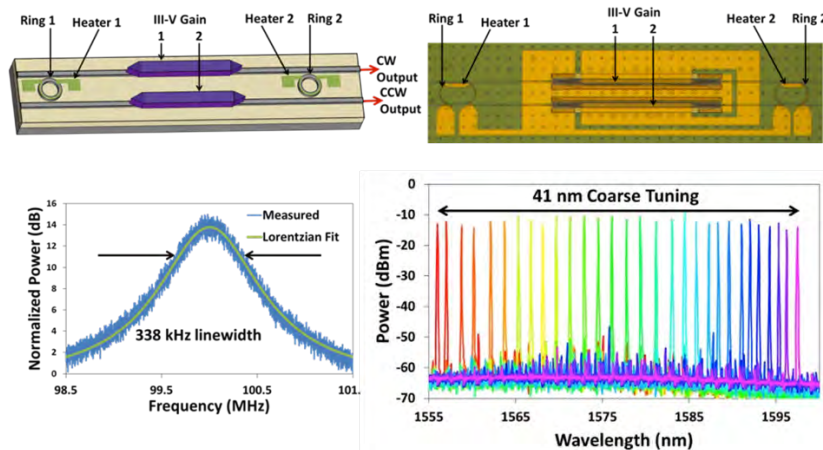
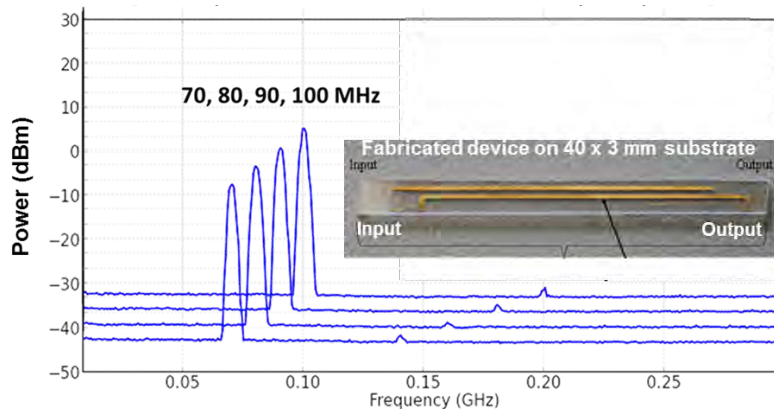


Figure 2. Laser with >40 nm tunability centered at 1575 nm [4].



For space reasons we only provide two examples of

relevant demonstrated devices. Figure 2 shows a laser developed at UC Santa Barbara comprising two gain elements [5]. Two thermally adjustable micro-rings are used in a Vernier configuration to enable >40 nm wavelength tuning with narrow linewidth and >35 dB side-mode suppression. The output power was >3 mW, which could be increased with on-chip semiconductor amplifiers (SOA) [6]. Other lasers demonstrated at UCSB include broadly tunable lasers with wavelength hopping and stabilization in 30 ns.

Frequency shifting is another important feature of coherent lidar systems as they are frequently used to generate intermediate frequencies (IF) and track out Doppler shifts. This is often accomplished using acousto-optic modulators (AOM), cascaded Mach-Zehnder interferometers, or by offset-locking two lasers. A conceptually very simple direct frequency shifter that emulates a rotating half-wave plate has recently been demonstrated [7] in LiNbO_3 at UC Davis – see Figure 3. Note the absence of the carrier frequency and ~ 40 dB suppression of the second harmonic. This device type is predicted to enable frequency shifting in excess of 10 GHz.

Many other important components also exist, including optical isolators with >30 dB isolation and 2.3 dB insertion loss [8], low-loss PIC to fiber couplers [9], and methods for writing low-loss 3D waveguides for routing [10]. Numerous additional examples of PICs can be found in reference [11].

3. Non-Mechanical Beam Steering (NMBS)

Beam steering is frequently a SWaP limiting factor in conventional lidar systems. Many means have been devised over the years to eliminate large, heavy, and slow gimbals, Risley prisms, and other steering devices. McManamon reviewed non-mechanical beam steering (NMBS) technologies in 2009 [12]. Silicon photonics is taking beam scanning to a new level by completely eliminating the need for bulk optics. The recent DARPA SWEEPER program developed multiple PIC-based NMBS systems. Figure 4 shows approaches by researchers at UC Berkeley [13] and MIT [14]. The Berkeley approach used MEMS ribbon arrays to on-the-fly reconfigure gratings which diffract light angularly, The MIT approach uses 2D arrays of phase shifters to steer beams by imposing transverse linear phase gradients. Both of these approaches demonstrated fast and efficient beam steering, but also revealed a scalability issue. To address N far field points in two dimensions the number of required controls grows as N^2 , which becomes very challenging as N becomes very large.

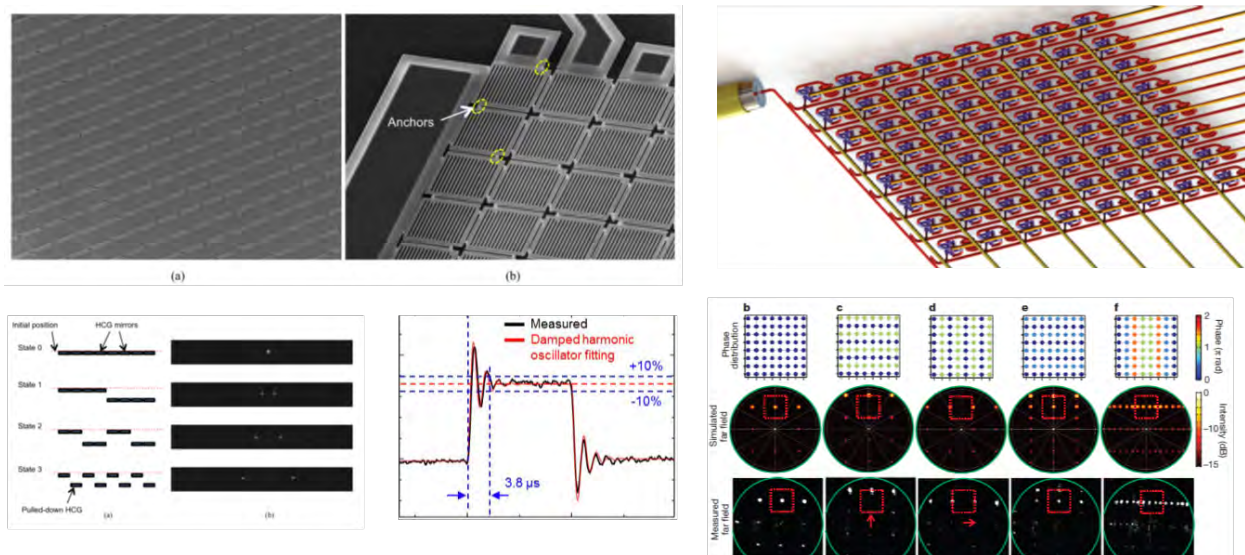


Figure 4. PIC-based NMBS demonstrated by UC Berkeley (left) using MEMS ribbon arrays and by MIT (right) using 2D arrays of phase shifters.

Figure 5 shows an alternative approach developed by UCSB [15,16]. In this approach laser tuning over ~ 43 nm combined with a fixed grating is used to steer beams in one dimension. Transverse phase gradients steer in the second dimension. This approach reduces the number of control elements to $N+1$, the 1 being the laser wavelength control.

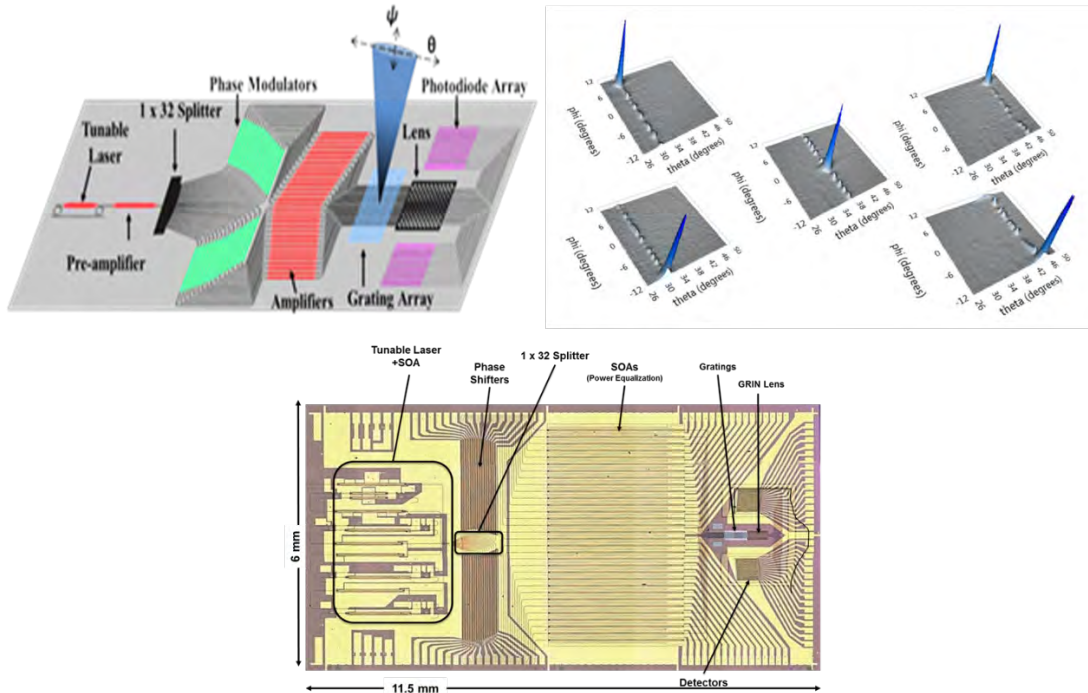


Figure 5. 2D NMBS approach developed by UCSB [15]. Top left – functional architecture. Top right – 2D beam steering demonstrated to date. Bottom – physical layout on 6×11.5 mm² chip.

4. Coherent Lidar Example

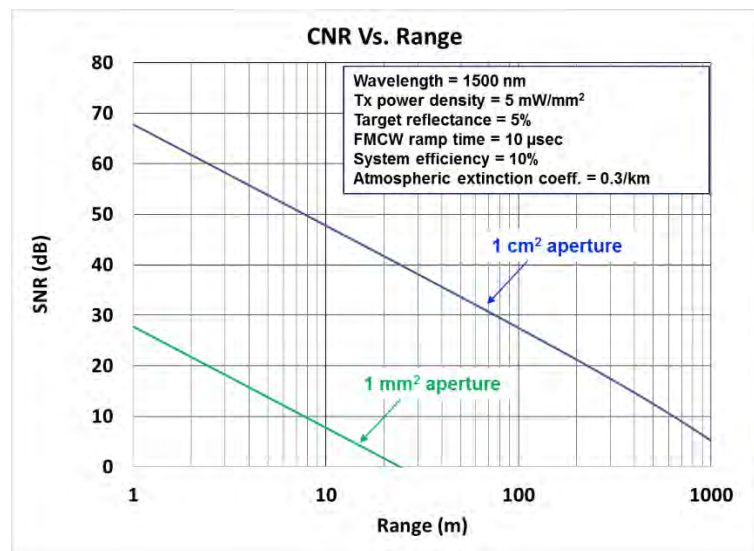


Figure 6. FMCW lidar CNR vs. range prediction for realistic sensing scenario at two aperture sizes with the same

Many versions of coherent lidar systems can be constructed as variations on the generic architecture shown in Figure 1. Frequency-modulated continuous wave (FMCW) operation is one approach to perform lidar functions like range finding at low peak powers and simple signal processing [17]. In this technique the laser frequency is ramped linearly in time and the time delay associated with the round-trip time to the target produces a beat signal with frequency proportional to range. Up-down frequency ramps can be used to unambiguously distinguish range and velocity. Figure 6 illustrates an example of the anticipated SNR achievable with a coherent FMCW single point sensor operating with a single shot measurement time of 10 μ s, i.e. up to 100 kHz data points per second rate. The green curve corresponds to a 1 \times 1 mm coherent transmit/receive aperture while the blue curve corresponds to a coherent 1 \times 1 cm aperture. Multi-point simultaneous sensing similar to that used in commercial 3D lidar instruments [18] can also be incorporated into the same chip. A non-mechanical steered single-chip sensor of this type could be constructed by incorporation of the technology elements described in this paper. As seen in Figure 6 such a sensor could provide rapid 3D mapping to km ranges with a modest \sim 1 cm² coherent aperture.

Looking into the future it is not far-fetched to envision future large aperture coherent lidar systems fabricated at low cost in very small form factors. These may incorporate all photonic components, the associated signal processing, as well as efficient heat removal. Development of such lidar systems is planned under programs like DARPA's Modular Optical Aperture Building Blocks (MOABB).

5. References

- [1] M. J. Heck, et al., "Hybrid Silicon Photonic Integrated Circuit Technology", IEEE J. of Sel. Top. In Quan. Electr, **19**, pp. 6100117 (2013)
- [2] Chong Zhang, et al., "2.56 Tbps ($8 \times 8 \times 40$ Gbps) Fully-Integrated Silicon Photonic Interconnection Circuit", Conference on Lasers and Electro-Optics (CLEO), San Jose, CA, USA (2016)
- [3] V. Stojanovic et al., "High-Density 3D Electronic-Photonic integration," in Fourth Berkeley Symposium on Energy Efficient Electronic Systems (E3S), pp. 1-2 (2015)
- [4] S. J. Ben Yoo, "Heterogeneous Photonic Integrated Circuits and Their Applications in Computing, Networking, and Imaging," Proc. SPIE 8988, Integrated Optics: Devices, Materials, and Technologies XVIII, 89881D (2014); doi:10.1117/12.2047106.
- [5] J. C. Hulme et al., "Widely Tunable Vernier Ring Laser on Hybrid Silicon," Opt. Express **21**, 19718-19722 (2013)
- [6] Michael L. Davenport, Sandra Skendzic, and John E. Bowers, "Heterogeneous Silicon/InP Semiconductor Optical Amplifiers with High Gain and High Saturation Power", Conference on Lasers and Electro-Optics (CLEO), San Jose, CA, USA; 5 - 10 June 2016
- [7] B. Ercan et al., "Optical Frequency Shifting in Electro-Optical Waveguides by Emulating Rotating Waveplates", *J. Lightwave Technology*, **33** (to be published, 2016)
- [8] D. Huang et al., "Silicon Microring Isolator With Large Optical Isolation and Low Loss", *Proc. Optical Fiber Conference*, OSA Publishing (2016), paper Th1K2
- [9] C. Lo et al. "CMOS-compatible High Efficiency Double-Etched Apodized Waveguide Grating Coupler", Opt. Expr., **21**, pp. 7868 (2013)
- [10] S. J. Ben Yoo et al., "Heterogeneous 2D/3D Photonic Integrated Microsystems" invited paper to appear in Nature Microsystems and Nanoengineering (2016)
- [11] L. Chrostowski and M. Hochberg, "Silicon Photonics Design: From Devices to Systems", Cambridge University Press (2015)
- [12] P.F.McManamon e al., "A Review of Phased Array Steering for Narrow-Band Electrooptical Systems", Proc. of the IEEE, **97**, PP. 1078 (2009)

Anniversary Workshop Speakers



Thirty-Five Years of Widely-Tunable Single-Chip Lasers: A Pathway to Active PICs

Prof. Larry A. Coldren

(Univ. of California, Santa Barbara, USA)

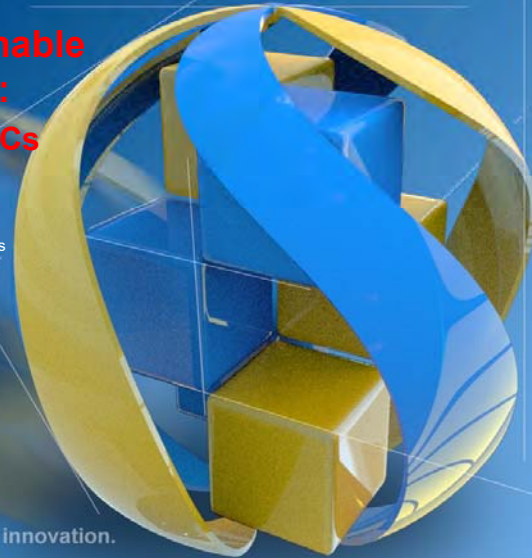
Larry A. Coldren is the Fred Kavli Professor of Optoelectronics and Sensors at the University of California, Santa Barbara, CA. He received his Ph.D. in EE from Stanford Univ. and spent 13 years in research at Bell Labs before joining UCSB in 1984, where he holds appointments in the ECE and Materials Departments. He served as Dean of Engineering at UCSB from 2009-2011. In 1991 he co-founded Optical Concepts, acquired as Gore Photonics, to develop novel Vertical-Cavity Surface-Emitting Laser (VCSEL) technology; and in 1998, Agility Communications, acquired by JDS-Uniphase, to develop widely-tunable integrated optical transmitters.

He has authored or co-authored over a thousand journal and conference papers, including numerous plenary, tutorial and invited presentations. He has co-authored 8 book chapters and two textbooks, including the most used text on Diode Lasers and Photonic ICs in circulation today. He has been issued 65 patents and is a recipient of several awards, including the John Tyndall, Aron Kressel, David Sarnoff and IPRM Awards. He is a Life Fellow of the IEEE, and a Fellow of the OSA and IEE as well as a member of the National Academy of Engineering.

**35 years of widely-tunable
single-chip lasers:
a pathway to active PICs**

Larry A. Coldren

Fred Kavli Professor of Optoelectronics and Sensors
ECE and Materials Departments
UCSB



The convergence of research and innovation.

- **Early tunable laser results**
 - vernier-tuned coupled-cavity lasers
 - DBRs
 - SGDBRs (vernier-tuned DBRs)
- **Other widely-tunable laser designs**
- **Recent advances**
- **Photonic ICs developed from (and including) tunable laser technology**
- **Heterogeneous Integration**

UC SANTA BARBARA
engineering
The convergence of research and innovation.

Single-frequency laser

- Change m, n or L to tune λ

Mirror-1 Gain Medium Mode Selection Filter Mirror-2 Output

$m\lambda/2 = nL$

Gain Spectrum Lasing Mode Mode Selection Filter Cavity Modes

λ

UC SANTA BARBARA
engineering
The convergence of research and innovation.

Distributed Bragg Reflector Laser

Mirror-1 Gain Medium Mode Selection Filter Mirror-2 Output

$m\lambda/2 = nL$

4

UC SANTA BARBARA
engineering
The convergence of research and innovation.

Coupled-Cavity Vernier Tuning

- Tune n_1 or n_2 to tune wavelength location of reinforced modes
- Also possible with coupled ring cavities
- Can provide enhanced AM or FM capability (ISLC '84)

Next: Combine vernier tuning with DBR mode selection and continuous tuning?

$\Delta\lambda = \frac{\lambda^2}{2n_1L_1}$
 $\Delta\lambda = \frac{\lambda^2}{2n_2L_2}$
 $\Delta\lambda = \frac{\lambda^2}{2(n_1L_1 - n_2L_2)}$

Mode-selection filter

UC SANTA BARBARA
engineering
The convergence of research and innovation.

Early tunable, single-frequency diode lasers

- Coupling mirrors between integrated active and passive sections

→ Etched grooves

- Tunable single frequency
- Laser-modulator
- Laser-detector

L.A. Coldren, B.I. Miller, K. Iga, and J.A. Rentschler, "Monolithic two-section GaInAsP/InP active-optical-resonator devices formed by RIE," *Appl. Phys. Letts.*, 38 (5) 315-7 (March, 1981).

First integrated InP (laser - X) devices

UC SANTA BARBARA
engineering
The convergence of research and innovation.

Early tunable, single-frequency diode lasers

- Coupling mirrors between integrated active and passive sections
 - Etched grooves
 - Tunable single frequency
 - Laser-modulator
 - Laser-detector

L.A. Coldren, B.I. Miller, K. Iga, and J.A. Rentschler, "Monolithic two-section GaInAsP/InP active-optical-resonator devices formed by RIE," *Appl. Phys. Letts.*, 38 (5) 315-7 (March, 1981).

First integrated InP (laser – X) devices

- DBR gratings and vertical couplers
 - Tunable single frequency
 - Combined integration technologies

Y. Tohmori, Y. Suematsu, Y. Tushima, and S. Arai, "Wavelength tuning of GaInAsP/InP integrated laser with butt-jointed built-in DBR," *Electron. Lett.*, 19 (17) 656-7 (1983).

Single-Frequency and Tunable Lasers; Circa 1983

TOP VG. NO.

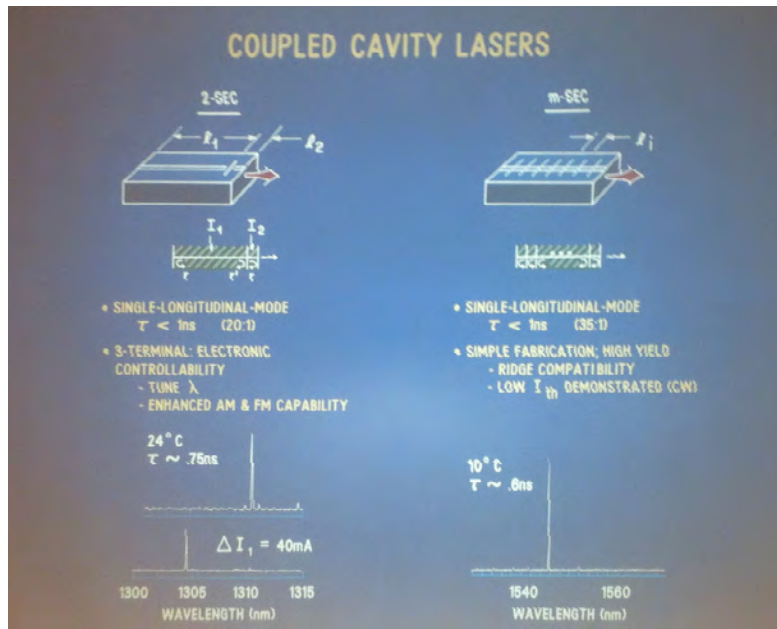
DO NOT AFFIX OVERLAYS ALONG THIS SURFACE

This set of eight slides of single frequency lasers. The slide in the top row and the slide in the second row are coupled cavity lasers. The slide in the third row is a phase-controlled laser. The slide in the fourth row is a phase-controlled laser. The slide in the fifth row is a phase-controlled laser. The slide in the sixth row is a phase-controlled laser.

IEEE Spectrum 1983

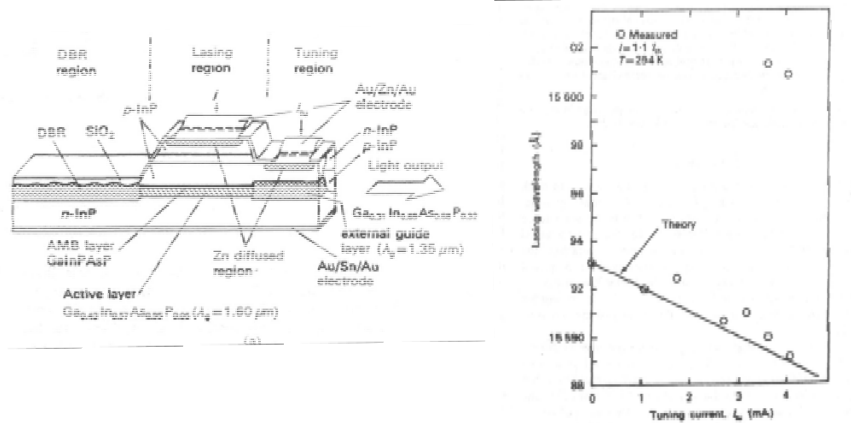
T. Bell, "Single-frequency semiconductor lasers," *IEEE Spectrum*, vol 20, 1983

Bell Laboratories



Coldren, Miller, Iga, and Rentschler, *APL*, **38** (Mar, '81); Ebeling, Coldren, Miller, Rentschler, *Electron., Lett.*, **18** ('82)

Pioneering Active-Passive interfaces



Tohmori, Suematsu, Tushima, and Arai, *TIT*, 1983

UC SANTA BARBARA engineering
The convergence of research and innovation.

No-Regrowth Groove Etch: RIE/HCl/Q-etch/HCl

RIE + WCE

011

Q

1 μm

1 μm

1. RIE
2. HCl
3. GaInAsP ETCHANT
4. HCl

Ti
Si₃N₄
GaInAsP
p-InP
GaInAsP
n-InP

Coldren, Furuya, Miller and Rentschler, *JQE*, 18 ('82)

Two-Section Coupled-Cavity Etched-Groove Tunable Laser

NOTES: DO NOT AFFIX OVERLAYS ALONG THIS SURFACE

ISLC '84, with T. Koch

RIE etch, Regrow InP, HCl etch

Bell Laboratories

UC SANTA BARBARA engineering
The convergence of research and innovation.

Tunable DBR Lasers (mid-late 1980's)

- Tune cavity modes and selection filter separately (or together)

- The center wavelength of grating, λ_g , will tune in direct proportion to the index change Δn_{DBR} ; however this will also tune the mode slightly as well, due to the penetration, L_{eff}
- Tuning the Phase section electrode will tune only the mode location, λ_m , (tune together with DBR for wide continuous tuning: *JQE* 23 (6) 903, June, 1987)
- There also may be some slight active region index change (due to loss changes)

$$\frac{\Delta \lambda_g}{\lambda_g} = \frac{\Delta \bar{n}_{DBR}}{\bar{n}_{DBR}}$$

$$\frac{\Delta \lambda_m}{\lambda_m} = \frac{\Delta \bar{n}_a L_a + \Delta \bar{n}_p L_p + \Delta \bar{n}_{DBR} L_{eff}}{\bar{n}_{ga} L_a + \bar{n}_{gp} L_p + \bar{n}_g DBR L_{eff}}$$

UC SANTA BARBARA engineering
The convergence of research and innovation.

Multi-element Mirror 4-Section Tunable Laser

- Combine vernier with DBR

United States Patent [19] [11] Patent Number: 4,896,325
Coldren [45] Date of Patent: Jan. 23, 1990

[54] MULTI-SECTION TUNABLE LASER WITH DIFFERING MULTI-ELEMENT MIRRORS
[75] Inventor: Larry A. Coldren, Santa Barbara, Calif.
[73] Assignee: The Regents of the University of California, Berkeley, Calif.
[21] Appl. No.: 235,307
[22] Filed: Aug. 23, 1988
[51] Int. Cl.⁴: H01S 3/10
[52] U.S. Cl.: 372/28; 372/99; 372/102; 372/38; 372/31; 372/29
[58] Field of Search: 372/101, 20, 92, 99, 372/102, 29, 32, 38

References Cited
U.S. PATENT DOCUMENTS
4,358,851 11/1982 Scifres et al. 372/6
4,504,950 3/1985 Au Yeung 373/101

OTHER PUBLICATIONS
Akiba et al.; "Self-Focusing Lens as Resonator enables 10 GHz Modulation"; *Fiberoptic Technology* Oct. 1981, p. 124.
Primary Examiner—Leon Soott, Jr.
Attorney, Agent, or Firm—Donald A. Streck

[57] **ABSTRACT**
An improvement for allowing selective tuning of the emitted beam over a broad bandwidth to a diode laser

having an active section for creating a light beam by spontaneous emission over a bandwidth around some center frequency and for guiding and reflecting the light beam between a pair of mirrors bounding the active on respective ends thereof to create an emitted beam of laser light. The mirrors each have narrow, spaced reflective maxima with the spacing of the reflective maxima of respective ones of the mirrors being different whereby only one of the reflective maxima of each of the mirrors can be in correspondence and thereby provide a low loss window at any time. The preferred mirrors each include a plurality of discontinuities to cause the narrow, spaced reflective maxima wherein the spacing of the discontinuities of one mirror is different from the spacing of the discontinuities of the other mirror so as to cause the wavelength spacing of the maxima to be different. Additionally, the preferred embodiment includes a vernier circuit operably connected to the mirrors which will cause continuous tuning within a desired frequency band, an offset control circuit operably connected to the mirrors for providing a voltage signal to the mirrors which will shift the reflective maxima of the mirrors into alignment at a desired frequency mode, and a phase control circuit for adjusting the laser mode wavelength to be in correspondence with the low loss window.

27 Claims, 3 Drawing Sheets

UC SANTA BARBARA engineering

Multi-element Mirror 4-Section Tunable Laser

The convergence of research and innovation.

United States Patent [19] (11) Patent Number: 4,896,325
Coldren [45] Date of Patent: Jan. 23, 1990

[54] **MULTI-ELEMENT TUNABLE LASER WITH DIFFERING MULTI-ELEMENT MIRRORS**
 [75] Inventor: Larry A. Coldren, Santa Barbara, Calif.
 [73] Assignee: The Regents of the University of California, Berkeley, Calif.
 [21] Appl. No.: 335,207
 [22] Filed: Aug. 23, 1988
 [51] Int. Cl.: H01S 3/10
 [52] U.S. Cl.: 372/29, 372/99, 372/102, 372/38, 372/51, 372/29
 [58] Field of Search: 372/101, 30, 92, 99, 372/102, 29, 32, 33

References Cited
U.S. PATENT DOCUMENTS
 4,304,841 11/1982 Skiffers et al. 372/6
 4,504,950 11/1981 Au-Yang 372/101

OTHER PUBLICATIONS
 Akiba et al., "Self-Focusing Lens as Resonator enables 10 GHz Modulation", Fiberoptic Technology Oct. 1981, p. 124.
 Primary Examiner—Leon Scott, Jr.
 Attorney, Agent, or Firm—Donald A. Streck

ABSTRACT
 An improvement for allowing selective tuning of the emitted beam over a broad bandwidth to a diode laser

27 Claims, 3 Drawing Sheets

DESCRIPTION OF THE PREFERRED EMBODIMENT

The novel four section tunable laser of the present invention is shown in simplified form in FIG. 5 where it is generally indicated as 38. By combining discrete mode-jump tuning with continuous tuning, it will be seen that this design allows the relative tuning range to be extended by at least an order of magnitude larger than $\Delta n/n$. To achieve the objectives, two multi-element mirrors 40, 42 are employed, one at each end of the laser 38. The gain section 36 and phase shifter section 32 are as described above with respect to the three-section laser of FIG. 3, of which this is an improvement.

UC SANTA BARBARA engineering

Sampled-Grating DBR Tunable Lasers

The convergence of research and innovation.

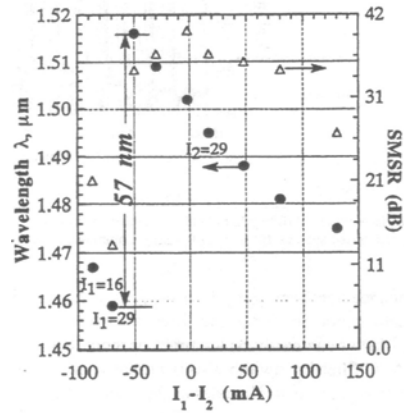
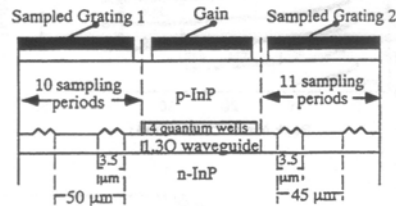
- 5-10X Tuning Range of DBR
- Reliable, Manufacturable InP Technology
- Can Cover C band, L band or C + L
- Easily Integrates Monolithically with Other Components (e.g. EAM, SOA)

3/6/2017 12:51 PM

Sampled-Grating DBR Tunable Laser

The convergence of research and innovation.

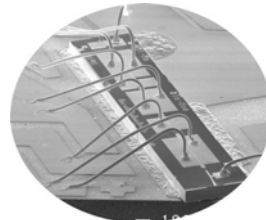
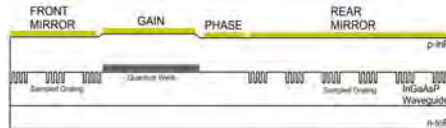
- Initial results
- 3 sections—vernier tuning



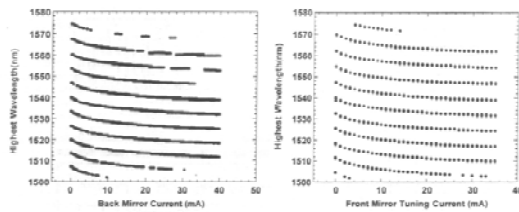
V. Jayaraman, A. Mathur, L.A. Coldren and P.D. Dapkus, ISLC 1992

SGDBR wide-tuning, high-power, high-reliability

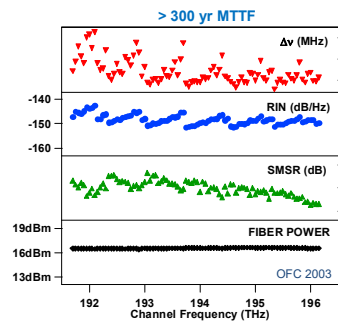
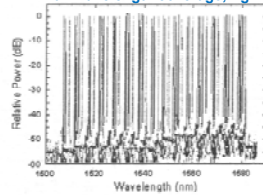
The convergence of research and innovation.



Agility Communications formed to Commercialize in 1998.



72 nm full wavelength coverage, Agility, 2001.



UC SANTA BARBARA engineering
The convergence of research and innovation.

Sampled-Grating DBR: Monolithic and Integrable

SGDBR+X widely-tunable transmitter:

- Foundation of PIC work at UCSB

UCSB'90-- → Agility'99-'05 → JDSU'05→

SG-DBR Laser

6 section InP chip

- Vernier tuning over 40+nm near 1550nm
- SOA external to cavity provides power control
- Currently used in many new DWDM systems (variations)
- Highly reliable— < 10% of SGDBR is grating
- Integration technology for much more complex PICs

Agility

JDSU-ILMZ TOSA (~ 18mm)

J. S. Barton, et al, *ISLC*, TuB3, Garmish, (Sept, 2002)

UC SANTA BARBARA engineering
The convergence of research and innovation.

Super-structure grating DBR laser

U.S. Patent June 28, 1994 Sheet 3 of 18 5,325,392

FIG. 3A

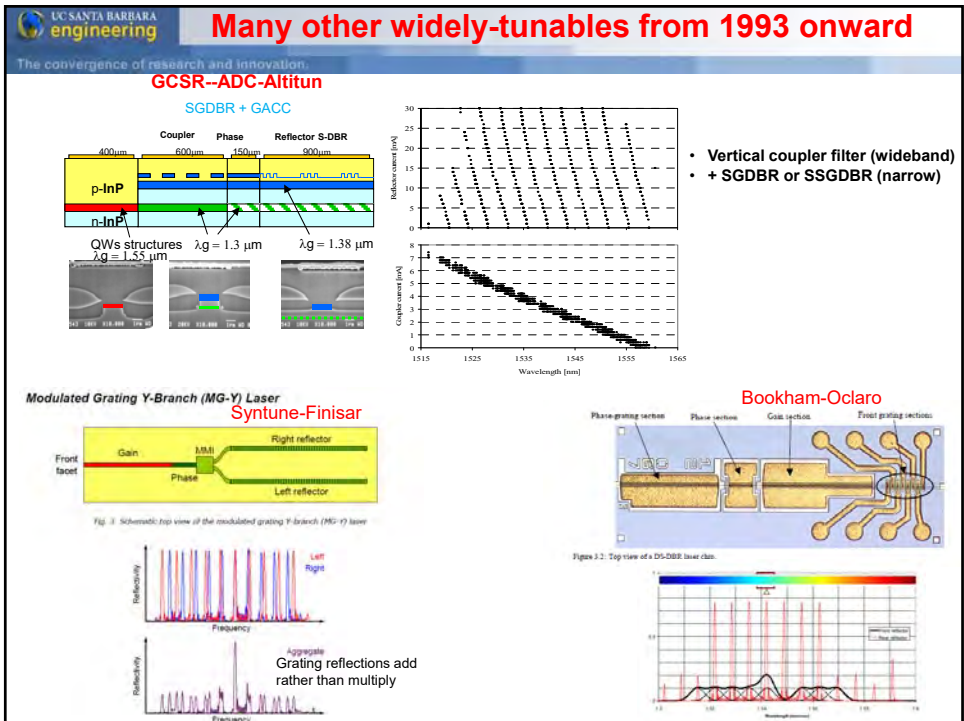
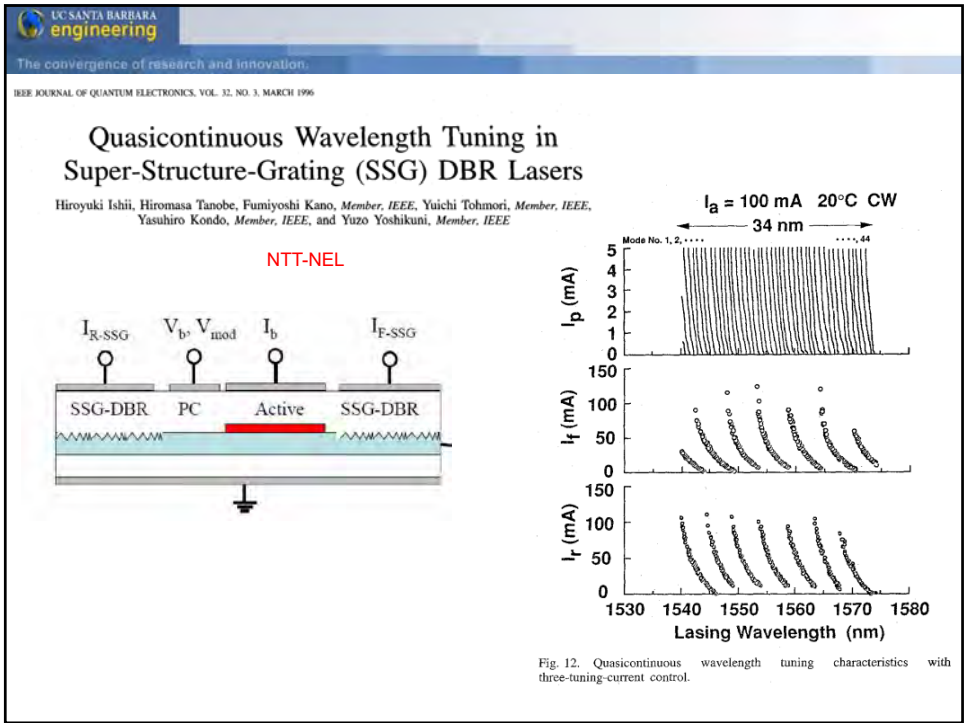
Distributed reflector and wavelength-tunable semiconductor laser

Tohmori, Yoshikuni, Ishii, Kano, Tamamura

--filed 3/3/1993

FIG. 3B

FIG. 3C



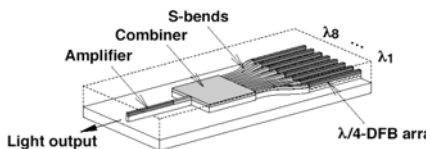
UC SANTA BARBARA engineering
The convergence of research and innovation.

Wavelength selectable "widely-tunables"

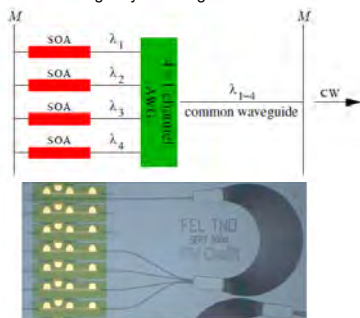
Fujitsu Laboratories Ltd.

Monolithic Integration of

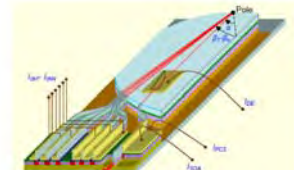
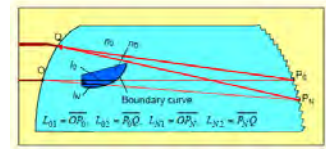
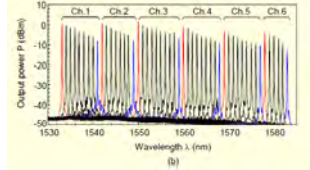
- Multi-wavelength DFB laser array
- Passive optical combiner
- Semiconductor optical amplifier



Select wavelength by selecting which SOA to turn on



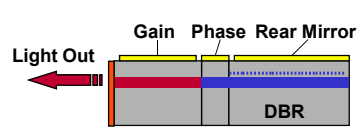
Eschelle Grating Laser

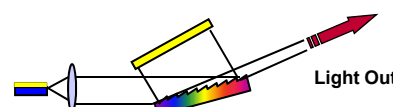




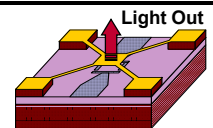
UC SANTA BARBARA engineering
The convergence of research and innovation.

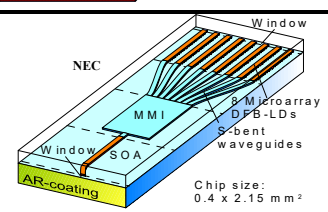
Solutions for Tunable Lasers (summary ~2005)

- **DBR Lasers**

 - Conventional DBR (<8 nm) [mid '80s]
 - Extended Tuning DBR's (≥ 32 nm) [early '90s]
- **External Cavity Lasers (≥ 32 nm)**

 - Littman-Metcalf/MEMs [late '90s]
 - Thermally tuned etalon
- **MEMS Tunable VCSEL (~ 32 nm)**

 - Optically or electrically pumped [late '90s]
- **DFB Array (~4nm X #DFBs)**

 - On-chip combiner + SOA [mid '90s]
 - Or, off-chip MEMs combiner
 - Thermally tuned

UC SANTA BARBARA engineering
The convergence of research and innovation.

Widely deployed commercial "WDM" PICs

EML's:

into XFP transceivers, etc.

Tunables & Selectable Arrays:

Logikhem
oclaro

UCSB → AGILITY → JDSU

FURUKAWA ELECTRIC
courtesy of T. Koch 2012

Narrow linewidth thermally-tuned SGDBR Laser

Mike Larson (TuC2)

- 70kHz linewidth and 50dB SMSR at +17dBm fiber power over 41nm range in C-band

Output Power and SOA Current

Instantaneous Linewidth

Side Mode Suppression Ratio

LUMENTUM M.C. Larson et al., OFC 2015, M2D.1 26

Tunable Interferometric Transmitter (Tunit) FREEDOM PHOTONICS

- Dual output Vernier tunable laser
 - 50 dB SMSR, well behaved tuning, 50nm
- Interferometrically combined modulator outputs
 - 12.5 Gbps operation, chirp control
 - 80+ km reach, SMF-28
- US Patent 9344196 (05/2016)

HR Coating Gain Phase Control Vernier Mirrors Out #1 SOA Out #2

Hig. ators

Freedom Photonics – Tunit – Tunable Interferometric Transmitter 27

InP Widely-tunable Coherent Receiver PIC

(Homodyne or Intradyne—also for Optical Synthesis)

SG-DBR laser

- 30 mW output power
- 40 nm tuning range
- 25 mA threshold current

90 deg hybrid

- 1x2 MMI couplers
- Directional couplers
- Phase shifters

↓

No phase error
4% power imbalance

UTC photodetectors

- 29 GHz 3-dB bandwidth with -2V bias
- 18 mA saturation current at -5V bias.

Mingzhi Lu, et al., Optics Express, Vol. 20, Issue 9, pp. 9736-9741 (2012)

UC SANTA BARBARA engineering
The convergence of research and innovation.

Phase Locked Coherent BPSK Receiver

Homodyne OPLL + Costas Loop → 1 cm² footprint

Fabricated by Mingzhi

Loop filter and system designed by Hyunchul

Designed by Eli using Teledyne 500nm HBT Process

Photonic IC: SGDBR laser, optical hybrid, and un-balanced PDs

Electrical IC: limiting amplifiers and phase & frequency detector (PFD)

Hybrid loop filter: Feed-forward technique, op-amplifier and 0603 SMDs

Mingzhi Lu, et. al., Optics Express, 20, (9), pp. 9736-9741 (2012)

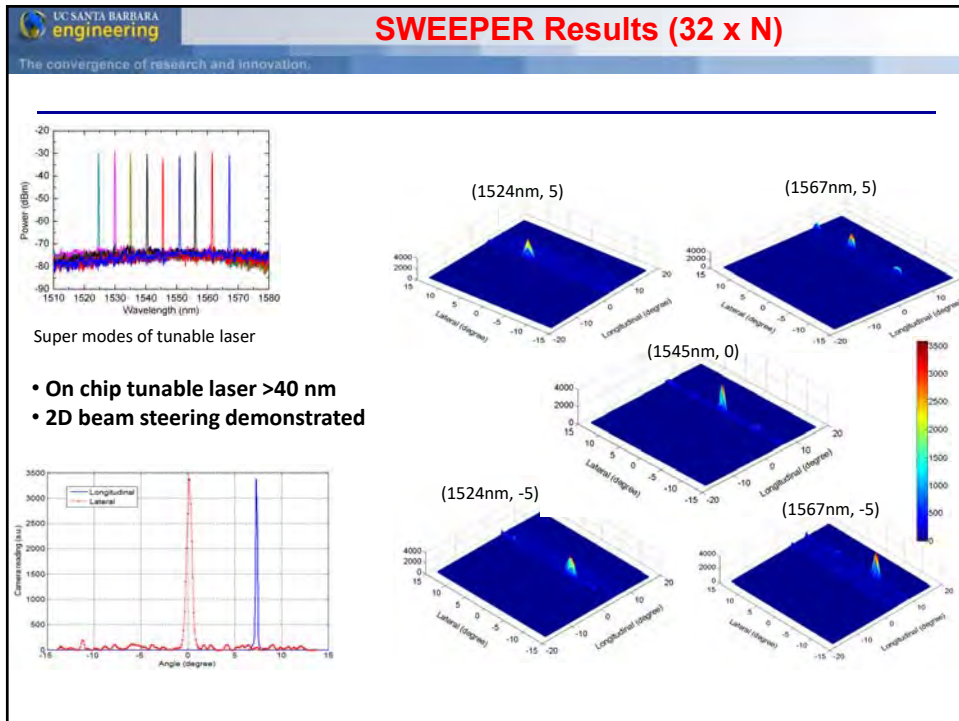
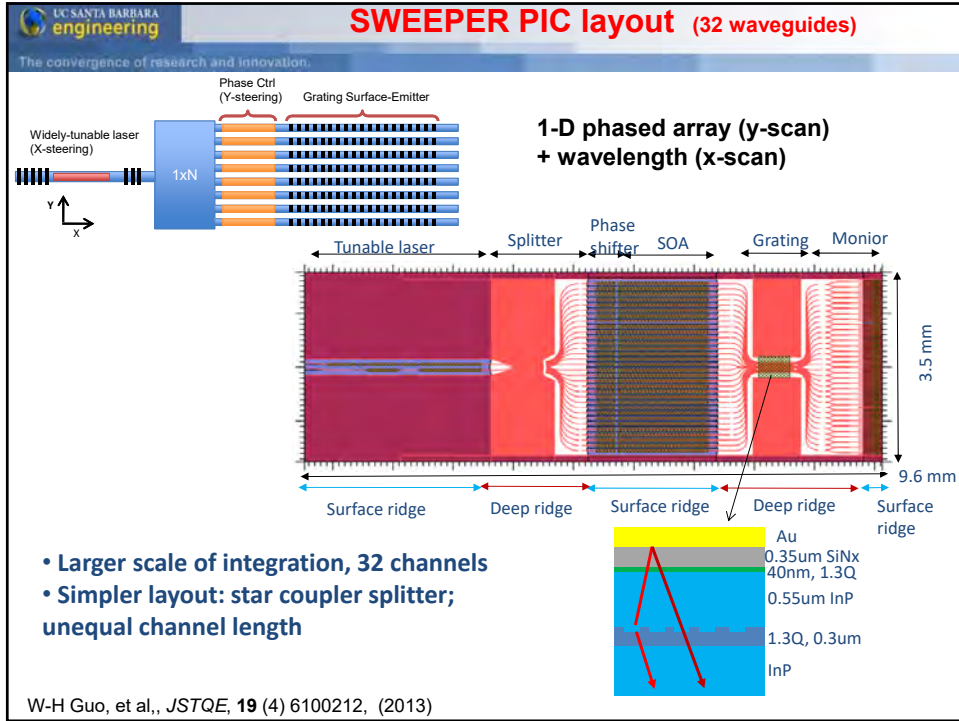
UC SANTA BARBARA engineering
The convergence of research and innovation.

“Analog” Coherent OPLL BPSK Receiver

- BER vs. OSNR (20Gb/s to 40Gb/s) → **No ADC—No DSP**
- Error-free up to 35Gb/s, < 1.0E-7 @ 40Gb/s
- PRBS 2³¹-1 signals – up to 40Gb/s
- Open eye diagrams for 25Gb/s and 40Gb/s

OSNR (dB/0.1nm)	40Gb/s BER	35Gb/s BER	30Gb/s BER	25Gb/s BER	20Gb/s BER
12	1.0E-3	1.0E-3	1.0E-3	1.0E-3	1.0E-3
14	1.0E-3	1.0E-4	1.0E-4	1.0E-4	1.0E-4
16	1.0E-3	1.0E-5	1.0E-5	1.0E-5	1.0E-5
18	1.0E-4	1.0E-6	1.0E-6	1.0E-6	1.0E-6
20	1.0E-4	1.0E-7	1.0E-7	1.0E-7	1.0E-7
22	1.0E-4	1.0E-8	1.0E-8	1.0E-8	1.0E-8
24	1.0E-4	1.0E-9	1.0E-9	1.0E-9	1.0E-9
26	1.0E-4	1.0E-10	1.0E-10	1.0E-10	1.0E-10
28	1.0E-4	1.0E-11	1.0E-11	1.0E-11	1.0E-11
30	1.0E-4	1.0E-12	1.0E-12	1.0E-12	1.0E-12
32	1.0E-4	1.0E-13	1.0E-13	1.0E-13	1.0E-13
34	1.0E-4	1.0E-13	1.0E-13	1.0E-13	1.0E-13
36	1.0E-4	1.0E-13	1.0E-13	1.0E-13	1.0E-13

ECOC '12 with Rodwell and Johansson



Indium Phosphide

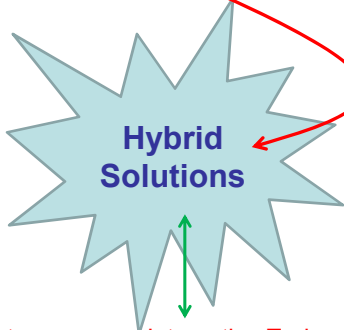
- Excellent active components
- Mature technology
- Complexity/propagation losses for passive elements
- Foundries evolving

Silica on Silicon (PLC)

- Excellent passive components
- Mature technology
- Lack of active elements

Polymer Technology

- Low loss
- Passive waveguides
- Modulators
- No laser



Silicon Photonics

- Piggy-back on Si-CMOS technology
- Integration with electronics?
- Constantly improving performance
- No laser

"Heterogeneous Integration Technology"

The convergence of research

Narrow linewidth tunable laser using coupled resonator mirrors

Tin Komljenovic, Michael Davenport, Sudharsanan Srinivasan, Jared Hulme, and John E. Bowers
*Electrical & Computer Engineering, University of California Santa Barbara, CA 93106.
 tkomljenovic@ece.ucsb.edu*

Hybrid-Si Platform
 --Vernier tuning with ring-mirrors

T. Komljenovic, et al, *IEEE JSTQE*, Vol: 21 Nov 2015

UC SANTA BARBARA
engineering
The convergence of research and innovation.

Summary

- Early vernier-tuned coupled-cavity laser concepts together with those of DBRs led to the creation of a four-section widely-tunable vernier-tuned design that is still in wide use today
- Many other widely-tunable laser designs have been developed over the years driven mainly by the need for a universal WDM source
- Integration technology developed for such lasers enabled many more complex Photonic Integrated Circuits
- Close integration of control/feedback electronics will be desirable in many future PIC applications
- Heterogeneous integration enables compatibility with different technologies—e.g., Si-photonics

UC SANTA BARBARA
engineering
The convergence of research and innovation.

Flip-chip tunable laser

The diagram illustrates the structure of a flip-chip tunable laser. It consists of several layers: a top InP layer with a reflector, gain, taper, and GC (Grating Coupler) section; a Buried Oxide layer; and a Si handle. A phase tuning section and a Si reflector are also shown. A red arrow indicates the direction of light propagation.

- Also being explored with evanescent coupling

Ashok Krishnamoorthy, O/C (2014)

I. Photonic Integrated Circuits

B. SOAs and Phase-Sensitive Amplifiers

First Monolithically Integrated Dual-Pumped Phase-Sensitive Amplifier Chip Based on a Saturated Semiconductor Optical Amplifier

Wangzhe Li, *Member, IEEE*, Mingzhi Lu, Antonio Mecozzi, *Fellow, IEEE*,
Michael Vasilyev, *Senior Member, IEEE*, Shamsul Arafin, *Member, IEEE*,
Danilo Dadic, Leif A. Johansson, *Member, IEEE*, and Larry A. Coldren, *Fellow, IEEE*

(Invited Paper)

Abstract—For the first time, a monolithically integrated photonic phase-sensitive amplification chip is fabricated and demonstrated based on an InP/InGaAsP platform. Different semiconductor optical amplifiers have been fabricated as well for characterization. On the chip, two tunable laser pumps that are coherently injection-locked, respectively, from two first-order sidebands of an externally modulated tone are generated to enable signal-degenerate dual-pumped phase-sensitive amplification in a saturated semiconductor optical amplifier. Experiments on different chips are conducted to successfully demonstrate phase-sensitive amplification with approximately 6.3 and 7.8 dB extinction of phase-sensitive on-chip gain. Theoretical simulations are performed and agree well with experimental results. The additive noise properties of the phase-sensitive amplification chip are also investigated.

Index Terms—Phase sensitive amplifier, semiconductor optical amplifier, photonic integrated circuit, four-wave mixing.

I. INTRODUCTION

OPTICAL phase-sensitive amplifiers (PSAs) have been attracting increasing attention [1], [2] due to unique advantages that enable them to break the 3-dB quantum limit of the noise figure (NF) [3], as well as achieve the phase regeneration to reduce phase and time jitters in optical transmission links [4]–[6]. Unlike a conventional phase-insensitive amplifier (PIA) such as an erbium-doped fiber amplifier (EDFA), featuring an inherent minimum NF of 3-dB [7], a PSA is capable of amplifying only one of the two quadrature phase

components in a light wave signal and attenuating the other. This unique feature makes it possible in theory to realize noise free amplification, leading to a NF of 0 dB, which can find numerous applications where noise levels are critical, such as optical telecommunication, remote sensing, optical spectroscopy, LIDAR and inter-satellite communication. Various PSAs have been demonstrated by using parametric down-conversion in $\chi^{(2)}$ -based nonlinear materials [8], [9], such as periodically poled LiNbO₃ (PPLN) waveguides and nonlinear optical loop mirrors (NOLMs) [10], or using four-wave mixing (FWM) in $\chi^{(3)}$ -based nonlinear media like optical fibers [2] and unsaturated semiconductor optical amplifiers (SOAs) [11]. New CMOS-compatible platforms are also emerging [12].

Among all demonstrated PSAs so far, their implementations are based on free-space bulk-crystal system or bench-top fiber systems, which makes it difficult to use them in practical scenarios. One of the challenges in realizing a practical PSA is that at input port of the PSA the phase relationship between the pump(s) and the signal must be synchronized and stabilized. Some solutions to synchronization of the pump and signal phases have been developed via pump injection locking [13] and optical phase-locked loop [14], which usually increase the complexity of the system and make it more unsuitable for use in a real application. In addition, other issues in terms of size, weight, power consumption and coupling losses also restrict the bench-top PSA's commercial allure. In order to solve this issue, photonic integration is a promising solution and can great benefit the implementation of PSAs for practical applications. Other than some obvious advantages like small footprint, light weight, reduced coupling losses and batch fabrication economies, integrated photonic chips can inherently guarantee a stable phase relationship among signal and pumps, requiring no phase-locking mechanisms, which significantly eases the implementation and practical application of PSAs.

In this paper, based on the implementation of a PSA through a dual-pump degenerate FWM process, a chip-scale PSA using a saturated SOA as a nonlinear element and different SOAs for characterization have been fabricated and for the first time an integrated photonic PSA chip has been experimentally demonstrated. The chip and SOAs fabrication is based on an InP/InGaAsP centered quantum well (CQW) platform. On the

Manuscript received October 15, 2015; revised December 12, 2015; accepted December 16, 2015. Date of publication December 24, 2015; date of current version January 15, 2016. This work was supported by Defense Advanced Research Projects Agency, Defense Sciences Office.

W. Li, S. Arafin, D. Dadic, L. A. Johansson, and L. A. Coldren are with the Department of Electrical and Computer Engineering, University of California at Santa Barbara, Santa Barbara, CA 93110 USA (e-mail: coldren@ece.ucsb.edu).

M. Lu was with the University of California at Santa Barbara, Santa Barbara, CA 93110 USA. He is now with Infinera Corporation, Sunnyvale, CA 94089 USA (e-mail: lumz85@gmail.com).

A. Mecozzi is with the Department of Physical and Chemical Sciences, University of L'Aquila, L'Aquila 67100, Italy (e-mail: antonio.mecozzi@univaq.it).

M. Vasilyev is with the Department of Electrical Engineering, University of Texas at Arlington, Arlington, TX 76019-0016 USA (e-mail: vasilyev@uta.edu).

Color versions of one or more of the figures in this paper are available online at <http://ieeexplore.ieee.org>.

Digital Object Identifier 10.1109/JQE.2015.2512538

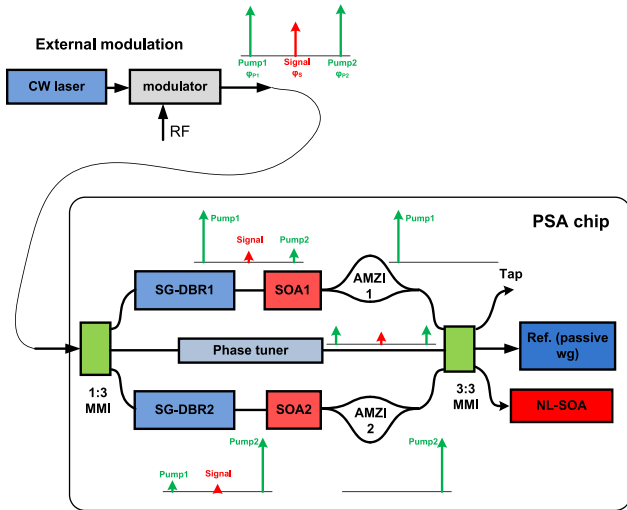


Fig. 1. Proposed schematic of demonstrating a chip scale dual-pump PSA.

chip, two tunable laser pumps that are coherently injection-locked from sidebands of an external modulated light wave are obtained to realize signal-degenerate dual-pumped PSA in a highly saturated SOA. A 6.3 dB and a 7.8 dB extinction ratio of gain based on different PSA chips are realized, which both agree well with simulation results. The reduction in signal-to-noise ratio is also estimated based on the measured optical spectrum of the light waves before and after the PSA.

II. PROPOSED CHIP-SCALE DUAL-PUMP PSA

Figure 1 shows the schematic of the degenerate dual pump PSA. The coherent incident light waves, which consist of two pumps and one signal, are here generated based on external modulation and then are coupled into a PSA chip. On the chip, the input light waves are split into three paths via a 1 by 3 multimode interference (MMI) coupler. Along the upper and lower paths, there are two tunable Sampled-Grating Distributed-Bragg-Reflector (SG-DBR) lasers [15], each of which is injection locked by opposite modulation side-band pumps. Please note that during external modulation the signal which is carrier would be intentionally suppressed by properly biasing the modulator so that the pumps have enough power to injection lock the two SG-DBR lasers. After being injection-locked, each SG-DBR laser which selectively amplifies the corresponding pump and suppresses the other one as well as the signal behaves as a pump laser. The signal suppression in each pump laser due to injection locking is important because such a suppression is helpful for avoiding on-chip signal-interference-induced signal power change at the input port of the PSA, which otherwise could be misinterpreted as the result of PSA. After further being amplified by a downstream SOA, the pump is filtered by an asymmetric Mach-Zehnder interferometer (AMZI) to remove the residual signal and the noise falling in the signal's spectrum, which avoids signal interference among three paths and enables the signal to be shot-noise limited.

Along the middle path, there is a phase tuner to phase shift the signal based on carrier plasma effects; therefore,

the adjustable and stable phase relationship among the signal and two pumps can be achieved for observing the PSA-based signal power variation as a function of the signal's phase. Please note that, although there are two pumps along the middle path, their powers are much smaller than those along the other two paths so that the interference of the pump waves along three paths are negligible. The light waves along three paths are combined together and split again by a 3-by-3 MMI coupler to a nonlinear-SOA (NL-SOA), a long passive waveguide (WG) as a reference port, and a tap to monitor the input light waves to the NL-SOA. The PSA occurs in the NL-SOA, and the process includes two main steps. The first step is generating new signal photons. Two pumps and a signal with a stable phase relationship are sent to a nonlinear media, in which FWM among the light waves is able to generate new signal photons with a phase which is the sum of two pumps' phases minus the original signal phase. In the second step, interference of the generated signal with original signal modulates the amplitude of the combined electrical field of the signal. Therefore, the constructive interference amplifies the amplitude of the signal's electrical field; while the destructive interference attenuates the signal. In another word, the PSA only maximally amplifies the signal when the original signal phase is 0 or π relative to the sum of two pumps' phases (in-phase components), and maximally attenuates the signal when its phase is $\pi/2$ or $3\pi/2$ (quadrature components) to the sum of two pumps' phases. Thus, the PSA gain experiences one cycle when the phase of the incident signal goes over one π , which is different from the transmission curve of a conventional Mach-Zehnder interferometer (MZI). Such a π -periodicity of the PSA gain is important and can be used to verify the implementation of the PSA. Therefore, in our demonstration of the chip-scale PSA, the relationship between the input signal phase and the signal power after the PSA can be recorded to verify the achievement of the PSA.

One potential concern is that the SOA can be used as a PIA, and its PIA gain may interfere with the nonlinear parametric process and undermine the PSA. To overcome or minimize this issue, the incident power to the NL-SOA is high enough to saturate the NL-SOA, which is capable of suppressing the amplified spontaneous emission noise. Therefore, the saturated NL-SOA can restrict PIA and optimize the FWM [16], [17]. By recording the light wave spectrum and the signal power at the output of the NL-SOA using an optical spectrum analyzer (OSA) when changing the current applied to the phase tuner to tune the signal phase, we can evaluate the PSA performance and characterize its gain profile.

III. SOA AND PSA CHIP FABRICATION

In order to fabricate SOAs for initial characterization and monolithically integrate the single-chip dual-pumped PSA based on saturated SOA, we chose an InP/InGaAsP centered quantum well (CQW) platform with 10 quantum wells (QWs) [18] because such a platform is capable of maximizing the mode overlap with the QWs in an SOA, enhancing the nonlinearity and maximizing the FWM.

The fabrication started with a base epi, which includes quantum well layers, waveguide layers and N-cladding layer.

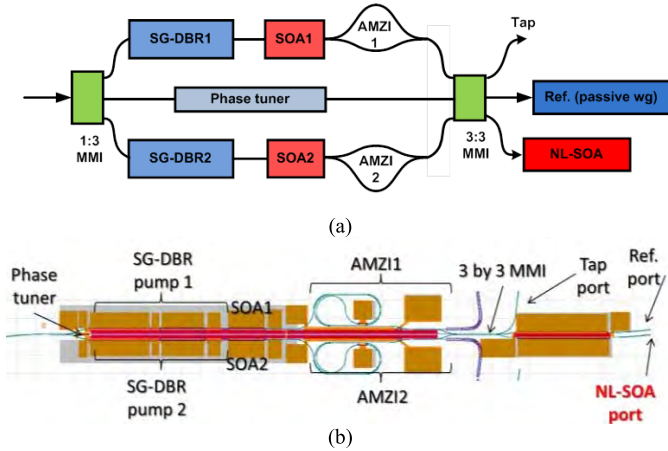


Fig. 2. (a) Schematic diagram of the PSA chip; (b) mask layout of the PSA-chip for fabrication.

Active and passive areas were defined using quantum well-intermixing (QWI) technology [19]. The passive waveguide with intermixed quantum wells still confine carriers well, which is ideal for low-loss phase tuners. Then, by using electron beam lithography and methane/hydrogen/argon (MHA)-based RIE etching, the gratings of the SG-DBR laser were defined. Following the grating definition, a blanket p-cladding and p-contact layer regrowth was carried out using metalorganic chemical vapor deposition (MOCVD). After the regrowth, waveguides were defined and etched. In order to have better heat dissipation and compactness at the same time, surface ridge waveguides were used for the straight SG-DBR lasers, while more-narrow deeply-etched waveguides were used for other components on the chip, which leads to better flexibility for waveguide routing and better SOA nonlinear efficiency due to a higher confinement factor. $\text{Cl}_2/\text{H}_2/\text{Ar}$ ICP-RIE dry etching as well as InP wet etching was used to define the features. Following the waveguide etching, P-contact vias were opened and Pt/Ti/Pt/Au was deposited as the P contact metal. To further decrease the passive waveguide loss and provide electrical isolation, we implanted protons in the p-cladding layer of the passive waveguides. The wafer was then thinned down to about $130\ \mu\text{m}$ for ease of cleaving. Backside Ti/Pt/Au metallization provided common cathode connections to the n-type substrate. After cleaving and anti-reflection coating of the waveguide facets, the discrete SOAs and the PSA chips were ready for characterization. The SOAs and the chip-scale PSA were fabricated on the same wafer so that the specifications of the SOAs would be identical to those of the SOAs in the PSA chip. The length and width of the PSA chip are about 1 mm and 7 mm. Fig. 2 shows the schematic diagram and the mask layout of the chip.

IV. SOA CHARACTERIZATION

Figure 3 shows all the different SOAs we fabricated. The longest SOAs are used to evaluate the dispersion. The high-speed SOAs which are the shortest are used to measure SOA's carrier lifetime; while the 1-mm SOAs are used to characterize their gain profile.

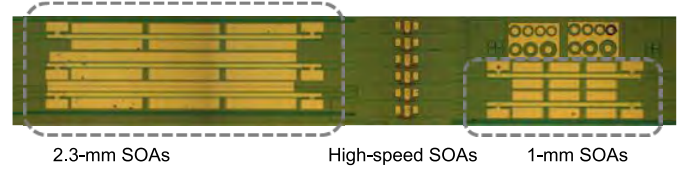


Fig. 3. Photo of the fabricated SOAs with different lengths. (left) 2.3-mm SOAs consisting of three cascaded SOAs with a length of $766\ \mu\text{m}$; (middle) high-speed SOAs with a length of 50, 100 and $150\ \mu\text{m}$; (right) 1-mm SOAs consisting of three identical SOAs with a length of $333\ \mu\text{m}$.

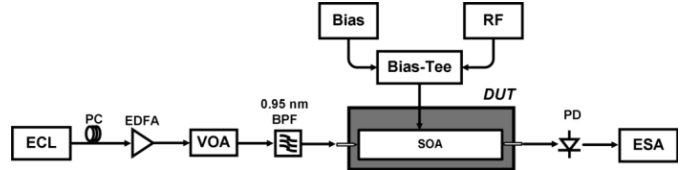


Fig. 4. SOA lifetime measurement setup.

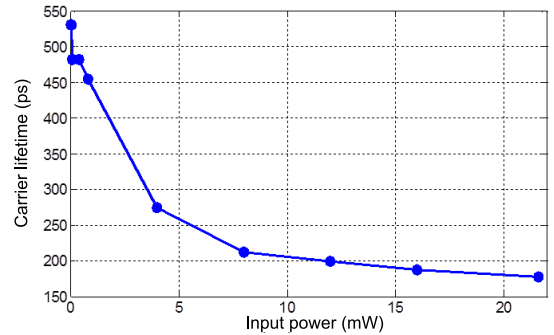


Fig. 5. Measured SOA carrier lifetime given different incident light wave power.

A. Carrier Lifetime Measurement

High-speed short SOAs were used to measure the carrier lifetime. The setup is shown in Fig. 4, which mainly includes an external cavity laser (ECL), an erbium-doped fiber amplifier (EDFA), a variable optical attenuator (VOA), a bandpass filter (BPF), a high-speed SOA, a photodetector (PD) and an electrical spectrum analyzer (ESA). A wavelength from the ECL was sent to the SOA through the EDFA, the VOA and the BPF which were used to control the input light wave power. To measure the SOA's carrier lifetime, we first measured its frequency response. To do so, an RF signal and a bias voltage were applied to the SOA via a bias-tee to modulate the light wave that was passing through the SOA. The SOA's output was converted by the PD to re-generate the RF frequency which was recorded and measured by the ESA.

The length of the SOA under test is $50\ \mu\text{m}$, biased with a current density of $6.67\ \text{kA}/\text{cm}^2$. We measured SOA's frequency response given different input power, and then based on its 3-dB bandwidth, the lifetime could be calculated. We plotted the relationship between the carrier lifetime and the input power to the SOA, as shown in Fig. 5. As it can be seen, the carrier lifetime goes down to $180\ \mu\text{m}$ as the input power increases to about 21 mW.

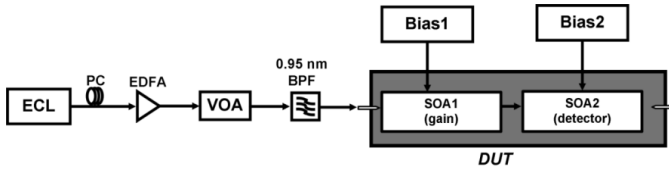


Fig. 6. SOA gain measurement setup.

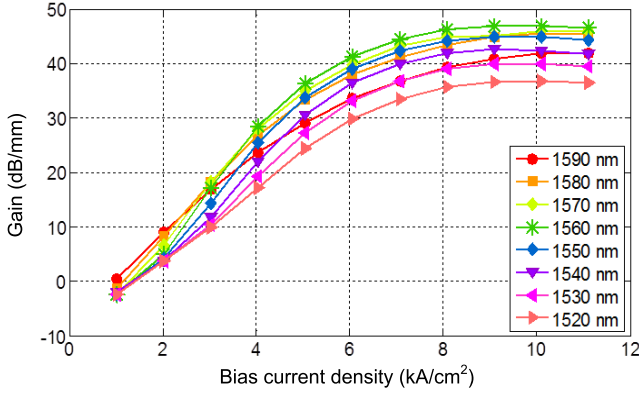


Fig. 7. Measured linear gain of a 1-mm SOA.

B. Small-Signal Gain Measurement

We took advantage of a 1-mm SOA consisting of three cascaded 333- μm SOAs to characterize its gain profile. The setup is shown in Fig. 6. Since the 1-mm SOA has three cascaded 333- μm SOAs, the first 333- μm SOA was negatively biased as a PD to measure the input power; then it was forward-biased as an amplifier to amplify the input light wave. The second 333- μm SOA was reverse-biased to detect the amplified light wave power at the output of the first 333- μm SOA.

Comparing the measured input power and the power after amplification, we can obtain the gain for a 333- μm SOA. Changing the forward bias current and the input wavelength, and tripling the calculated gain, we can collect gain profiles of the 1-mm SOA, which are shown in Fig. 7. Fig. 7 shows the relationships between small-signal gain of the SOA and current density given different input wavelengths. We can see that the small-signal gain goes up as we increase the current density and becomes saturated after the current density is higher than 8 kA/cm^2 . The transparent current density, given different wavelengths, is varied in the range between 1 kA/cm^2 and 1.5 kA/cm^2 . Fig. 8 shows the relationship between the maximum small-signal gain and the incident wavelength when the current density is fixed. As we can see from Fig. 8, the peak small-signal gain was measured to be about 47.5 dB/mm at a wavelength of 1560 nm and a current density of 9 kA/cm^2 . For the PSA experiment, we will choose a proper incident wavelength to optimize the gain of the SOAs for the operation of the PSA chip.

Because the PSA-chip is based on a saturated SOA, we need to find out the input power level to saturate the SOA. Since the length of the NL-SOA on the PSA chip is 1 mm, then we treated the 1-mm cascaded SOA as a single SOA, and we applied a current density of about 3 kA/cm^2 and measured

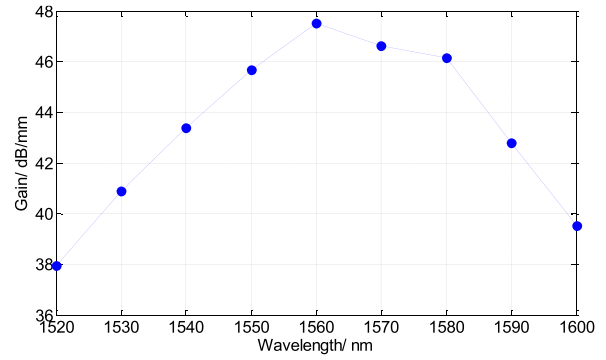


Fig. 8. Measured wavelength-dependent small-signal gain profile.

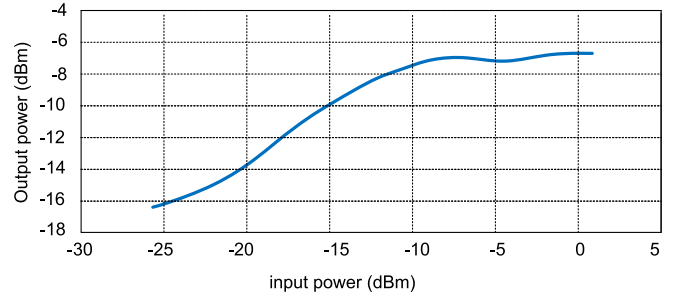


Fig. 9. Measured output power of the SOA with respect to the input power.

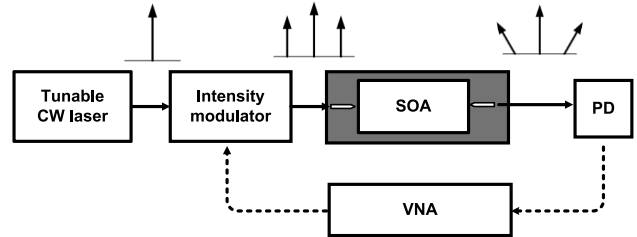


Fig. 10. SOA dispersion measurement setup.

its output power as we increased the input power. The result is plotted in Fig. 9, showing that the 1-mm SOA would be saturated when the input power reaches about -9 dBm. Based on this input power level, we chose an incident power of 0 dB or higher to the NL-SOA on the PSA chip to ensure that the NL-SOA was deeply saturated.

C. Dispersion Measurement

In the implementation of the PSA based on a long single mode fiber or a high nonlinearity fiber, the fiber dispersion can play an important role in the PSA effect, reducing the PSA gain or gain bandwidth. Similarly, for operating the PSA chip, we have to find out the dispersion characteristics of a saturated SOA. A method to measure the dispersion has been proposed.

The setup shown in Fig. 10 consists of a tunable laser source, an intensity modulator (IM), a PD and a vector network analyzer (VNA). The light wave from the laser was external modulated through the IM by an RF signal applied to the IM. The RF signal was generated from the VNA. Due to the small-signal modulation, the light wave would have two more

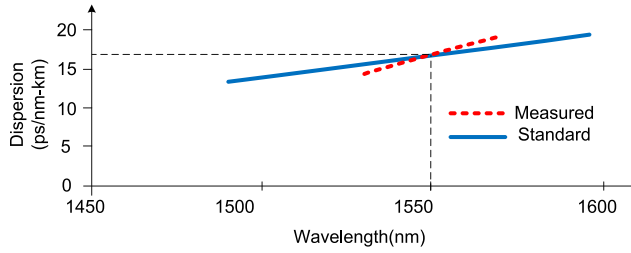


Fig. 11. Comparison of the measured dispersion of a 2-meter SMF and its standard dispersion value.

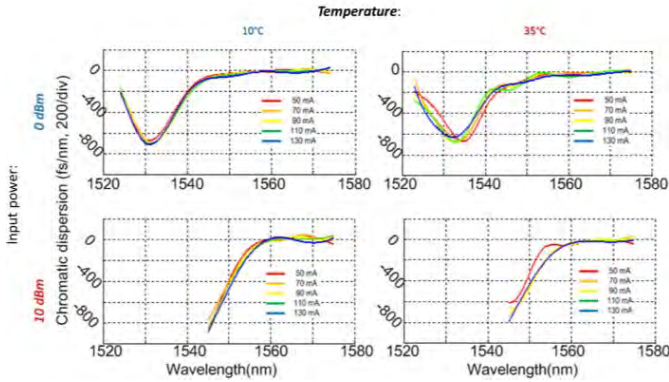


Fig. 12. Measured SOA dispersion curves given different temperatures and input powers.

sidebands; and after passing through the SOA, nonlinear phase changes were applied to the sidebands and the original carrier due to the dispersion of the SOA. The sidebands and the carrier were sent to the PD to re-generate the RF signal which was recorded by the VNA. Then the nonlinear phase changes introduced by the dispersion could be recovered by the comparing the RF phase changes. When we swept the input wavelength and recorded the corresponding nonlinear phase changes or the RF phase differences, we could calculate the dispersion of the SOA.

Before measuring the dispersion of the SOA, we need to evaluate this setup and prove it is functional. Therefore, we use the setup to measure the dispersion of a 2-meter signal mode fiber (SMF) and compared the result with the standard dispersion result of an ITU G.653 single mode fiber. The input wavelength was shifted from 1545 nm to 1575 nm. As we can see from Fig. 11, at 1550 nm, the measured result agrees well with the standard dispersion value; The dispersion slot is different, which could be caused by the facts that the standard SMF dispersion is based on a few km meter fiber (averaging thousands of different 2-meter SMFs) and the input wavelength was not stable and drifting during the experiment.

After proving that the setup in Fig. 10 is functional, we measured the dispersion of a 2.3-mm SOA given different temperature and input power. The input power was set to be 0 dBm and 10 dBm, which are high enough to saturate the SOA. Please note that before each measurement, we removed the SOA first and measured the background dispersion including the modulator and the 16-meter fiber in the setup.

The measured dispersion is shown in Fig. 12, as we can see, dispersion curves are not flat. When temperature was

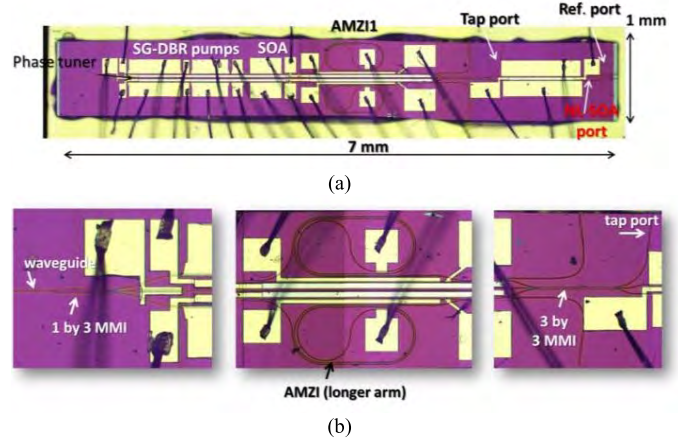


Fig. 13. (a) Photo of the signal-degenerate dual-pumped PSA chip after wire-bonding; (b) close-up views of some sections of the chip.

fixed at 0 degree Celsius, given a 0-dBm input power, the dispersion is flat and close to 0 fs/nm when the wavelength falls in a range between 1550 nm to 1570 nm. At a shorter wavelength range between 1525 nm to 1545 nm, there is a dispersion notch, and the saturated SOA shows a relatively large dispersion of -700 fs/nm, or -304 fs/nm/mm at a wavelength of 1530 nm. When the input power was increased to 10 dBm to further saturate the SOA, the measurement can only covers a wavelength range from 1545 nm to 1575 nm because of the limited gain bandwidth of the EDFA we used in the experiment; however, thanks to the appearance of the right edge of the notch, we can still tell that the dispersion curves are red-shifted. Then we increased the temperature to 35 degree Celsius, we repeated the measurement and found out that the dispersion characteristics stayed the same.

The measurement still has a few issues. The wavelength instability caused dispersion ripples on the curves; large background dispersion introduced by the 16-meter long fiber in the setup made it difficult to accurately measure the small amount of dispersion.

For the future PSA experiment and simulation, we chose the incident wavelength around 1560 nm and treated the SOA as dispersion-free element.

V. PSA CHIP CHARACTERIZATION

Fig. 13 shows a microscope picture of the fabricated PSA chip after being wire-bonded and a close-up view of some sections of the chip. We can clearly see the metal contacts which are the large golden squares, the thin waveguide at the input port of the 1 by 3 MMI, the long and curled waveguide as one arm of the AMZI, and the 3 by 3 MMI before the input of the NL-SOA and tap waveguide.

Before conducting the PSA experiment, we need to characterize the chip to choose the best chips. Specifically, we evaluated the performance of the SG-DBR lasers, the injection locking of the two SG-DBR lasers and the spurious signal interference among three paths.

A. SG-DBR Lasers

First of all, the two SG-DBR lasers were pumped and light-current-voltage (LIV) curves were measured. A typical

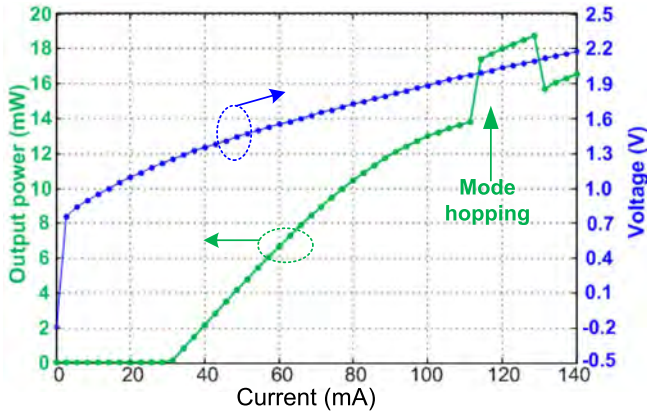


Fig. 14. Measured LIV curve of a SG-DBR laser.

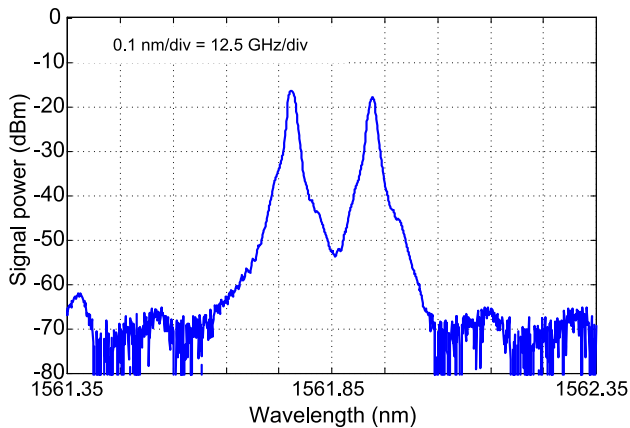


Fig. 15. Measured optical spectrum of the output of two free-running SG-DBR lasers.

measured LIV curve is shown in Fig. 14. The green curve is the measured laser output power as we increased the pump current. The kink on the curve represents a mode-hopping which was caused by the internal temperature and refractive index change as we changed the current. As we can see, the SG-DBR laser has a threshold of about 30 mA at a temperature of 20 degree Celsius, and a maximum output power of about 18 dBm at a bias current of 120 mA. However, when both SG-DBR lasers were turned on, the maximum output of each one was only about 12 dBm or less due to heating effect.

The outputs of two SG-DBR lasers were measured as well using an optical spectrum analyzer (OSA, with a resolution of 0.01 nm) and shown in Fig. 15. The two wavelengths are spacing around 0.15 nm, which is equivalently 18.7 GHz. We can easily tune the wavelengths by changing the current applied to the corresponding phase section in each SG-DBR laser. The averaged tuning rate is about 1.18 GHz/mA. However, due to heating effect, tuning one wavelength always changed the other one in the experiment.

B. Injection Locking of Two SG-DBR Lasers

Because injection locking two SG-DBR lasers is important to make sure that the two pumps and the signal sent to the NL-SOA to have the stable phase relationship, we have to evaluate the injection locking performance of each laser.

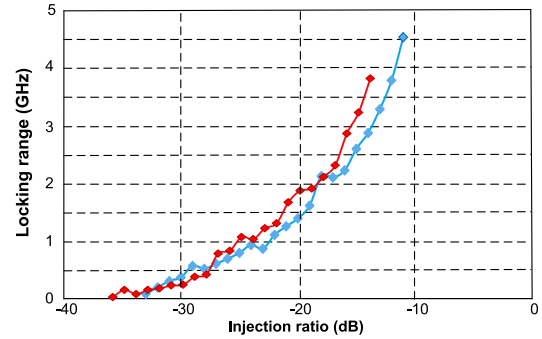


Fig. 16. Measured injection locking ranges of two SG-DBR lasers given different injection ratios.

We simply used an external laser to send the light wave to the chip and turned on only one SG-DBR laser. Then at the tap port, we used an OSA to monitor two wavelengths and started to align them with each other. Once they were close enough, we coupled the output of the tap to an external PD to convert the light waves to an electrical beat note which was analyzed by an ESA and we observed an unstable peak due to the random phase relationship between two wavelengths. When the spacing between two wavelengths became closer and closer, we observed that the central frequency of the beat decreased. Once the two wavelengths were close enough, the beat signal disappeared and only a flat noise floor appeared on the ESA which indicated that the SG-DBR laser was injection locked and its wavelength was as same as the external one. By shifting the wavelength of the sideband through changing the frequency of the modulation RF signal, and the incident sideband power, we measured the injection locking range with respect to different injection ratio. The injection ratio is the power ratio of the incident sideband power to the laser output. Then we turned off the laser, turned on the other and repeated the same measurement. The results are plotted in Fig. 16. As we can see that the maximum locking ranges are about 4.5 GHz and 3.8 GHz when the injection ratio is maximized in the experiment. However, for the PSA experiment, both SG-DBR lasers must be injection-locked, the total input power from external modulation was distributed on two sidebands (the signal power can be ignored), which reduced the injection ratio by 3 dB. Therefore, only 3 GHz and 2.2 GHz injection locking ranges can be achieved. Considering the laser wavelength shifting due to cross heating effect when we changed the phase tuner current, the real locking range for each laser would be smaller.

Once two SG-DBR lasers were both injection-locked by the two pumps from external modulation, the beat note of two wavelengths at a PD becomes a very stable and narrow line and can be monitored by the ESA, as shown in Fig. 17. The resolution bandwidth of the ESA was about 100 Hz. The 3-dB bandwidth of the beat is less than 1 kHz, which means that once two SG-DBR lasers are injection locked, their relative frequency spacing is fixed and determined by the two pumps and their relative linewidth is also less than 1 kHz. Thus, once we observe a stable peak with a frequency of twice the RF modulation frequency at the ESA, we can claim that

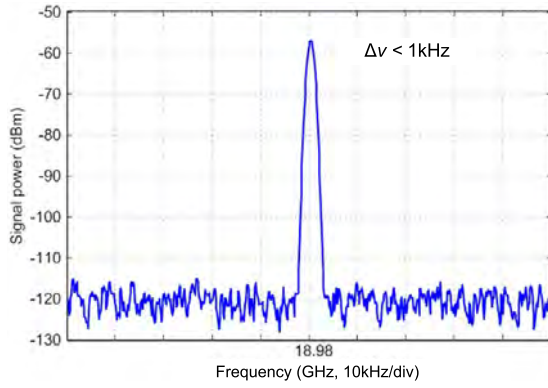


Fig. 17. Measured electrical spectrum of the beat by heterodyning the wavelengths from two injection-locked SG-DBR lasers.

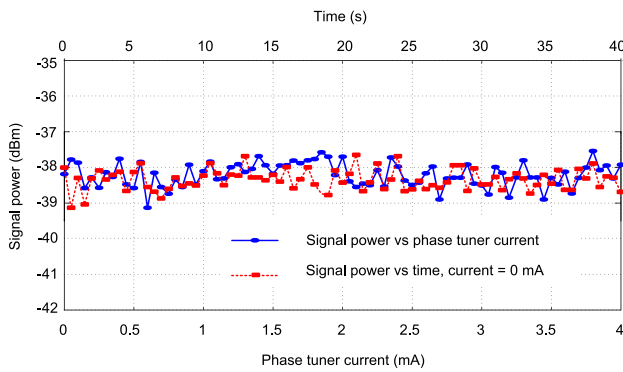


Fig. 18. Measured signal power at the output of the tap with and without phase tuner current changing.

the two SG-DBR lasers are injection-locked. During the PSA experiment we conducted, we always used the ESA to monitor the beat note of two SG-DBR lasers through the tap port to make ensure the injection locking was enabled.

C. Spurious Signal Interference

As we mentioned before, another advantage of injection locking is the suppression of the signal, which ensures that signal passes through the upper and middle paths, causing signal interference and leading to possible misinterpreted PSA effect. Therefore, after two SG-DBR lasers were injection-locked and before we started to evaluate the PSA by recording the signal power at the output of the NL-SOA, we have to first rule out the possibility of the signal interference among three paths to avoid improper interpretation of the PSA when shifting the signal phase by change the phase tuner current. Thus, at the output of the tap port, the signal power with respect to time and phase tuner current were measured and compared, as shown in Fig. 18. The blue solid curve is the measured signal power as we increased phase tuner current; while the dotted red curve is the measured signal power over time. By comparing two curves here, only similar random power fluctuations of about ± 0.5 dB were observed in two cases and no obvious interference among three paths was observed.

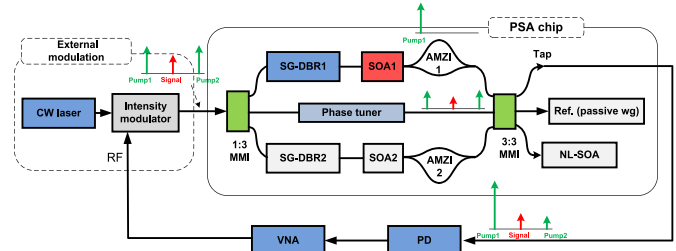


Fig. 19. Relative signal phase measurement setup.

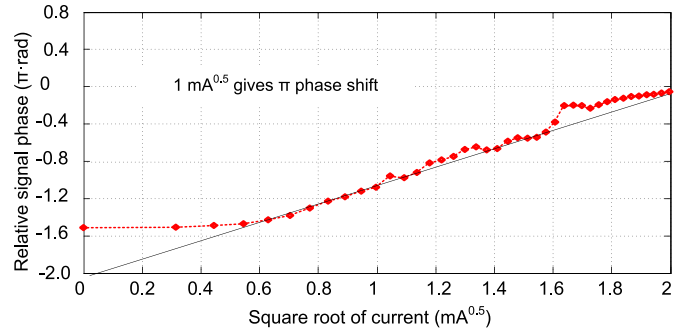


Fig. 20. Measured relative signal phase change.

In addition, the power of the SG-DBR pump waves along the upper and the lower paths were about 15 dB higher than those along the middle path, therefore, the pump interference which could cause PSA gain drift can be ignored as well, and the signal power change at the output of the NL-SOA would be only caused by the PSA.

D. Phase Tuner Characterization and Phase Shift Measurement

Tuning the phase of the signal is important for the PSA experiment. And knowing the exact phase shift when we tune the current applied to the phase tuner is more important because we need to take advantage of π -periodicity of the PSA gain curve to verify the PSA. To obtain relative phase change of the signal, we used the setup shown in Fig. 19.

The RF signal for the external modulation was from the VNA. One SG-DBR laser was turned off so that only one SG-DBR laser was injection locked and only one sideband was selectively amplified. Please note that the power of the amplified sideband was much larger than those of sidebands along the middle path so that the later were ignored. The signal and the amplified sideband at the output of the tap were sent to the PD to re-generate the RF signal whose phase change would be identical to that of the optical signal. Therefore, by using the VNA to measure the phase change of the received the RF signal when changing the phase tuner current, we were able to equivalently get the relative phase change of the optical signal. The result is shown in Fig. 20. The abscissa variable is set to be the square root of the phase tuner current because the signal phase in theory varies linearly with the square root of the phase tuner current. As we can see, there was no obvious phase change of the signal until after the current was larger than 1 mA. Such a delay in phase shift commonly occurs in

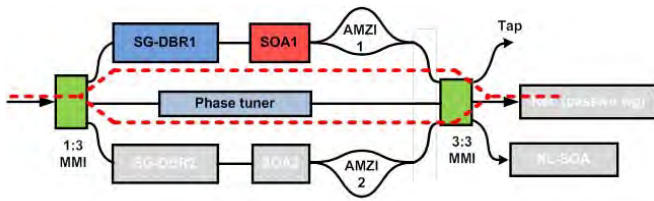


Fig. 21. On-chip MZI setup.

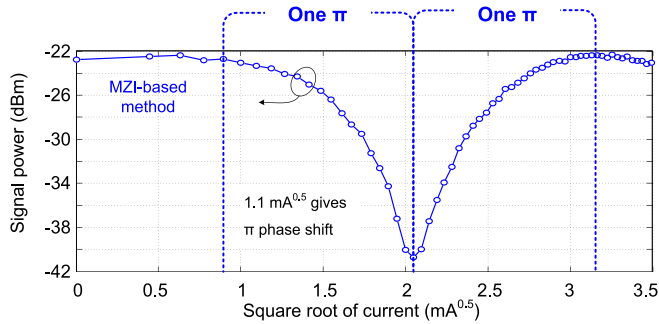


Fig. 22. Measured MZI output when changing the phase tuner current.

tunable SG-DBR lasers and could be caused by an N+ sheet charge that exists at the regrowth interface due to surface contamination. As the current was further increased, these traps are filled and phase shift appeared. Overall, $1 \text{ mA}^{0.5}$ gives π phase shift of the signal.

To help evaluate the signal phase measurement, we also formed an on-chip MZI by deactivating the lower path. Without external modulation, we sent one wavelength to the chip and injection locking one SG-DBR laser and measured the output power at the tap when we were changing the phase tuner current. The on-chip MZI is depicted in Fig. 21. It is well-known that the output power of the MZI varies sinusoidally with the phase difference of the light waves along two arms, and features a 2π -periodicity. Therefore, we can estimate the current-induced phase shift of the signal by observing the MZI output as we change the phase tuner current.

The measured MZI output is shown in Fig. 22. As we can see, the output power barely changes when the current is less than 1 mA due to the phase delay. As the current increase, the signal power experiences one cycle. It can be clearly seen that approximately $1.1 \text{ mA}^{0.5}$ gives one π phase shift, which agrees well with the result obtained based on previous method ($1 \text{ mA}^{0.5}$ gives π phase shift).

VI. PSA EXPERIMENTAL RESULTS AND DISCUSSION

Once the basic chip characterizations were completed and the best chips were chosen, we started to configure the chip and the external modulation setup to start the PSA experiment. For external modulation, two pumps spacing about 18 GHz and one signal were generated by using an external tunable laser and an IM as in Fig. 1. The IM was properly biased to suppress the signal power, which made the sidebands' power dominant and facilitated the injection locking. The incident light waves were coupled into the PSA chip via a tapered

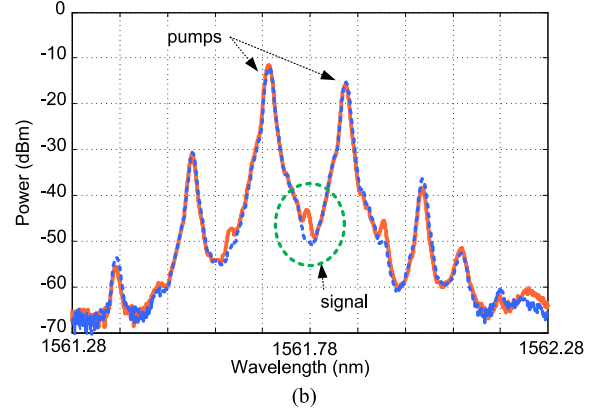
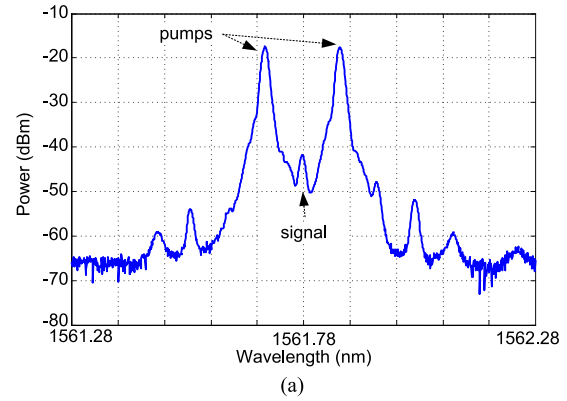


Fig. 23. Measured optical spectrum of the light wave at (a) the input and (b) the output of the NL-SOA.

fiber with a total coupling loss of about 6 dB . The pump power coupled into the SG-DBR laser was about -3 dBm and the output power of each laser is about 11 dBm , giving an injection ratio of about -14 dB and an injection locking ranges of 3 GHz and 2.2 GHz for two lasers, respectively. The current applied to the gain section of each SG-DBR laser fell in a range between 80 mA and 100 mA . The current to each SOA following corresponding laser lied in a range between 70 mA and 90 mA . By finely tuning the free running wavelengths of two SG-DBR lasers, the wavelength of the external laser and the RF modulation frequency, two SG-DBR lasers could be injection locked by the two pumps. During the measurements, the wavelength of the incident signal was tuned to lie in a range between 1560 nm and 1562 nm , and the frequency of the RF signal was set to be about 9 GHz . Then the pumps and the signal were sent to the NL-SOA with a current of about 90 mA . The total input power to the NL-SOA was about -1 dBm , which was high enough to saturate the NL-SOA because the NL-SOA started saturation at -9 dBm . Once the SOA was saturated, the spontaneous emission noise and PIA were suppressed. The output of the NL-SOA was sent to the optical spectrum analyzer for recording the power of the signal as its phase was changed for PSA demonstration. The input saturation power was -9 dBm . (The PIA gain is much smaller with input powers approaching the input saturation power).

The optical spectra at the input and the output of the NL-SOA were measured to record the signal power change caused by the PSA. The optical spectrum of the input light

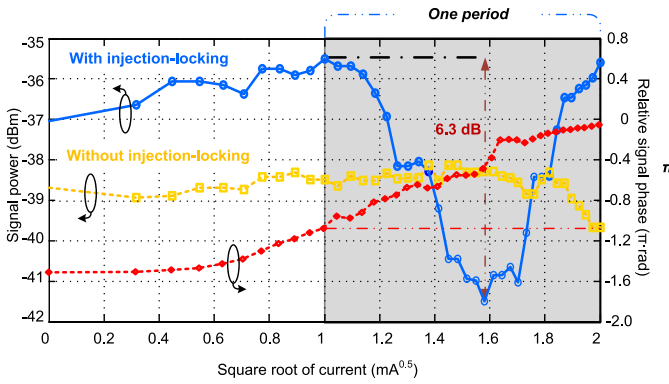


Fig. 24. Measured relationship among the signal power, the signal phase and the square root of the current applied to the phase tuner.

waves was equivalently obtained by monitoring the output of the tap port by using the optical spectrum analyzer. The measured optical spectra are shown in Fig. 23. Fig. 23 (a) is the optical spectrum of the input light waves. As we can see, there are two dominant pumps and one suppressed signal in the middle. Other small peaks are high-order sidebands from external modulation. Fig. 23(b) is the optical spectrum of the light wave after the PSA when the signal phase was changed by tuning the phase tuner current. Comparing with Fig. 23(a), we can clearly see the FWM and the idler waves outside the two pumps. In addition, we can see that the signal was amplified or attenuated as the phase tuner current was adjusted. Such a current- or phase-dependent signal power change could be caused by the PSA.

To specifically demonstrate and evaluate the PSA, the measured signal power at the output of the SOA with respect to the square root of the phase tuner current was measured, which is shown in Fig. 24. Again, the abscissa variable is set to be the square root of the phase tuner current because the signal power after PSA varies with the signal phase, which is known to vary linearly with the square root of the phase tuner current. For comparison, the measured signal power without injection locking and the measured relative phase change are shown in Fig. 24 as well. As can be seen from Fig. 24, when injection locking was inactive and two lasers were in free-running modes, there was no PSA due to random phase drifting among the pumps and the signal waves. Once the injection locking was enabled, however, there was no obvious PSA or phase change of the signal until after the current was larger than 1 mA, which is caused by the phase delay we mentioned before. As the current was further increased, these traps are filled and phase-dependent signal gain appeared. Overall, 1 mA^{0.5} gives π phase shift of the signal and one period oscillation of the signal. Clearly, such a signal power oscillation over one π instead of 2π phase indicates that the signal power change was caused by the PSA instead of the signal interference. The measured signal power curve shows that approximate 6.3 dB extinction of phase-sensitive on-chip gain was achieved.

To demonstrate multiple periods of a PSA gain curve, we chose another PSA chip and repeated the same procedures but increased the phase tuner current. The results are shown

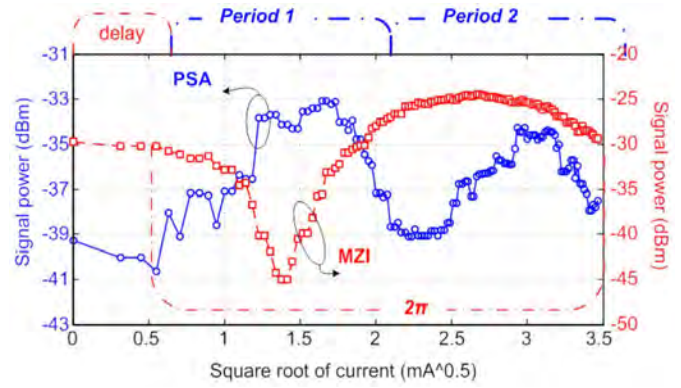


Fig. 25. Measured signal power at the output of the NL-SOA when the chip is configured as a PSA chip and the signal power at the output of the tap when the chip is configured as an MZI.

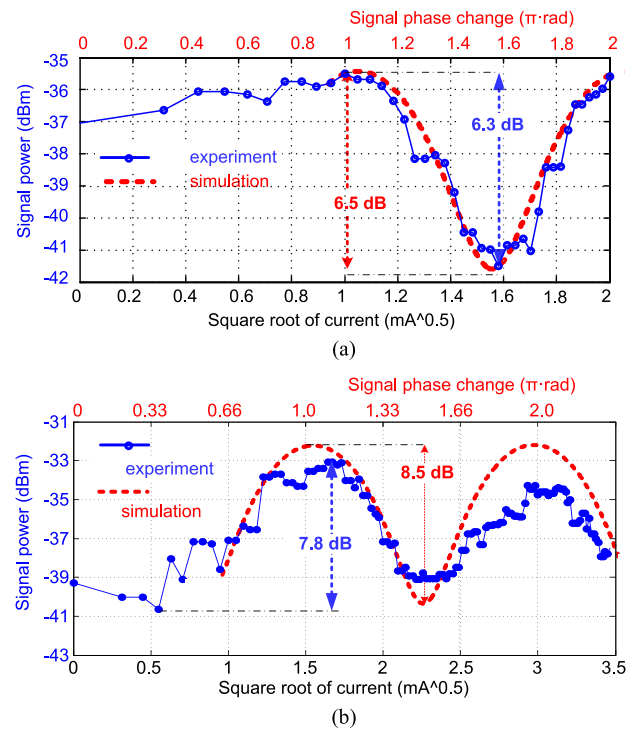


Fig. 26. Comparisons of the measured PSA gain curve and the theoretical simulation. (a) One-period PSA gain curve with 6.3 dB experimental and 6.5 dB theoretical results; (b) two-period PSA gain curve with 7.8 dB experimental and 8.5 dB theoretical results.

in Fig. 25. The blue curve is the measured signal power change at the output of the NL-SOA caused by the PSA; while the red curve is the measured signal power at the output of the on-chip MZI. The blue curve shows a PSA gain curve of two periods, and the red curve indicates that approximately, 1.5 mA^{0.5} gives one π phase shift. Amplitude reduction of the second period was probably caused by the power reduction of the input pumps as the phase tuner current was increased.

A theoretical simulation of the PSA gain based on coupled differential equations [17] and the model provided by Prof. Mecozzi is presented in Fig. 26(a), showing a 6.5 dB extinction ratio of the phase-sensitive gain, which agrees well with the experimental result over this current and

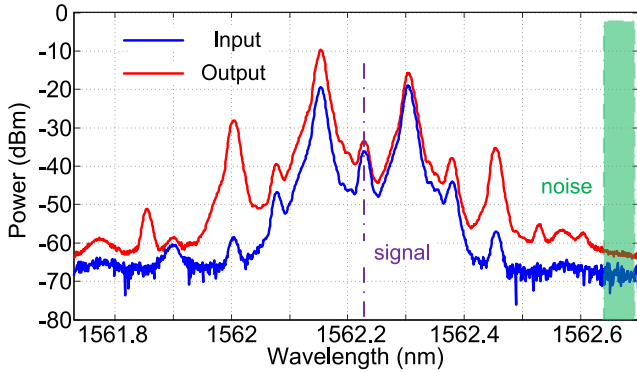


Fig. 27. The measured input and the output optical spectra of the NL-SOA.

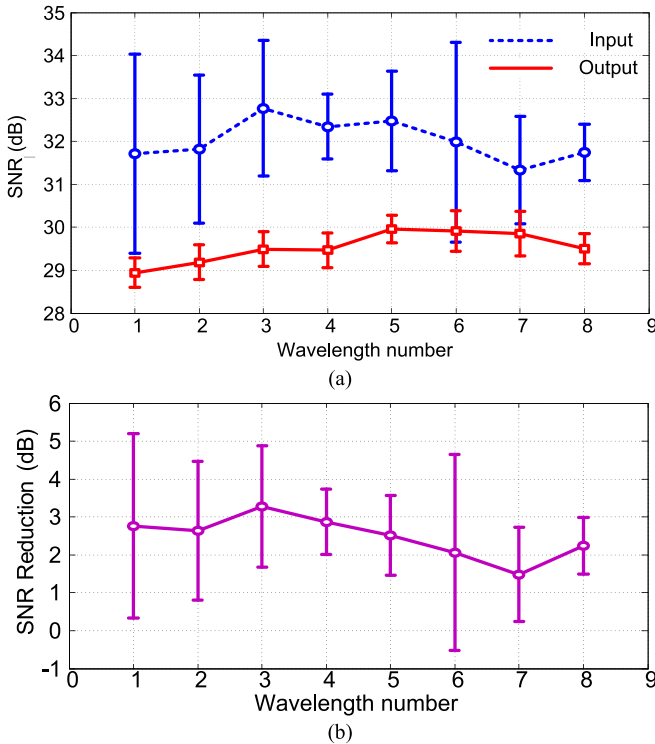


Fig. 28. (a) Measured SNR of the input and the output light waves of the NL-SOA; (b) calculated SNR reduction.

phase-shift range. Simulation results for the second chip were obtained as well and presented in Fig. 26(b), showing a two-period PSA gain curve. Again, good agreement was observed.

The added noise of the PSA is another important aspect. Thus, the input and the output SNR of the PSA was estimated from the measured optical spectrum of light waves at the input and the output port of the NL-SOA. Please note that the input optical spectrum was equivalently measured at the output of the tap port. The signal level was the power at the signal wavelength. The noise level could not be easily measured at exactly the same wavelength, so it was measured at eight different wavelengths that were 0.5 nm away from the signal wavelength where the background spectrum was relatively flat, as shown in Fig. 27.

At each wavelength, the measured SNR was obtained through 10 times iteration, as shown in Fig. 28(a), and

the difference was calculated and shown in Fig. 28(b). The smallest difference in SNR was 1.5 dB and overall averaged decrease in SNR was about 2.5 dB.

VII. CONCLUSION

Based on an InP/InGaAsP, platform we have fabricated and characterized different SOAs, and based on a highly saturated SOA, we have successfully fabricated and demonstrated the first monolithic dual-pumped PSA chip. The amplified spontaneous emission noise of the SOA was suppressed significantly due to the high saturation which restricts PIA, while high nonlinearity of the SOA benefited the PSA.

On the chip, two tunable laser pumps coherently injection-locked from sidebands of an external modulated tone were generated to enable signal-degenerate dual-pumped phase-sensitive amplification in a highly saturated semiconductor optical amplifier. Phase-sensitive amplification was experimentally achieved with approximately 6.3 dB and 7.8 dB extinction of phase-sensitive on-chip gain using two different chips. Theoretical simulations based on coupled differential equations were performed and agreed well with experimental results. The Signal-to-Noise Ratio degradation of the phase-sensitive amplification chip was also estimated, and averaged 1.5 – 3.1 dB.

However, compared with high nonlinear fiber, the PSA gain is still small. The investigation of the chip-scale PSA is not comprehensive due to low current density to the NL-SOA and low incident pump power to the NL-SOA. Increasing the current density to the NL-SOA to increase the PSA gain more likely causes more heating problems, which either leads to unstable injection locking or reducing the laser pump power or possible pump interference. In addition, limited pump power to the NL-SOA restricts the saturation level of the NL-SOA, which makes it difficult to evaluate the PSA effect given a deeply saturated SOA. The PSA chip layout can be improved to allow more incident pump powers to the NL-SOA, such as using directional couplers in the PSA chip.

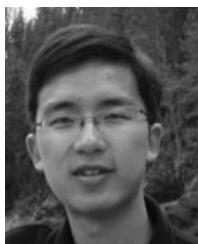
REFERENCES

- [1] R. Slavík *et al.*, “All-optical phase and amplitude regenerator for next-generation telecommunications systems,” *Nature Photon.*, vol. 4, no. 10, pp. 690–695, Oct. 2010.
- [2] Z. Tong *et al.*, “Towards ultrasensitive optical links enabled by low-noise phase-sensitive amplifiers,” *Nature Photon.*, vol. 5, no. 7, pp. 430–436, 2011.
- [3] C. M. Caves, “Quantum limits on noise in linear amplifiers,” *Phys. Rev. D*, vol. 26, no. 8, pp. 1817–1839, 1982.
- [4] Y. Mu and C. M. Savage, “Parametric amplifiers in phase-noise-limited optical communications,” *J. Opt. Soc. Amer. B*, vol. 9, no. 1, pp. 65–70, 1992.
- [5] H. P. Yuen, “Reduction of quantum fluctuation and suppression of the Gordon–Haus effect with phase-sensitive linear amplifiers,” *Opt. Lett.*, vol. 17, no. 1, pp. 73–75, 1992.
- [6] J. N. Kutz, W. L. Kath, R.-D. Li, and P. Kumar, “Long-distance pulse propagation in nonlinear optical fibers by using periodically spaced parametric amplifiers,” *Opt. Lett.*, vol. 18, no. 10, pp. 802–804, 1993.
- [7] P. C. Becker, N. A. Olsson, and J. R. Simpson, *Erbium-doped Fiber Amplifiers: Fundamentals and Technology*. San Diego, CA, USA: Academic, 1999.
- [8] K. J. Lee *et al.*, “Phase sensitive amplification based on quadratic cascading in a periodically poled lithium niobate waveguide,” *Opt. Exp.*, vol. 17, no. 22, pp. 20393–20400, 2009.

- [9] T. Umeki, M. Asobe, and H. Takenouchi, "In-line phase sensitive amplifier based on PPLN waveguides," *Opt. Exp.*, vol. 21, no. 10, pp. 12077–12084, 2013.
- [10] M. E. Marhic, C. H. Hsia, and J.-M. Jeong, "Optical amplification in a nonlinear fibre interferometer," *Electron. Lett.*, vol. 27, no. 3, pp. 210–211, 1991.
- [11] A. D. Ellis and S. Sygletos, "Phase sensitive signal processing using semiconductor optical amplifiers," in *Proc. OFC*, 2013, p. OW4C.1.
- [12] D. J. Moss, R. Morandotti, A. L. Gaeta, and M. Lipson, "New CMOS-compatible platforms based on silicon nitride and Hydex for nonlinear optics," *Nature Photon.*, vol. 7, pp. 597–607, Aug. 2013.
- [13] A. Takada and W. Imajuku, "In-line optical phase-sensitive amplifier employing pump laser injection-locked to input signal light," *Electron. Lett.*, vol. 34, no. 3, pp. 274–276, Feb. 1998.
- [14] W. Imajuku and A. Takada, "In-line optical phase-sensitive amplifier with pump light source controlled by optical phase-lock loop," *J. Lightw. Technol.*, vol. 17, no. 4, pp. 637–646, Apr. 1999.
- [15] L. A. Coldren, G. A. Fish, Y. Akulova, J. S. Barton, L. Johansson, and C. W. Coldren, "Tunable semiconductor lasers: A tutorial," *J. Lightw. Technol.*, vol. 22, no. 1, pp. 193–202, Jan. 2004.
- [16] A. D'Ottavi *et al.*, "Four-wave mixing in semiconductor optical amplifiers: A practical tool for wavelength conversion," *IEEE J. Sel. Topics Quantum Electron.*, vol. 3, no. 2, pp. 522–528, Apr. 1997.
- [17] A. Mecozzi, "Analytical theory of four-wave mixing in semiconductor amplifiers," *Opt. Lett.*, vol. 19, no. 12, pp. 892–894, 1994.
- [18] J. W. Raring *et al.*, "Advanced integration schemes for high-functionality/high-performance photonic integrated circuits," *Proc. SPIE*, vol. 6126, p. 61260H, Feb. 2006.
- [19] E. J. Skogen, J. S. Barton, S. P. Denbaars, and L. A. Coldren, "A quantum-well-intermixing process for wavelength-agile photonic integrated circuits," *IEEE J. Sel. Topics Quantum Electron.*, vol. 8, no. 4, pp. 863–869, Jul./Aug. 2002.



Wangzhe Li received the Ph.D. degree from the University of Ottawa, Canada, in 2013, with a focus on photonic generation of microwave and millimeter-wave signals. He joined the University of California at Santa Barbara, CA, as a Post-Doctoral Scholar, where he has been involved in integrated optical phase-sensitive amplifiers.



Mingzhi Lu received the B.S. degree in electrical engineering from Southeast University, Nanjing, China, in 2008, and the M.S. and Ph.D. degrees in electrical and computer engineering from the University of California at Santa Barbara, CA, in 2010 and 2013, respectively. He was with the University of California at Santa Barbara as a Post-Doctoral Researcher from 2013 to 2014. He is currently with Infinera Corporation as a Senior PIC Development Engineer. His Ph.D. and post-doctoral research is mainly focused on III–V photonic integration technology, and integrated coherent optical systems, such as integrated optical phase-locked loops, coherent LIDAR, optical synthesizer, and phase-sensitive amplifiers. He is currently focusing on the next-generation larger-scale photonic integrated circuits for future communication applications.



Antonio Mecozzi (F'03) worked for 15 years with the Optical Communication Division of Fondazione Ugo Bordoni, Rome. He was a Visiting Scientist with the EECS Department and the Research Laboratory of Electronics, Massachusetts Institute of Technology, from 1991 to 1992. He is a Professor and the Director of the Department of Physical and Chemical Sciences with the University of L'Aquila, Italy. He holds numerous patents and over 160 publications in refereed scientific journals. His areas of interest include studies on soliton transmission, laser mode-locking, nonlinear propagation in fiber, polarization mode dispersion, physics and applications of semiconductor optical amplifiers, optical amplification, and noise. He is a fellow of the Optical Society of America.



Michael Vasilyev received the M.S. degree in physics from the Moscow Institute of Physics and Technology, Russia, in 1993, and the Ph.D. degree in electrical engineering from Northwestern University, Evanston, IL, in 1999, with a focus on quantum properties of parametric amplifiers and solitons in optical fibers. Before joining the University of Texas at Arlington in 2003, where he is currently a Professor of Electrical Engineering, he was with Corning Inc., Somerset, NJ, as a Senior Research Scientist, investigating noise and nonlinearities in optical fibers and Raman and erbium-doped amplifiers. He has authored over 54 journal and over 130 conference papers, and holds ten U.S. patents. His interests concentrate on experimental and theoretical nonlinear and quantum optics and nanophotonics, with applications to classical and quantum information processing, ultra-sensitive measurements, and remote sensing. He is a fellow of OSA and a Senior Member of the IEEE Photonics and Communication Society. He was a recipient of the 2008 DARPA Young Faculty Award. He has served as a Chair or Member of the Technical Committees for many conferences, including the IEEE Summer Topicals, CLEO, OFC, Photonics West, and FiO, and is an Associate Editor of the IEEE JOURNAL OF LIGHTWAVE TECHNOLOGY/*OSA Journal of Lightwave Technology*.



Shamsul Arafin received the B.Sc. degree in electrical and electronics engineering from the Bangladesh University of Engineering and Technology (BUET), Bangladesh, in 2005, the M.Sc. degree in communication technology from Universität Ulm, Germany, in 2008, and the Ph.D. degree from the Walter Schottky Institut, Technische Universität München, Germany, in 2011. He was a Post-Doctoral Research Scholar with the Device Research Laboratory, University of California at Los Angeles, USA. In 2012, he was with the Nanophotonics Group, Electrical and Computer Engineering Department, McGill University, as a Post-Doctoral Fellow. He is currently an Assistant Project Scientist with the University of California at Santa Barbara, USA, under the supervision of Prof. L. A. Coldren.



Danilo Dadić received the B.S. degree in physics from the University of California at Los Angeles, CA, in 2014. He is currently pursuing the M.S./Ph.D. degree with the Electrical and Computer Engineering Department, University of California at Santa Barbara, CA. His research focus is on the design, fabrication, and characterization of photonic integrated circuits closely integrated with electronic integrated circuits.



Leif A. Johansson (M'04) received the Ph.D. degree in engineering from University College London, London, U.K., in 2002. He has been a Research Scientist with the University of California at Santa Barbara, and is the Founder of Freedom Photonics. His current research interests include design and characterization of integrated photonic devices for analog and digital applications and analog photonic systems and subsystems.



Larry A. Coldren (S'67–M'72–SM'77–F'82) received the Ph.D. degree in electrical engineering from Stanford University, Stanford, CA, in 1972. After 13 years in the research area with Bell Laboratories, he joined the University of California at Santa Barbara (UCSB) in 1984. From 2009 to 2011, he served as the Dean of the College of Engineering. In 1990, he co-founded Optical Concepts, later acquired as Gore Photonics, to develop novel VCSEL technology, and, in 1998, he co-founded Agility Communications, later acquired by JDSU, to develop widely-tunable integrated transmitters. At UCSB, he has worked on multiple-section widely-tunable lasers and efficient vertical-cavity surface-emitting lasers (VCSELs). More recently, his group has developed high-performance InP-based photonic integrated circuits and high-speed VCSELs. He is currently the Fred Kavli Professor of Optoelectronics and Sensors and holds appointments with the Department of Materials and the Department of Electrical and Computer Engineering, UCSB. He has authored or co-authored over a thousand journal and conference papers, co-authored eight book chapters, a widely used textbook, and holds 65 patents. He is a fellow of OSA and IEE, and a member of the National Academy of Engineering. He was a recipient of the 2004 John Tyndall Award, the 2009 Aron Kressel Award, the 2014 David Sarnoff Award, and the 2015 IPRM Award.

Efficient and Accurate Modeling of Multiwavelength Propagation in SOAs: A Generalized Coupled-Mode Approach

Cristian Antonelli, Antonio Mecozzi, *Fellow, IEEE, Fellow, OSA*, Wangzhe Li, and Larry A. Coldren, *Life Fellow, IEEE, Fellow, OSA*

Abstract—We present a model for multiwavelength mixing in semiconductor optical amplifiers (SOAs) based on coupled-mode equations. The proposed model applies to all kinds of SOA structures, takes into account the longitudinal dependence of carrier density caused by saturation, it accommodates an arbitrary functional dependencies of the material gain and carrier recombination rate on the local value of carrier density, and is computationally more efficient by orders of magnitude as compared with the standard full model based on space-time equations. We apply the coupled-mode equations model to a recently demonstrated phase-sensitive amplifier based on an integrated SOA and prove its results to be consistent with the experimental data. The accuracy of the proposed model is certified by means of a meticulous comparison with the results obtained by integrating the space-time equations.

Index Terms—Nonlinear optics, semiconductor optical amplifiers, wave mixing.

I. INTRODUCTION

SEMICONDUCTOR optical amplifiers (SOAs) have been in the spotlight for many years, attracting ever growing interest in multiple areas of applications. These include all-optical signal processing in fiber-optic communication networks, cost-effective local area transmission, and, more recently, integrated silicon photonics, where SOAs are the building blocks for the implementation of large-scale integrated photonic circuits. Many of these applications rely on the mixing of the wavelength components of the propagating electric field, and their theoretical study can be performed by numerically integrating the coupled nonlinear equations describing the evolution of the electric field envelope in the longitudinal direction along the SOA, and the temporal carrier dynamics [1], [2]. Obviously, this approach is not suitable for the efficient design of an SOA, owing to the intensive computational effort that it involves. The

search for computationally efficient and analytically tractable models has yield the formulation of what is sometimes referred to as a *reduced model* for the nonlinear SOA response [3], where the space-time equations reduce to a single ordinary differential equation [3], suitable for the analytic study of multi-wave mixing (see, e.g., [3]–[5]). The formulation of a reduced model hinges upon two major assumptions. The first is that the spontaneous carrier recombination rate is proportional to the carrier spatial density, and the second is that the material gain also depends linearly on the carrier density. These assumptions emanate from early studies of semiconductor lasers. Indeed, in lasers the carrier density dynamics is characterized by small deviations from a steady state value which is set by the threshold condition of gain equalling the cavity loss. The small deviations around this value are only caused by amplified spontaneous emission (ASE) and by some spatial hole burning, which is however of little significance because in most structures the intra-cavity optical intensity is only moderately inhomogeneous. Consequently, in laser structures, gain and spontaneous emission rate can be accurately described by a linearized expression around the steady state carrier density. Early studies on SOA structures also used linear expressions for gain and carrier recombination, and in this case the linearization, albeit less accurate, found its ground on its simplicity and, more importantly, on the limited gain of legacy SOAs, which implied a limited longitudinal inhomogeneity of the optical field in the optical waveguide.

Unfortunately, these assumptions do not reflect the characteristics of modern SOAs, as is clarified in what follows. Modern SOAs may have linear gain in excess to 40 dB, implying a pronounced longitudinal inhomogeneity of the field intensity and hence of gain saturation. This may cause, in some cases, that the gain is only slightly saturated at the waveguide input, whereas it is almost zero at the waveguide output, where saturation is so high that the carrier density approaches its transparency value. When this is the case, a linear expression for the gain is reasonably accurate only if the gain does not deviate significantly from the linear expansion around the transparency carrier density over a range of values. The nowadays widely accepted forms for the dependence of the material gain on carrier density do not meet this requirement, because over such wide range of carrier density values the nonlinearity cannot be neglected, especially in quantum-well (QW) SOAs devices [6]. This makes the use of linear forms for the gain not an option for an accurate and quantitative description of the SOA dynamics. In addition, advances in material fabrication have made in modern devices the

Manuscript received October 12, 2015; revised January 15, 2016; accepted January 15, 2016. Date of publication January 17, 2016; date of current version March 18, 2016. This work was supported by DARPA under Project W911NF-14-1-0249. The work of C. Antonelli and A. Mecozzi was supported by the Italian Ministry of University and Research under ROAD-NGN Project (PRIN 2010–2011), and under Cipe resolution 135 (Dec. 21, 2012), project INnovating City Planning through Information and Communication Technologies.

C. Antonelli and A. Mecozzi are with the Department of Physical and Chemical Sciences, University of L'Aquila, L'Aquila 67100, Italy (e-mail: cristian.antonelli@univaq.it; antonio.mecozzi@univaq.it).

W. Li and L. Coldren are with the Departments of Electrical and Computer Engineering and Materials, University of California, Santa Barbara, CA 93106 USA (e-mail: teralee008@gmail.com; coldren@ece.ucsb.edu).

Color versions of one or more of the figures in this paper are available online at <http://ieeexplore.ieee.org>.

Digital Object Identifier 10.1109/JLT.2016.2519240

contribution of defect-induced carrier recombination, which is proportional to the carrier density N , negligible, with the consequence that spontaneous carrier recombination is dominated primarily by radiative recombination, whose rate is proportional to N^2 , and secondarily by Auger recombination, whose rate is proportional to N^3 [6]. This reality makes the linearization of the spontaneous recombination rate also a questionable approximation. All these arguments together suggest that the accuracy of models of the nonlinear SOA response based on linearization of the carrier recombination rate and gain may be, in state-of-the-art devices, highly inaccurate.

A natural approach to the study of wave mixing in SOAs, which closely reminds coupled-mode theories, is the one based on the derivation of evolution equations for the complex amplitudes of the field frequency components. Somewhat surprisingly, studies of wave mixing in modern SOAs (that is, SOAs characterized by a nonlinear dependence of the recombination rate and material gain on carrier density) based on this approach seem to be absent in the literature. In a couple of recent papers [7], [8], the authors assume a linear gain and a polynomial recombination rate, as it would be appropriate for bulk SOAs. However, they express the recombination rate as $R(N) = N/\tau_c(N)$, where $\tau_c(N) = N/R(N)$ has the meaning of an equivalent spontaneous carrier lifetime and, in the derivation of the coupled-mode equations, they replace $\tau_c(N)$ with some time- and space-independent value. This makes, again, the assumed carrier recombination rate linear.

Another distinctive assumption of all existing coupled-mode approaches to multi-wave mixing in SOAs is that the carrier density modulation induced by the mixing is characterized by a single harmonic component [8]. This is a reasonable assumption when a single frequency component is dominant over the others, like for instance, in four-wave mixing (FWM) experiments where a single pump and a frequency-detuned weak signal are injected into the SOA. On the contrary, this assumption is not satisfied when multiple frequency components, detuned by a few gigahertz, have comparable intensities. This configuration characterizes for instance experiments where two strong pumps are injected at frequencies $-\Omega + \omega_0$ and $\Omega + \omega_0$, and one is interested in the amplification of a weak signal injected at the central frequency ω_0 . In this case, the strongest carrier modulation occurs at the beat frequency 2Ω between the two strong pumps, but the signal amplification is mainly affected by the, possibly weaker, carrier modulation at frequency Ω . This configuration recently became of great interest because it describes the operation of a relevant class of SOA-based phase sensitive amplifiers (PSAs) [9]–[13].

In this paper, we derive coupled-mode equations describing multi-wavelength mixing in SOAs characterized by arbitrary functional dependencies of the recombination rate and material gain on carrier density. These include both QW and bulk SOAs. The proposed model, which in what follows we refer to as the *couple-mode model*, takes into account the frequency dependence of the material gain, as well as all orders of the waveguide dispersion, and accommodates input optical waveforms consisting of arbitrary combinations of multiple frequency

components.¹ The implementation of the model is illustrated in detail in the case of a QW SOA characterized by a logarithmic dependence of the optical gain on the carrier density N , and by a cubic-polynomial carrier recombination rate $R(N)$. The accuracy of the coupled-mode model is successfully tested (unlike in previous related studies) by means of a meticulous comparison with the results obtained by integrating the space-time equations of the SOA full model. Remarkably, owing to their inherent simplicity, the coupled-mode equations imply computational costs by orders of magnitude smaller than those required by the space-time equations, thus enabling the efficient characterization of multi-wave mixing in SOA structures, which would be otherwise highly impractical. We then apply the derived coupled-mode equations to studying the operation of a recently demonstrated dual-pumped PSA based on an integrated QW SOA [11]. We prove the results to be consistent with the experimental data, and confirm the excellent agreement with the results obtained by using the full SOA model.

II. COUPLED-MODE EQUATIONS FOR MULTI-WAVELENGTH PROPAGATION IN SOAs

We denote by $E(z, t)$ the slowly-varying complex envelope of the electric field propagating in the SOA in the temporal reference frame that accommodates the field group velocity v_g , corresponding to the real field

$$\mathcal{E}(z, t) = \text{Re} \left[E \left(z, t - \frac{z}{v_g} \right) e^{-i[\omega_0 t - \beta(\omega_0)z]} \right], \quad (1)$$

with ω_0 being the optical frequency. The field envelope E is normalized so that that $|E|^2$ is the optical power flowing through the transverse waveguide section. It is related to the photon flux P in photons per unit time and area through the relation

$$|E|^2 = \hbar\omega_0 S_{\text{mod}} P, \quad (2)$$

where $S_{\text{mod}} = S/\Gamma$ is the modal area of the waveguide, with S denoting the effective SOA area and Γ the optical confinement factor. The evolution of $E(z, t)$ along the SOA is governed by the familiar equation

$$\frac{\partial E}{\partial z} = \frac{1}{2} [(1 - i\alpha)\Gamma\hat{g} - \alpha_{\text{int}}] E + i\hat{\beta}E + r_{\text{sp}}, \quad (3)$$

¹We consider here only the nonlinearity that comes from carrier modulation, neglecting ultrafast nonlinearity arising from carrier heating, two photon absorption and spectral hole burning. This choice has been motivated to keep the analysis simple, and also because we are interested to cases where nonlinearity is large enough to be used in all-optical processing applications or to be an issue in applications where linearity is sought for. In these cases, the frequency detuning does not exceed a few tens of gigahertz, and in this detuning range the nonlinear modulation is mostly caused by carriers. The inclusion of ultrafast processes, however, does not pose any conceptual difficulties, and can be done along the lines of ref. [14] assuming that the gain depends on quantities other than carrier density, like, e.g., the carrier temperature for carrier heating, or the energy-resolved population of carriers for spectral hole burning, and assuming a linear decay process of these quantities towards their steady state values. The effect of carrier capture and escape processes in QW structures can be similarly taken into account by considering two distinct carrier densities, one for the confinement region and one for the QW. Also these processes, however, become of relevance for a pump-probe frequency detuning of the order of 100 GHz [15], much higher than the range of values considered here.

where α is the Henry factor, α_{int} is the SOA internal loss coefficient, and r_{sp} is the spontaneous emission noise term. By \hat{g} and $\hat{\beta}$ we denote the material gain operator and the wavenumber operator. The operator formalism allows us to conveniently accommodate the frequency dependence of the gain as well as the waveguide dispersion to any order. Within this formalism the two operators can be expressed as

$$\hat{g} = \sum_{m=0}^{\infty} \frac{1}{m!} \frac{\partial^m g(N, \omega_0)}{\partial \omega_0^m} \left(i \frac{\partial}{\partial t} \right)^m \quad (4)$$

$$\hat{\beta} = \sum_{m=2}^{\infty} \frac{1}{m!} \frac{d^m \beta(\omega_0)}{d\omega_0^m} \left(i \frac{\partial}{\partial t} \right)^m, \quad (5)$$

where $g(N, \omega)$ is the gain coefficient expressed as a function of the carrier density N and the optical frequency ω , and $\beta(\omega)$ is the frequency-dependent field propagation constant. The expressions for \hat{g} and $\hat{\beta}$ in Eqs. (4) and (5) are obtained by expanding $g(N, \omega)$ and $\beta(\omega)$ around the carrier frequency ω_0 . The fact that the sum in Eq. (5) starts from $n = 2$ is consistent with the definition of $E(z, t)$ in Eq. (1), which already accounts for the effect of $\beta(\omega_0)$ and $d\beta(\omega_0)/d\omega_0 = 1/v_g$.

The spontaneous emission noise term r_{sp} is modeled as a zero-mean, complex phase independent random process. It depends explicitly on the carrier density, besides time and space, i.e., $r_{\text{sp}} = r_{\text{sp}}(N, t; z)$. Its correlation function is [16]

$$\mathbb{E} [r_{\text{sp}}^*(N, t; z) r_{\text{sp}}(N, t'; z')] = \hbar\omega_0 R_{\text{sp}}(N, t - t') \delta(z - z'), \quad (6)$$

where by the symbol \mathbb{E} we denote ensemble averaging. Here the term $\delta(z - z')$ accounts for the fact that different longitudinal waveguide sections provide statistically independent contributions to the noise term, and [6]

$$R_{\text{sp}}(N, t' - t) = \int e^{-i(\omega - \omega_0)(t' - t)} n_{\text{sp}}(N, \omega) \Gamma g(N, \omega) \frac{d\omega}{2\pi}, \quad (7)$$

is the spontaneous emission rate into the waveguide mode and in the field propagation direction, with n_{sp} denoting the population inversion factor [6]. Spontaneous emission is a small perturbation of the propagating field, so that we may safely replace N with its temporal average, thus neglecting the effect of its small fluctuations around this value. Within this approximation the process of spontaneous emission can be modeled as a stationary process in time.

The equation for the carrier density is

$$\frac{\partial N}{\partial t} = R_J - R_{\text{rad}} - R_{\text{nr}}, \quad (8)$$

where the meaning of each of the terms at the right-hand side of the equation is discussed in what follows. The term

$$R_J = \frac{J w_a L}{V} = \frac{J}{ed}, \quad (9)$$

is the carrier injection rate into the active volume $V = SL = w_a dL$, where w_a is the active region width, L is the active region length, and d is the active region thickness. The term $R_{\text{rad}} = R_{\text{in}} + R_{\text{out}}$ is the radiative recombination rate related to

processes in which the recombination of one carrier is associated to the generation of one photon. The term R_{in} refers to processes in which emission occurs into the guided mode. By definition, this implies that $R_{\text{in}}(N)$ is related to the flux of photons flowing in the waveguide P through the balance relation

$$R_{\text{in}} S dz = S_{\text{mod}} [P(z + dz) - P(z)], \quad (10)$$

which yields

$$R_{\text{in}} = \frac{1}{\Gamma} \frac{\partial P}{\partial z}. \quad (11)$$

The processes accounted for by R_{in} includes stimulated emission and spontaneous emission within the waveguide mode (which is only a fraction of the overall spontaneous emission). The term $R_{\text{out}}(N)$ is the rate of recombinations accompanied by spontaneous emission of photons outside the waveguide mode and it can be expressed as $R_{\text{out}} = BN^2 - R_{\text{sp},\text{in}}$, where the term BN^2 is known to be an excellent approximation of the total rate of recombinations associated with spontaneous emission (inside and outside the waveguide mode) [6], and $R_{\text{sp},\text{in}}$ accounts for the rate of recombinations that produce spontaneous emission in the waveguide mode, namely it accounts for the contribution to the carrier recombination rate of the noise term r_{sp} that appears in Eq. (3). Finally, the term R_{nr} is the recombination rate of non-radiative processes, which we express as $R_{\text{nr}} = AN + CN^3$, where the linear contribution AN is mostly due to defect-induced recombination, and the cubic contribution CN^3 to Auger recombination.² By combining the various mechanisms, Eq. (8) becomes

$$\frac{\partial N}{\partial t} = -R(N) + \frac{J}{ed} + R_{\text{sp},\text{in}} - \frac{1}{\hbar\omega_0 S} \frac{\partial |E|^2}{\partial z}, \quad (12)$$

where by $R(N)$ we denote the familiar recombination rate³

$$R(N) = AN + BN^2 + CN^3. \quad (13)$$

By expanding the derivative $\partial |E|^2 / \partial z$ and using Eq. (3), Eq. (12) assumes the form

$$\frac{\partial N}{\partial t} = -R(N) + \frac{J}{ed} - \frac{1}{\hbar\omega_0 S} \text{Re} [E^* (1 - i\alpha) \Gamma \hat{g} E], \quad (14)$$

where we used the fact that $\hat{\beta}$ is a Hermitian operator, and hence it does not contribute to $\partial |E|^2 / \partial z$. The last term at the right-hand side of Eq. (14) reduces to the familiar form $\Gamma g |E|^2 / \hbar\omega_0 S$ if the gain coefficient is assumed to be frequency independent. Note that in Eq. (14), the term $R_{\text{sp},\text{in}}$ disappears because it

²We note that, while the resulting cubic polynomial expression $AN + BN^2 + CN^3$ has been shown to fit very well the experimental data in most cases [6], the one-to-one correspondence between the three terms of the polynomial and the three recombination mechanisms is not always as definite as is illustrated in the main text. For instance, in the case of non-parabolic bands (the normal case), radiative recombination is also non-parabolic and is best modeled with a bit of linear component; carrier leakage (due to finite QW barriers) has an exponential dependence and requires a polynomial fit, affecting the numerical values of A , B , and C .

³This expression of $R(N)$ is widely established and is given here for consistency with previous studies. We stress, however, that the analysis that follows does not make use of it explicitly, and rather applies to arbitrary expressions of $R(N)$.

cancel with an opposite term that—by definition—comes from $\partial|E|^2/\partial z$.

We note that Eqs. (3) and (14) can be generalized so as to include the field polarization in the analysis. While this task is rather straightforward and does not involve any conceptual challenge, we intentionally ignore polarization-related issues in order to keep the focus on the main objective of this work, which is the study of multi-wavelength propagation.

We express the multi-wavelength electric field and the carrier density as follows,

$$E(z, t) = \sum_k E_k(z) e^{-ik\Omega t}, \quad (15)$$

$$N(z, t) = N_0(z) + \sum_k \Delta N_k(z) e^{-ik\Omega t}, \quad (16)$$

where the coefficients ΔN_k must satisfy the equality $\Delta N_{-k}(z) = \Delta N_k^*(z)$ for $N(z, t)$ to be real. The term $N_0(z) + \Delta N_0(z)$ is the z -dependent time-independent value of the carrier density that characterizes the system when it achieves its stationary state, and $N_0(z)$ is defined as the solution of

$$\frac{J}{ed} = R(N_0) + \frac{\Gamma}{\hbar\omega_0 S} \sum_k g(N_0, \omega_k) |E_k|^2. \quad (17)$$

For values of the frequency spacing $\Omega/2\pi$ that exceed the SOA modulation bandwidth, the temporal fluctuations of $N(z, t)$ around its stationary value are filtered by the carrier dynamics and hence they can be treated within a perturbation approach. A consequence of this situation is that the deviation $\Delta N_0(z)$ of the stationary carrier density value from $N_0(z)$ is also a perturbation, and is small compared to $N_0(z)$. In this framework, all carrier-density dependent quantities that appear in Eqs. (3) and (14) can thus be expanded to first order with respect to $\Delta N = N - N_0$, namely

$$R(N) = R(N_0) + \frac{\Delta N}{\tau(N_0)}, \quad (18)$$

$$g(N, \omega) = g(N_0, \omega) + g_N(N_0, \omega) \Delta N, \quad (19)$$

where by the subscript N we denote differentiation with respect to N . The quantity

$$\tau(N_0) = R_N(N_0)^{-1} = \left[\frac{dR(N)}{dN} \Big|_{N=N_0} \right]^{-1}, \quad (20)$$

is the spontaneous carrier lifetime, and

$$g_N(N_0, \omega) = \frac{\partial g(N, \omega)}{\partial N} \Big|_{N=N_0}, \quad (21)$$

is the differential gain. We stress that *these are z -dependent quantities*, owing to the fact that $N_0 = N_0(z)$, and hence their values evolve along the SOA. We also notice that the effective carrier lifetime governing the dynamics of carrier modulation around the steady state value is the *differential* carrier lifetime $\tau(N_0)$ given in Eq. (20) and also introduced in [17], and not the *total* carrier lifetime $\tau_c(N_0) = N_0/R(N_0)$ used in Refs. [7]

and [8]. The difference between these two quantities is approximately a factor of 2 when the radiative bimolecular recombination BN^2 is the dominant contribution to $R(N)$, or 3 when the Auger recombination CN^3 is dominant. By inserting Eqs. (18) and (19) into Eq. (3) and Eq. (14) we obtain

$$\frac{\partial E}{\partial z} = \frac{1}{2} [(1 - i\alpha)\Gamma(\hat{g}_0 + \Delta N \hat{g}_N) - \alpha_{\text{int}}] E + i\hat{\beta}E + r, \quad (22)$$

and

$$\begin{aligned} \frac{\partial \Delta N}{\partial t} = & -\frac{\Delta N}{\tau(N_0)} - \left[R(N_0) - \frac{J}{ed} \right] \\ & - \frac{\text{Re} [E^* (1 - i\alpha)\Gamma \hat{g}_0 E]}{\hbar\omega_0 S} \\ & - \Delta N \frac{\text{Re} [E^* (1 - i\alpha)\Gamma \hat{g}_N E]}{\hbar\omega_0 S}, \end{aligned} \quad (23)$$

where the operators \hat{g}_0 and \hat{g}_N are defined as in Eq. (4), provided that $g(N, \omega)$ is replaced with $g(N_0, \omega)$ and $g_N(N_0, \omega)$, respectively.

The evolution equation for the electric field coefficient E_k is obtained by inserting the expression of the field (15) in Eq. (22) and by equating the coefficient of the term $\exp(-ik\Omega t)$ at the two sides of the resulting equation. As a result, one finds

$$\begin{aligned} \frac{dE_k}{dz} = & \left[\frac{1}{2}(1 - i\alpha)\Gamma g(N_0, \omega_k) - \alpha_{\text{int}} + i\beta(\omega_k) \right] E_k \\ & + \frac{1}{2}(1 - i\alpha) \sum_n \Delta N_{k-n} \Gamma g_N(N_0, \omega_n) E_n + r_k, \end{aligned} \quad (24)$$

where we used $\hat{g}_0 E = \sum_k g(N_0, \omega_k) E_k \exp(-ik\Omega t)$ and $\hat{g}_N E = \sum_k g_N(N_0, \omega_k) E_k \exp(-ik\Omega t)$, with $\omega_k = \omega_0 + k\Omega$. The noise term r_k is defined by

$$r_k(N; z) = \int dt e^{ik\Omega t} r_{\text{sp}}(N, t; z), \quad (25)$$

has zero mean $\langle r_k(N; z) \rangle = 0$, and its variance follows from

$$\begin{aligned} \langle r_k^*(N; z) r_h(N; z') \rangle = & \delta(z - z') \hbar\omega_0 \\ & \times \int dt \int dt' \exp[i\Omega(kt' - ht)] R_{\text{sp}}(N, t' - t). \end{aligned} \quad (26)$$

Using the stationarity of R_{sp} , we may express the above as

$$\begin{aligned} \langle r_k^*(N; z) r_h(N; z') \rangle = & \delta_{k,h} \delta(z - z') \hbar\omega_0 \\ & \times n_{\text{sp}}(N, \omega_0 + k\Omega) \Gamma g(N, \omega_0 + k\Omega). \end{aligned} \quad (27)$$

The terms $r_k(N; z')$, $k = 0, \pm 1, \pm 2, \dots$ are therefore a set of phase-independent, spatially-uncorrelated noise terms, which can be modeled as differentials of independent Wiener processes. At this point we can recast Eq. (24) in the following compact form

$$\frac{d\vec{E}}{dz} = \left[\frac{1}{2}(1 - i\alpha)\Gamma(\mathbf{G} + \mathbf{H}) - \alpha_{\text{int}}\mathbf{I} + i\mathbf{b} \right] \vec{E} + \vec{r}, \quad (28)$$

where \vec{E} and \vec{r} are column vectors constructed by stacking the electric field coefficients E_k and the noise projections r_k one on

top of another, respectively, with E_0 and r_0 occupying the central position, namely $\vec{E} = [\dots, E_2, E_1, E_0, E_{-1}, E_{-2}, \dots]^t$, and the same for \vec{r} (the superscript t stands for “transposed”). The vector \vec{E} and \vec{r} are of course infinite-dimensional, and so are the square matrices \mathbf{G} , \mathbf{H} and \mathbf{b} . Consistently with the definition of \vec{E} , we use positive and negative indices to identify the elements of these matrices, with the $(0, 0)$ element occupying the central position. In particular, \mathbf{G} and \mathbf{b} are diagonal matrices whose (k, k) elements are equal to $G_{k,k} = g(N_0, \omega_k)$ and $b_{k,k} = \beta(\omega_k) - \beta(\omega_0) - k\Omega d\beta(\omega_0)/d\omega_0$, respectively, whereas the (k, n) element of \mathbf{H} is $H_{k,n} = \Delta N_{k-n} g_N(N_0, \omega_n)$. By \mathbf{I} we denote the identity matrix (regardless of its dimensions).

We now proceed to the extraction of the carrier density coefficients ΔN_k by equating the terms proportional to $\exp(-ik\Omega t)$ at the two sides of Eq. (23), when the expression of ΔN in Eq. (16) is inserted in it. After some straightforward algebra, involving the use of Eq. (17), one obtains

$$(1 - ik\tau\Omega) \Delta N_k = - \sum_h \Delta N_h p_{k,h} + \mathcal{N}_k, \quad (29)$$

where

$$\begin{aligned} \mathcal{N}_k &= -\tau(N_0)R(N_0)(1 - \delta_{k,0}) \\ &\times \sum_n \left[\frac{(1 - i\alpha)E_{n+k}E_n^*}{P_{\text{stim}}(N_0, \omega_{n+k})} + \frac{(1 + i\alpha)E_{n+k}E_n^*}{P_{\text{stim}}(N_0, \omega_n)} \right], \quad (30) \\ p_{k,h} &= \sum_n \left[\frac{(1 - i\alpha)E_{n+k-h}E_n^*}{P_{\text{sat}}(N_0, \omega_{n+k-h})} + \frac{(1 + i\alpha)E_{n+k-h}E_n^*}{P_{\text{sat}}(N_0, \omega_n)} \right]. \quad (31) \end{aligned}$$

The quantity

$$P_{\text{sat}}(N_0, \omega) = \frac{\hbar\omega_0 S}{\tau(N_0)\Gamma g_N(N_0, \omega)} \quad (32)$$

is the familiar saturation power, although its definition accounts for the frequency dependence of the gain coefficient explicitly, and

$$P_{\text{stim}}(N_0, \omega) = R(N_0) \frac{\hbar\omega_0 S}{\Gamma g(N_0, \omega)} \quad (33)$$

is the power value above which carrier depletion is dominated by stimulated emission. We hence refer to P_{stim} as to *stimulated* power. Equation (29) can be conveniently recast in the following compact form

$$(\mathbf{I} - i\tau\Omega\mathbf{k} + \mathbf{p})\Delta\vec{N} = \vec{\mathcal{N}}, \quad (34)$$

where the (k, h) element of the matrix \mathbf{p} is equal to $p_{k,h}$, and \mathbf{k} is a diagonal matrix with diagonal elements $\kappa_{k,k} = k$. The column vectors $\Delta\vec{N}$ and $\vec{\mathcal{N}}$ are constructed (like the field vector \vec{E}) by stacking the coefficients ΔN_k and \mathcal{N}_k one on top of another, respectively, namely, $\Delta\vec{N} = [\dots, \Delta N_1, \Delta N_0, \Delta N_{-1}, \dots]^t$ and $\vec{\mathcal{N}} = [\dots, \mathcal{N}_1, 0, \mathcal{N}_{-1}, \dots]^t$. The coefficients N_0 and ΔN_k are hence obtained for a given electric field state by solving Eqs. (17) and (34). These are the most general coupled-mode equations accounting for any functional dependence of the recombination

rate and material optical gain on carrier density, as well as for the frequency dependence of the gain and waveguide dispersion.

III. IMPLEMENTATION OF THE COUPLED-MODE EQUATION MODEL IN REALISTIC SOA STRUCTURES

As is customarily done in most studies of practical relevance, where the waveguide dispersion and the frequency dependence of the gain coefficient have been shown to play a minor role, in this section we neglect chromatic dispersion, as well as higher-order dispersion, and assume frequency-independent gain. With this simplification the matrices \mathbf{G} , \mathbf{H} , and \mathbf{p} become frequency-independent and assume a very convenient form, as is shown in what follows. We also neglect the presence of spontaneous emission noise terms, whose implications on the SOA performance, chiefly on the SOA noise figure, will be the subject of future work.

The multi-wavelength propagation model introduced in the previous section involves an infinite number of coefficients E_k and ΔN_k , a situation that is obviously incompatible with its implementation in any numerical platform. However, as will be shown in the next section, high-order coefficients (namely E_k and ΔN_k coefficients with large values of $|k|$) provide a negligible contribution to the solution of Eqs. (17), (28), and (34), and hence they can be omitted by truncating the vectors \vec{E} and $\Delta\vec{N}$. The truncation of \vec{E} and $\Delta\vec{N}$ requires of course that all matrices involved in Eqs. (28) and (34) be also truncated accordingly. In what follows we provide explicit expressions for those matrices and discuss the procedure that allows the efficient computation of \vec{E} and $\Delta\vec{N}$.

The truncation procedure of the infinite set of equations (28) can be performed in a number of ways. One possible approach is assuming that $E_k(z) = 0$ for $|k| > M$. Here M is an integer number that can be determined self consistently by checking that the integration of the equations for $M \rightarrow M + 1$ yields indistinguishable results. This assumption implies $\Delta N_k(z) = 0$ for $|k| > 2M$, owing to the absence of beat terms at frequency offsets larger than $2M\Omega$. A simpler yet equally accurate approach is to assume that the carrier density coefficients $\Delta N_k(z)$ are also zero at frequency offsets greater than $M\Omega$. Here we adopt the latter approach, within which Eqs. (15) and (16) specialize to

$$E(z, t) = \sum_{k=-M}^M E_k(z) e^{-ik\Omega t}, \quad (35)$$

$$N(z, t) = N_0(z) + \sum_{k=-M}^M \Delta N_k(z) e^{-ik\Omega t}. \quad (36)$$

Accordingly, the field vector \vec{E} and carrier density modulation vector $\Delta\vec{N}$, consist of $(2M + 1)$ components. Matrices \mathbf{G} and \mathbf{H} in Eq. (28) become $(2M + 1) \times (2M + 1)$ matrices. In particular, owing to the assumption of frequency-flat gain, one can readily verify the equalities $\mathbf{G} = g(N_0)\mathbf{I}$, and $\mathbf{H} = g_N(N_0)\mathbf{T}(\Delta\vec{N})$, where by $\mathbf{T}_{2M+1}(\Delta N_k)$ we denote a Hermitian-symmetric Toeplitz matrix [18]. Below we give the expression of $\mathbf{T}_{2M+1}(\Delta N_k)$ in the case $M = 2$ for illustration

purposes,

$$\mathbf{T}_5(\Delta N_k) = \begin{bmatrix} \Delta N_0 & \Delta N_1 & \Delta N_2 & 0 & 0 \\ \Delta N_1^* & \Delta N_0 & \Delta N_1 & \Delta N_2 & 0 \\ \Delta N_2^* & \Delta N_1^* & \Delta N_0 & \Delta N_1 & \Delta N_2 \\ 0 & \Delta N_2^* & \Delta N_1^* & \Delta N_0 & \Delta N_1 \\ 0 & 0 & \Delta N_2^* & \Delta N_1^* & \Delta N_0 \end{bmatrix}. \quad (37)$$

The neglect of the waveguide dispersion yields $\mathbf{b} = 0$, and hence Eq. (28) simplifies to

$$\frac{d\vec{E}}{dz} = \left[\frac{(1 - i\alpha)g(N_0) - \alpha_{\text{int}}}{2} \mathbf{I} + \mathbf{T}_{2M+1}(\Delta N_k) \right] \vec{E}, \quad (38)$$

where N_0 is the solution of

$$\frac{J}{ed} = R(N_0) \left[1 + \frac{|\vec{E}|^2}{\tau P_{\text{stim}}(N_0)} \right], \quad (39)$$

with

$$P_{\text{stim}}(N_0) = R(N_0) \frac{\hbar\omega_0 S}{\Gamma g(N_0)}. \quad (40)$$

The expression for the carrier density modulation vector $\Delta\vec{N}$ simplifies to

$$\Delta\vec{N} = -\frac{\tau R(N_0)}{P_{\text{stim}}(N_0)} \left[\mathbf{I} - \tau\Omega\mathbf{k} + \frac{\mathbf{T}_{2M+1}(C_k)}{P_{\text{sat}}(N_0)} \right]^{-1} \vec{C}, \quad (41)$$

where

$$P_{\text{sat}}(N_0) = \frac{\hbar\omega_0 S}{\tau(N_0)\Gamma g_N(N_0)}, \quad (42)$$

and where C_k is the discrete autocorrelation function of \vec{E} , namely

$$C_k = \sum_{n=-M}^M E_{n+k} E_n^*, \quad (43)$$

in which we assume $E_n = 0$ for $|n| > M$. The expression of \vec{C} in the case $M = 2$ is

$$\vec{C} = [C_2, C_1, C_0, C_1^*, C_2^*]^t, \quad (44)$$

and that of $\mathbf{T}_5(C_k)$ is

$$\mathbf{T}_5(C_k) = \begin{bmatrix} C_0 & C_1 & C_2 & C_3 & C_4 \\ C_1^* & C_0 & C_1 & C_2 & C_3 \\ C_2^* & C_1^* & C_0 & C_1 & C_2 \\ C_3^* & C_2^* & C_1^* & C_0 & C_1 \\ C_4^* & C_3^* & C_2^* & C_1^* & C_0 \end{bmatrix}, \quad (45)$$

where we used $C_{-k} = C_k^*$, as can be readily verified by inspecting Eq. (43).

The numerical integration of the coupled-equations involves a three-step procedure for the transition from z to $z + \Delta z$, given the field vector $\vec{E}(z)$. These are:

- 1) Find the value of $N_0(z)$ by solving Eq. (39);
- 2) Extract the carrier density vector $\Delta\vec{N}(z)$ as in Eq. (41);

TABLE I
SOA PARAMETERS

Description	Value	Units
Linear recombination coefficient A	10^6	s^{-1}
Bimolecular recombination coefficient B	0.3×10^{-10}	cm^3/s
Auger coefficient C	3.3×10^{-29}	cm^6/s
Optical confinement factor Γ	9.7%	
Linewidth enhancement factor α	5	
Optical wavelength λ_0	1561	nm
Group velocity v_g	8.33×10^9	cm/s
Active region width w_a	2×10^{-4}	cm
Active region tickness d	65×10^{-7}	cm
Active region length L	0.1	cm
Gain coefficient g_0	1800	cm^{-1}
Transparency carrier density N_{tr}	2×10^{18}	cm^{-3}
SOA internal loss α_{int}	5	cm^{-1}
Injection current density J	3.4×10^3	A/cm ²
Frequency spacing $\Omega/2\pi$	8.6	GHz

- 3) Evaluate the field vector $\vec{E}(z + \Delta z)$ by solving Eq. (38) from z to $z + \Delta z$ while using the values of N_0 and ΔN_k obtained in steps 1 and 2, according to

$$\vec{E}(z + \Delta z) = \exp \left\{ \frac{(1 - i\alpha)g[N_0(z)] - \alpha_{\text{int}}}{2} \Delta z \right\} \exp \{ \mathbf{T}_{2M+1}[\Delta N_k(z)] \Delta z \} \vec{E}(z). \quad (46)$$

A. Model Validation

In this section we test the accuracy of the proposed multi-wavelength propagation model against the results obtained by integrating the full model' space-time equations (3) and (14). To this end we consider a QW SOA, characterized by the following logarithmic functional dependence of the gain coefficient on carrier density [6]

$$g(N) = g_0 \log \left(\frac{N}{N_{\text{tr}}} \right), \quad (47)$$

where g_0 is a gain parameter and N_{tr} is the carrier density required for transparency.⁴ The expansion of the gain function is in this case $g(N) \simeq g(N_0) + g_N(N_0)\Delta N$, with

$$g(N_0) = g_0 \log \left(\frac{N_0}{N_{\text{tr}}} \right), \quad g_N(N_0) = \frac{g_0}{N_0}. \quad (48)$$

The physical and operational parameters of the SOA are listed in Table I (we note that the SOA is operated with the injection current density $J = 8.5J_{\text{tr}}$, where $J_{\text{tr}} = ed(AN_{\text{tr}} + BN_{\text{tr}}^2 + CN_{\text{tr}}^3)$ is the injection current density required for transparency). The SOA is injected with a three-wavelength optical signal characterized by the complex envelope

$$E_{\text{in}}(t) = \sqrt{W_1} e^{-i\Omega t} + \sqrt{W_0} + \sqrt{W_{-1}} e^{i\Omega t} \quad (49)$$

with $W_1 = W_{-1} = -2$ dBm, and $W_0 = -7$ dBm. For this set of parameters we solved the coupled-mode equations (38), (40), and (41) with the input field vector $\vec{E}_{\text{in}} = [\dots, 0, \sqrt{W_1}, \sqrt{W_0}]$,

⁴Of course, the use of different functional forms of $g(N)$, for instance the more accurate three parameter expression $g(N) = g_0 \ln[(N + N_s)/(N_{\text{tr}} + N_s)]$ also reported in [6], is fully equivalent in terms of model complexity.

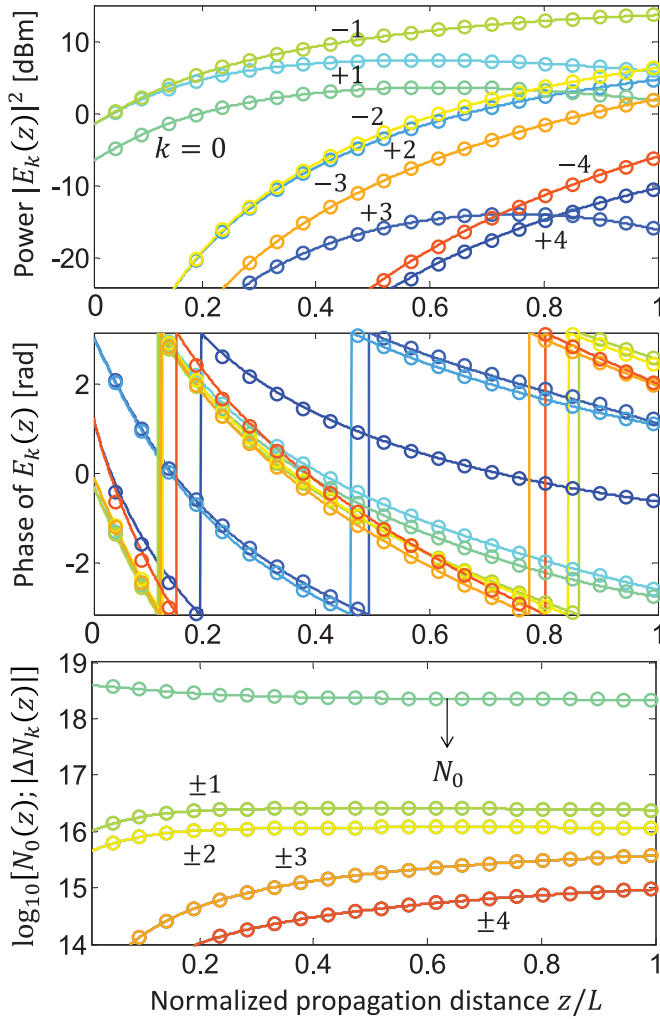


Fig. 1. Intensity (top panel) and phase (bottom panel) of the field components E_k versus normalized propagation distance z/L for the displayed values of k and for the SOA parameters' values in Table I. Solid curves refer to the coupled-mode model, while circles were obtained by solving the space-time equations of the full model.

$\sqrt{W_{-1}}, 0, \dots]^t$. We used $M = 6$ and checked that larger values of M yield indistinguishable results. We then integrated the full model's equations (3) and (14) with the procedure described in [19], and extracted the coefficients $E_k(z)$ from the numerical solution $E_{\text{num}}(z, t)$ according to

$$E_k(z) \leftrightarrow \frac{\Omega}{2\pi} \int_{t_0}^{2\pi/\Omega} E_{\text{num}}(z, t) e^{ik\Omega t} dt, \quad (50)$$

where by t_0 we denote any time at which the system achieved its stationary state. The results are shown in Fig. 1. In the top panel we plot by solid curves the intensities of the coefficients $E_k(z)$ versus the normalized propagation distance z/L for values of k ranging between $k = -4$ and $k = 4$. By circles we plot the results obtained with the full model. The excellent accuracy of the coupled-mode model is self-evident. Interestingly, the figure shows that the coupled-mode model is accurate in describing the formation of FWM components that eventually (at the SOA output) exceed some of the input components. The center panel of the same figure shows the corresponding phases

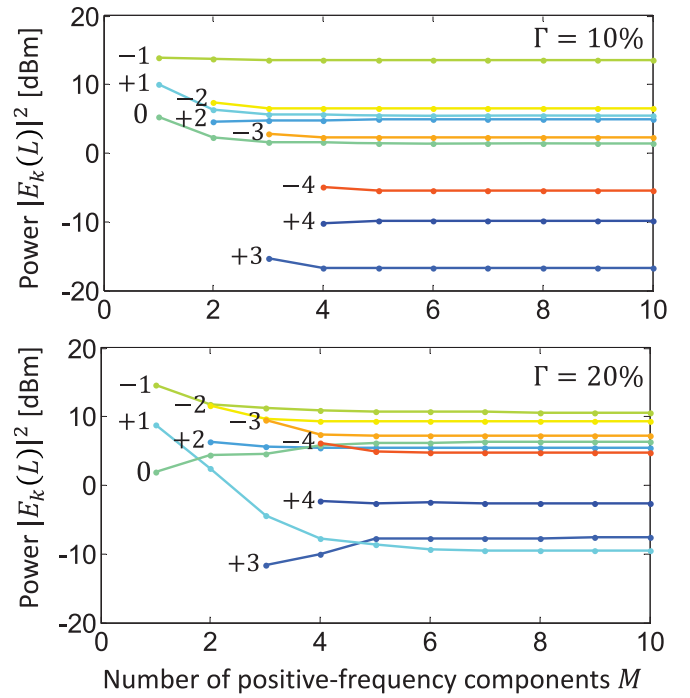


Fig. 2. Intensities of field components E_k at the SOA output $|E_k(L)|^2$, as obtained by using the coupled-mode model, for increasing values of M . Each curve corresponds to a specific value of k and hence it originates at $|k| = M$. The top panel refers to the set of parameters listed in Table I and used in Fig. 1, whereas in the bottom panel the optical confinement factor was increased from 10% to 20%.

of the field coefficients E_k (more precisely the solid curves are the plot of $\text{Phase}[E_k(z)] + k\Omega z/v_g$, where the second term accounts for the fact that the coefficients $E_k(z)$ characterize the field envelope in the time reference delayed by z/v_g). The lower panel provides a direct validation of the condition $|\Delta N_k| \ll N_0$, which was assumed in the perturbation analysis. The top circles show the time-averaged carrier density (in a logarithmic scale) extracted from the full model results. Although this quantity is described in the coupled-mode model by $N_0 + \Delta N_0$, we compare it with N_0 , which is shown as a solid curve. The excellent agreement between the two plotted quantities is a proof of the condition $\Delta N_0 \ll N_0$. Lower curves and markers are plots of $|\Delta N_k|$ for values of $|k|$ ranging between 1 and 4 (we recall that $|\Delta N_k| = |\Delta N_{-k}|$). The plot shows that the absolute value of the coefficients ΔN_k is more than two orders of magnitude smaller than N_0 , thus confirming the condition $|\Delta N_k| \ll N_0$, also for $|k| > 0$. Moreover, the excellent agreement between the full model and the coupled-mode model validates the perturbation approach for arbitrary magnitude of the perturbations.

We stress that the coupled-mode model offers considerably greater computational efficiency, as compared to the full time domain model. In the specific example of Fig. 1, the integration time of the coupled-mode equations was more than two orders of magnitude smaller than the integration time required by the space-time equations, using in both cases in-house developed MATLAB routines run on the same workstation.

In Fig. 2 we illustrate the dependence of the coupled-mode model's results on the number of field coefficients that are

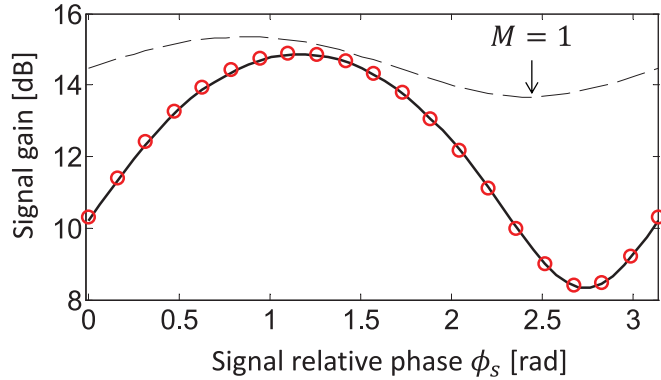


Fig. 3. Dual-pumped SOA-based PSA's gain versus the relative phase of the input signal ϕ_s introduced in Eq. (55). The SOA parameters used in the numerical computation are those given in Table I, the input pump powers were set to $W_{P_1} = W_{P_2} = -2$ dBm, and the input signal power to $W_s = -22$ dBm. The solid curve refers to the coupled-mode model with $M = 4$ (larger values of M yield indistinguishable results), while the circles were obtained by integrating the space-time equations of the full model. The dashed curve shows the results obtained with the coupled-mode model by propagating only the pump and signal components, namely by setting $M = 1$.

considered. In the top panel we plot the output intensities $|E_k(L)|^2$ evaluated by solving the coupled-mode equations for increasing values of M , with each curve corresponding to a different value of k . Since the accounting for the frequency component E_k dictates that $M \geq |k|$, the curve referring to E_k originates at $M = |k|$. The plot shows that in the numerical example considered here the results of the coupled-mode equations for the component E_k become accurate (that is, the corresponding curve in the figure becomes flat) for M exceeding $|k|$ by a one or two units. However, it should be pointed out that the convergence to the correct result is affected by the specific SOA parameters' value and may be slower. This is shown in the lower panel of the Fig. 2, where the same curves plotted in the top panel are re-calculated by increasing the SOA optical confinement factor from 10% to 20% and by leaving the other SOA parameters unchanged. In this example, it can be seen that using $M < 6$ may yield an error in the calculation of $|E_1(L)|^2$ up to a factor of 100.

The SOA length assumed in this section for the validation of the coupled-mode model is intermediate between the typical length of “ultra-short” SOAs ($L < 0.5$ mm) and that of “ultra-long” SOAs ($L > 1$ mm). We note that while the accuracy of the coupled-mode model is not affected in the case of shorter SOAs, the model may require some improvement in the case of ultra-long SOAs, where one needs to take into account the spatial dependence of the injection current, as well as its dependence on the local carrier density [20].

IV. APPLICATION OF THE MODEL: DUAL-PUMPED SOA-BASED PSA

In this section we apply the coupled-mode model to the study of the dual-pumped SOA-based PSA presented in [11]–[13]. The goal of this exercise is two-folded. On the one hand we aim to show that the phase-sensitive gain value obtained with the coupled-mode model assuming realistic SOA parameters is

consistent with the experimentally obtained value. On the other hand, we show explicitly that by restricting the coupled-mode model to the pump and signal components only, as is sometimes done [21], yields significantly incorrect results when a realistic dependence of the amplifier gain on carrier density is used.

The waveform at the input of a PSA of the kind considered here can be expressed as

$$E_{\text{in}}(t) = e^{i\phi_1} \sqrt{W_1} e^{-i\Omega t} + e^{i\phi_0} \sqrt{W_0} + e^{i\phi_{-1}} \sqrt{W_{-1}} e^{i\Omega t}, \quad (51)$$

where by W_1 and W_{-1} we denote the optical powers of the two pumps and by ϕ_1 and ϕ_{-1} their absolute phases. The field component at the central frequency represents the input signal component. By removing in all components the immaterial average phase of the two pumps

$$\phi_c = (\phi_1 + \phi_{-1})/2, \quad (52)$$

and denoting by

$$\phi_s = \phi_0 - \phi_c \quad (53)$$

the input signal phase relative to ϕ_c , the input field envelope can be expressed as

$$E_{\text{in}}(t) = e^{i\phi_p} \sqrt{W_1} e^{-i\Omega t} + e^{i\phi_s} \sqrt{W_0} + e^{-i\phi_p} \sqrt{W_{-1}} e^{i\Omega t}, \quad (54)$$

where $\phi_p = (\phi_1 - \phi_{-1})/2$. We further note that the effect of ϕ_p is limited to introducing an immaterial time shift $t_p = \phi_p/\Omega$, and hence it can be safely set to $\phi_p = 0$. We therefore solve the space-time equations using the following input waveform,

$$E_{\text{in}}(t) = \sqrt{W_{P_1}} e^{-i\Omega t} + e^{i\phi_s} \sqrt{W_s} + \sqrt{W_{P_2}} e^{i\Omega t}, \quad (55)$$

and the coupled-mode equations with the input field vector

$$\vec{E}_{\text{in}} = [\dots, 0, \sqrt{W_{P_1}}, e^{i\phi_s} \sqrt{W_s}, \sqrt{W_{P_2}}, 0, \dots]^t. \quad (56)$$

The key quantity that characterizes the performance of the PSA under scrutiny is the dependence of the signal gain on the phase ϕ_s . In Fig. 3 we plot the gain $G_s(\phi_s) = |E_s(L)|^2/W_s$ (in decibels) as a function of ϕ_s , where in the case of the full model the term $E_s(L)$ is extracted from the numerical solution $E_{\text{num}}(L, t)$ according to Eq. (50) with $z = L$. The SOA parameters used in the numerical example are those given in Table I. The input pump powers were set to $W_{P_1} = W_{P_2} = -2$ dBm, and the input signal power to the much smaller value $W_s = -22$ dBm. The solid curve is obtained by integrating the coupled-mode model with $M = 4$, whereas the circles refer to the space-time model. The excellent agreement between the coupled-mode model and the space-time model, like in the previous section, is self-evident. The thin dashed curve in Fig. 3 shows the result obtained with the coupled-mode model by including only the pump and signal field components, that is by using $M = 1$. The plot shows that the neglect of high-order FWM products yields higher gain values and a lower phase dependent gain.

We now proceed to compare the results of the coupled-mode model with the experimental data reported in ref. [13], wherein all the details concerning the experiment can be found.

The comparison between the theory and the data is performed by looking at the dependence of the PSA gain on the input signal relative phase ϕ_s of the kind shown in Fig. 3. To this end, we

note that the numerical values of the SOA parameters listed in Table I are those estimated for one of the devices tested in [13], and specifically for the device with a phase dependent gain of about 6.3 dB. Some of the parameters were directly taken from the device geometry, like the active region length and width. The active region thickness was taken to be 65 nm to reflect the fact that the active region of the device consisted of 10 InP/InGaAsP QWs of 6.5 nm width each. Some of the parameters were estimated by independent analysis, like for instance the value of $\Gamma \simeq 10\%$, which was extracted from the mode profile given by a finite-difference-method-based electromagnetic solver. The value of the transparency current density used in simulations is $J_{th} = 0.43 \text{ kA/cm}^2$, versus the measured value of about 1 kA/cm^2 . This implies an injection efficiency of about 43%, which includes the loss caused by lateral current spreading in the waveguide region and the carrier trapping efficiency in the QWs. The values for the gain coefficient g_0 and for the coefficients A , B and C are those typical for the InP/InGaAsP MQW active region of the SOA used in the experiment [6], [13]. The waveguide internal loss was also set to the typical value of $\alpha_{int} = 5 \text{ cm}^{-1}$ measured in good quality devices. The linewidth enhancement factor $\alpha = 5$ is also within the typical range of values for devices of this type. With these parameters, the model predicts about 59 dB of linear gain, whereas the measured linear gain of the device under test was about 48.5 dB [13]. The 10 dB difference can, however, be safely attributed to gain compression induced by ASE—neglected in the model but significant for zero input in devices with high linear gain—and to thermal effects within the waveguide.

The comparison between the theoretical curve shown in Fig. 3 and the data requires some care. More specifically, since the way in which the experiment is performed does not allow a precise measurement of the input signal power, in this comparison we look at the output signal power (rather than at the gain). In the logarithmic scale, this simply requires adding a bias to the theoretical PSA gain. The relative signal phase ϕ_s defined in Eq. (53) is also not known directly. Indeed in the experiment, the phase of the input signal is controlled by passing the signal through a tuning region prior to the injection into the SOA. The phase change of the signal is proportional to the square root of the current I_ϕ injected in the tuning region. A calibration procedure allowed to establish, for I_ϕ between 1 and 2 mA, the relation $\phi_0 - \phi_1 = \pi\chi\sqrt{I_\phi}$ with $\chi \simeq 1 \text{ mA}^{-1/2}$. As a result, the relation between the signal relative phase ϕ_s and the measured control current I_ϕ , $\phi_s = \pi\chi\sqrt{I_\phi} + \phi_b$, obtained using the definition of ϕ_s in Eq. (53), contains the unknown bias $\phi_b = (\phi_1 - \phi_{-1})/2$, which also needs to be added to the theoretical signal phase in order to facilitate the comparison between the theory and the data.

In Fig. 4 we plot the output signal power versus the square-root injection current $\sqrt{I_\phi}$. The markers refer to the experimental results, and they were taken from [13, Fig. 26(a)]. The solid curve is obtained from the curve plotted in Fig. 3 by shifting the vertical and the horizontal axes, so as to fit the data, as discussed in the previous paragraph. The agreement between theory and experiment is self evident. We remark that such good agreement cannot be obtained by using the conventional three-wave

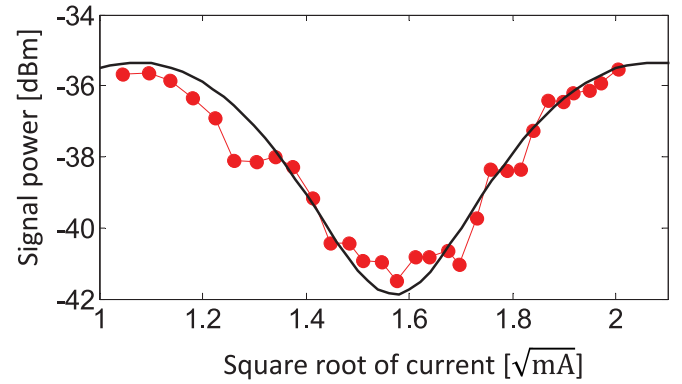


Fig. 4. Measured relationship among the signal power, the signal phase and the square root of the current applied to the phase tuner (see ref. [13]), together with the curve of Fig. 3, suitably re-centered to fit the data.

model (corresponding to the case $M = 1$ in our theory and used in ref. [21]) where the high-order harmonics generated by the nonlinear interaction between the signal and the two pump are neglected, unless unrealistic values for the device parameters are assumed.

V. CONCLUSION

To conclude, we derived a couple-mode model for multi-wave mixing in SOAs characterized by arbitrary functional dependencies of the recombination rate and material gain on carrier density. The model takes into account the frequency dependence of the material gain, as well as all orders of the waveguide dispersion, and accommodates input fields consisting of arbitrary combinations of multiple frequency components. We showed that the conventional approach assuming a limited number of generated FWM components gives inaccurate results when two waveforms of similar intensities are injected into the SOA. In this case, our model gives highly accurate results if a sufficient number of generated components are taken into account, as we showed by direct comparison with full time-domain simulations. We applied the coupled-mode model to studying the operation of a recently demonstrated dual-pumped PSA based on an integrated QW SOA [11]–[13], and showed that the outcome of the model is consistent with the experimental results.

REFERENCES

- [1] M. J. Connelly, "Wide-band steady-state numerical model and parameter extraction of a tensile-strained Bulk semiconductor optical amplifier," *IEEE J. Quantum Electron.*, vol. 43, no. 1, pp. 47–56, Jan. 2007.
- [2] A. R. Totović, J. V. Crnjanski, M. M. Krstić, and D. M. Gvozdić, "Numerical study of the small-signal modulation bandwidth of reflective and traveling-wave SOAs," *J. Lightw. Technol.*, vol. 33, no. 13, pp. 2758–2764, Jul. 1, 2015.
- [3] G. P. Agrawal, "Population pulsations and nondegenerate four-wave mixing in semiconductor lasers and amplifiers," *J. Opt. Soc. Amer. B*, vol. 5, pp. 147–159, Jan. 1988.
- [4] A. Mecozzi, "Analytical theory of four-wave mixing in semiconductor amplifiers," *Opt. Lett.*, vol. 19, pp. 892–894, Jun. 15, 1994.
- [5] A. Mecozzi and J. Mørk, "Saturation induced by picosecond pulses in semiconductor optical amplifiers," *J. Opt. Soc. Amer. B*, vol. 14, pp. 761–770, Apr. 1997.
- [6] L. A. Coldren, S. W. Corzine, and M. L. Mašanović, *Diode Lasers and Photonic Integrated Circuits* (ser. Microwave and Optical Engineering), 2nd ed. Hoboken, NJ, USA: Wiley, 2012, ch. 2, 4.

- [7] P. P. Baveja, D. N. Maywar, and G. P. Agrawal, "Interband four-wave mixing in semiconductor optical amplifiers with ASE-enhanced gain recovery," *IEEE J. Sel. Topics Quantum Electron.*, vol. 18, no. 2, pp. 899–908, Mar./Apr. 2012.
- [8] M. A. Summerfield and R. S. Tucker, "Frequency-domain model of multiwave mixing in bulk semiconductor optical amplifiers," *IEEE J. Sel. Topics Quantum Electron.*, vol. 5, no. 3, pp. 839–850, May/June 1999.
- [9] P. Frascella, S. Sygletos, F. C. Garcia Gunning, R. Weerasuriya, L. Grüner-Nielsen, R. Phelan, J. O’Gorman, and A. D. Ellis, "DPSK signal regeneration with a dual-pump nondegenerate phase-sensitive amplifier," *IEEE Photon. Technol. Lett.*, vol. 23, no. 8, pp. 516–518, Apr. 2011.
- [10] A. D. Ellis and S. Sygletos, "Phase sensitive signal processing using semiconductor optical amplifiers," presented at the Optical Fiber Communication Conf./Nat. Fiber Optic Engineers Conf., Anaheim, CA, USA, 2013, paper OW4C.1.
- [11] W. Li, M. Lu, L. Johansson, M. L. Mašanović, D. Dadić, S. Arafın, and L. Coldren, "First demonstration of an integrated photonic phase-sensitive amplifier," presented at the Conf. Lasers Electro Optics, San Jose, CA, USA, paper SW4N.5.
- [12] L. A. Coldren, W. Li, A. Mecozzi, M. Lu, S. Arafın, M. Vasilyev, D. Dadić, and L. A. Johansson, "Single-chip dual-pumped SOA-based phase-sensitive amplifier at 1550 nm," presented at the Summer Topicals Meeting Series, Jul. 13–15, 2015, pp. 88–89.
- [13] W. Li, M. Lu, A. Mecozzi, M. Vasilyev, S. Arafın, D. Dadić, L. A. Johansson, L. A. Coldren, "First monolithically integrated dual-pumped phase-sensitive amplifier chip based on a saturated semiconductor optical amplifier," *IEEE J. Quantum Electron.*, vol. 52, no. 1, pp. 1–12, Jan. 2016.
- [14] A. Mecozzi and J. Mørk, "Saturation effects in nondegenerate four-wave mixing between short optical pulses in semiconductor laser amplifiers," *IEEE J. Sel. Topics Quantum Electron.*, vol. 3, no. 5, pp. 1190–1207, Oct. 1997.
- [15] R. Paiella, G. Hunziker, and K. J. Vahala, "Quantum-well capture and inter-well transport in semiconductor active layers," *Semicond. Sci. Technol.*, vol. 14, pp. R17–R25, 1999.
- [16] C. W. Gardiner, *Handbook of Stochastic Methods* (ser. Synergetics), vol. 13, 2nd ed. Berlin, Germany: Springer-Verlag, 1985.
- [17] L. A. Coldren, S. W. Corzine, and M. L. Mašanović, *Diode Lasers and Photonic Integrated Circuits* (ser. Microwave and Optical Engineering), 2nd ed. Hoboken, NJ, USA: Wiley, 2012, ch. 5, p. 257.
- [18] A. Böttcher and S. M. Grudsky, *Toeplitz Matrices, Asymptotic Linear Algebra, and Functional Analysis*. Basel, Switzerland: Birkhäuser, 2012.
- [19] J. W. D. Chi, L. Chao, and M. K. Rao, "Time-domain large-signal investigation on nonlinear interactions between an optical pulse and semiconductor waveguides," *IEEE J. Quantum Electron.*, vol. 37, no. 10, pp. 1329–1336, Oct. 2001.
- [20] P. Morel and A. Sharaiha, "Wideband time-domain transfer matrix model equivalent circuit for short pulse propagation in semiconductor optical amplifiers," *IEEE J. Quantum Electron.*, vol. 45, no. 2, pp. 103–116, Feb. 2009.
- [21] W. Yang, T. Cao, Y. Yu, L. Shi, X. Zhang, and D. Huang, "Theoretical analysis and experimental investigation of degenerate phase sensitive amplification in a semiconductor optical amplifier," *J. Lightw. Technol.*, vol. 33, no. 19, pp. 4001–4007, Oct. 1, 2015.

Cristian Antonelli received the M.Sc. and Ph.D. degrees in electrical engineering from the University of L’Aquila, L’Aquila, Italy, in 2002 and 2006, respectively. During his graduate studies, he worked on the "Hinge Model" for the time dynamics of PMD in lightwave systems within a collaboration with AT&T Labs, Middletown, NJ, USA, where he was a Visiting Scientist in the summers of 2004 and 2005. In 2006, he spent six months with the Research Laboratory of Electronics, Massachusetts Institute of Technology, Cambridge, MA, USA, performing research on the theory of mode-locked fiber lasers. Since 2007, he has been a Senior Research Scientist first at CNISM, the Italian Interuniversity Consortium for the physics of matter, and then at the University of L’Aquila. In April 2014, he joined the Department of Physical and Chemical Sciences of the same university as an Assistant Professor. His research interests include the modeling and characterization of fiber-optic communication systems, including PMD and PDL, fundamental energy consumption limits, semiconductor optical amplifier-based devices, and linear and nonlinear propagation effects in space-division multiplexed transmission. He is currently serving as a TCP Member for OFC 2016, as well as an Associate Editor for the JLT.

Antonio Mecozzi (M’98–SM’00–F’03) is a Professor and the Director of the Department of Physical and Chemical Sciences at the University of L’Aquila, L’Aquila, Italy. Previously, he worked for 15 years in the Optical Communication Division of Fondazione Ugo Bordoni, Rome. He was a Visiting Scientist of the EECS Department and the Research Laboratory of Electronics of MIT from 1991 to 1992. His areas of research interests include studies on soliton transmission, laser mode-locking, nonlinear propagation in single and multimode fibers, modal dispersion in multimode fibers, physics and applications of semiconductor optical amplifiers, and optical amplification and noise. He holds numerous patents and more than 160 publications in refereed scientific journals. He is currently serving as an Associate Editor for *Optics Express*. He is a Fellow of the Optical Society of America.

Wangzhe Li received the Ph.D. degree from the University of Ottawa, Ottawa, ON, Canada, in 2013 working on the photonic generation of microwave and millimeter wave signals, and then joined the University of California, Santa Barbara, CA, USA, as a Postdoctoral Scholar where he has been working on integrated optical phase-sensitive amplifiers.

Larry A. Coldren (S’67–M’72–SM’77–F’82–LF’12) received the Ph.D. degree in electrical engineering from Stanford University, Stanford, CA, USA, in 1972. After 13 years in the research area with Bell Laboratories, he joined the University of California (UCSB), Santa Barbara, CA, in 1984. He is the Fred Kavli Professor of optoelectronics and sensors and holds appointments with the Departments of Materials and Electrical and Computer Engineering. From 2009 to 2011, he was the Dean of the College of Engineering. In 1990, he cofounded Optical Concepts, later acquired as Gore Photonics, to develop novel VCSEL technology, and, in 1998, he cofounded Agility Communications, later acquired by JDSU, to develop widely tunable integrated transmitters. At UCSB, he worked on multiple-section widely tunable lasers and efficient vertical-cavity surface-emitting lasers (VCSELs). More recently, his group has developed high-performance InP-based photonic integrated circuits as well as high-speed VCSELs. He has authored or coauthored more than thousand journal and conference papers. He has also coauthored eight book chapters, a widely used textbook, and has been issued 65 patents. He received the 2004 John Tyndall, 2009 Aron Kressel, 2014 David Sarnoff, and 2015 IPRM Awards, and he is a Fellow of the OSA and IEE, and a Member of the National Academy of Engineering.

Investigation of an Integrated Photonic Dual-Pumped Phase-Sensitive Amplifier based on a Highly Saturated Semiconductor Optical Amplifier

Wangzhe Li¹, Antonio Mecozzi², Michael Vasilyev³, Mingzhi Lu¹, Leif Johansson¹, and Larry A. Coldren^{1*}

¹Department of Electrical and Computer Engineering, University of California, Santa Barbara, California 93117, USA

²Dept. of Physical and Chemical Sciences, University of L'Aquila via Vetoio 1, L'Aquila, Italy

³Dept. of Electrical Engineering, University of Texas at Arlington, Texas, USA

coldren@ece.ucsb.edu

Abstract: An integrated photonic phase-sensitive amplifier with a dual-pumped four-wave mixing architecture is investigated. Gain curves with multiple periods are theoretically studied and experimentally demonstrated with approximately 7.8 dB extinction gain.

OCIS codes: (190.4380) Nonlinear optics, four-wave mixing; (190.4410) Nonlinear optics, parametric processes; (250.5300) Photonic integrated circuits; (250.5980) Semiconductor optical amplifiers

1. Introduction

During the last few years, optical phase-sensitive amplifiers (PSAs) have been attracting great research attention [1] due to the unique advantage of enabling noiseless amplification. Unlike conventional phase-insensitive amplifiers (PIAs), such as erbium-doped fiber amplifiers (EDFAs) featuring 3-dB quantum-limited NF, PSAs' noise-free amplification could significantly improve the performance of optical links and provide a wide range of applications, such as optical telecommunication, remote sensing, and optical spectroscopy and imaging, where performance of the signal to noise ratio (SNR) is critical. Various PSAs using parametric down-conversion [2] or four-wave mixing (FWM) [3] have been demonstrated; however, in most demonstrated PSAs so far, their implementations are based on bulky bench-top systems, which make it difficult to use them in practical scenarios. In [4], we proposed and experimentally demonstrated the first integrated photonic PSA chip based on a highly saturated nonlinear semiconductor optical amplifier (SOA), exhibiting the potential that a chip-scale PSA could great benefit the implementation of PSAs for practical applications.

In this paper, we further investigate the performance of the PSA chip. A theoretical model is presented to estimate the gain performance of the PSA chip and two-period gain curves with approximately 7.8 dB extinction gain are measured which agree well with the simulation results.

2. Principle and chip fabrication

Figure 1 shows a microscope picture of the fabricated PSA chip after being wire-bonded. The coherent input light waves, which are coupled into the chip, consist of one signal to be phase-sensitive amplified in a nonlinear SOA, and two pumps to be amplified by two sampled grating distributed Bragg reflector (SG-DBR) lasers thanks to injection locking, and. An on-chip phase tuner is used to change the phase of the signal for observing the relationship between the PSA gain the signal phase.

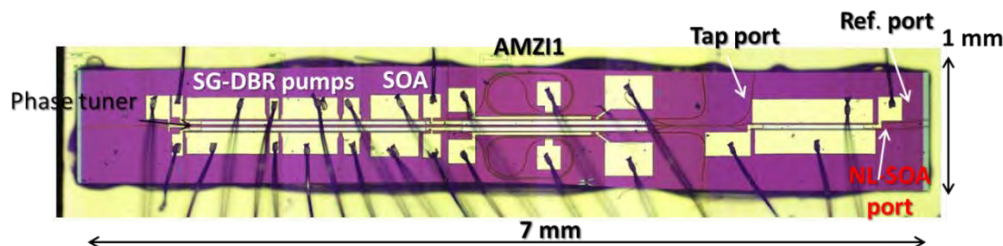


Fig. 1 Photo of the signal-degenerate dual-pumped PSA chip after wire-bonding

To monolithically integrate the single-chip PSA, we have chosen an InP/InGaAsP centered quantum well (CQW) platform with 10 quantum wells. Quantum well intermixing (QWI) technology [5] is used to define active and passive areas. More details about operation principle and chip fabrication can be found in [4].

3. Experimental results and theoretical simulation

First of all, basic configurations for each PSA were conducted to make sure that 1) the two SG-DBR lasers can be injection locked; 2) the power distributions among the signal and the pumps are optimized; 3) only the signal phase is affected by the phase tuner; 4) no signal interference on the chip. Then, we measured the phase shift of the signal when we tuned the phase tuner current. The result is shown in Fig. 2(a) and overall, $1 \text{ mA}^{0.5}$ gives π phase shift of the signal. A delay in phase shift when the current was less than 1 mA could be caused by an N+ sheet charge that exists at the regrowth interface. The optical spectra at the output of the NL-SOA were measured when the signal phase was changed, as shown in Fig. 2(b). The signal was amplified or attenuated as the phase tuner current was adjusted. Such a current- or phase-dependent signal power change could be caused by the PSA.

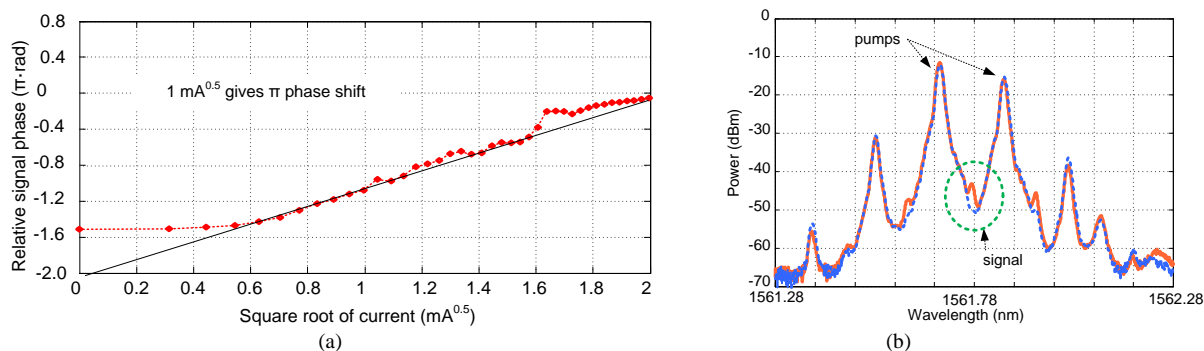


Fig. 2 (a) Measured relative signal phase change; (b) measured optical spectrum of the light wave at the output of the nonlinear SOA.

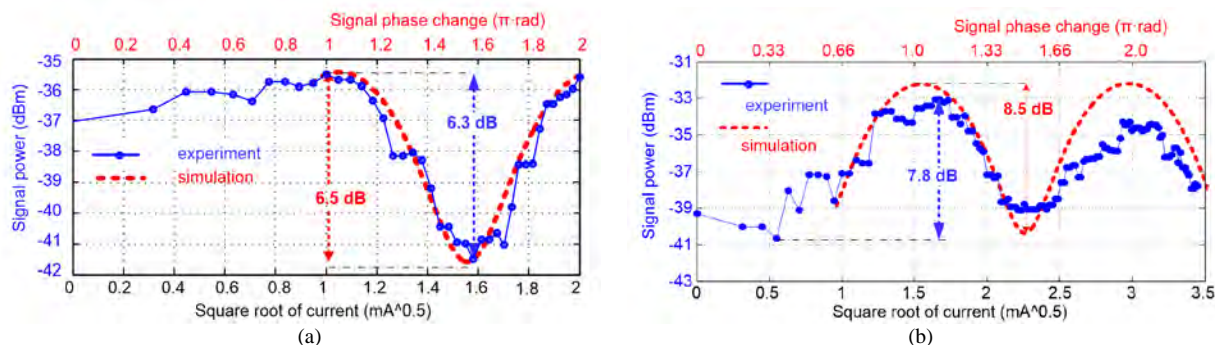


Fig. 3 Comparisons of the measured PSA gain curve and the theoretical simulation. (a) one-period PSA gain curve with 6.3 dB experimental and 6.5 dB theoretical results; (b) two-period PSA gain curve with 7.8 dB experimental and 8.5 dB theoretical results.

To specifically demonstrate and evaluate the PSA, the measured relationship among the signal power at the output of the SOA, the square root of the phase tuner current and the signal phase are shown in Fig. 3(a). Overall, $1 \text{ mA}^{0.5}$ gives π phase shift of the signal and one period oscillation of the signal. Clearly, such a signal power oscillation over one π instead of 2π phase indicates that the signal power change was caused by the PSA. Another PSA chip was chosen to demonstrate multiple periods of a PSA gain curve, as shown in Fig. 3(b), and about $1.5 \text{ mA}^{0.5}$ gives π signal phase shift and one period oscillation of the signal. A model for multi-wavelength mixing in SOAs based on coupled mode equations [6] is developed and applied to the nonlinear SOA on the PSA chip. The simulation results are superposed on Fig 3. By comparing the experimental data and the theoretical curves, good agreement is achieved.

4. References

- [1] J. Hansryd, P. A. Andrekson, M. Westlund, J. Li, and P.-O. Hedekvist, "Fiber-based optical parametric amplifiers and their applications," *IEEE Select. Topics Quantum Electron.* **8**, 506–520 (2002).
- [2] K. J. Lee, F. Parmigiani, S. Liu, J. Kakande, P. Petropoulos, K. Gallo, and D. J. Richardson, "Phase sensitive amplification based on quadratic cascading in a periodically poled lithium niobate waveguide," *Opt. Express* **17**, 20393–20400 (2009).
- [3] Z. Tong, C. Lundström, P. A. Andrekson, C. J. McKinstrie, M. Karlsson, D. J. Blessing, E. Tipsuwannakul, B. J. Puttnam, H. Toda, and L. Grüner-Nielsen, "Towards ultrasensitive optical links enabled by low-noise phase-sensitive amplifiers," *Nat. Photonics* **5**, 430–436 (2011).
- [4] W. Li, M. Lu, A. Mecozzi, M. Vasilyev, S. Arafat, D. Dadic, L. A. Johansson, L. A. Coldren, "First monolithically integrated dual-pumped phase-sensitive amplifier chip based on a saturated semiconductor optical amplifier," *IEEE J. Quantum Electron.* **52**, 1–12 (2016)
- [5] E. Skogen, J. Barton, S. Denbaars, and L. Coldren, "A quantum-well-intermixing process for wavelength-agile photonic integrated circuits," *IEEE J. Sel. Top. Quantum Electron.* **8**, 863–869 (2002).
- [6] C. Antonelli, A. Mecozzi, W. Li, and L. Coldren, "Efficient and accurate modeling of multi-wavelength propagation in SOAs: a generalized coupled-mode approach," *IEEE/OSA, J. Lightwave. Technol.*, to be published (2016)

I. Photonic Integrated Circuits

*C. Signal Processing with Active Micro-ring
Filters*

A fully reconfigurable photonic integrated signal processor

Weilin Liu^{1‡}, Ming Li^{1‡}, Robert S. Guzzon^{2‡}, Erik J. Norberg², John S. Parker², Mingzhi Lu², Larry A. Coldren² and Jianping Yao^{1*}

Photonic signal processing has been considered a solution to overcome the inherent electronic speed limitations. Over the past few years, an impressive range of photonic integrated signal processors have been proposed, but they usually offer limited reconfigurability, a feature highly needed for the implementation of large-scale general-purpose photonic signal processors. Here, we report and experimentally demonstrate a fully reconfigurable photonic integrated signal processor based on an InP–InGaAsP material system. The proposed photonic signal processor is capable of performing reconfigurable signal processing functions including temporal integration, temporal differentiation and Hilbert transformation. The reconfigurability is achieved by controlling the injection currents to the active components of the signal processor. Our demonstration suggests great potential for chip-scale fully programmable all-optical signal processing.

One of the fundamental challenges for digital signal processing (DSP) is the limited speed, largely restricted by the electronic sampling rate. In an optical network, signal processing is implemented based on DSP, which involves electronic sampling, optical-to-electrical (OE) and electrical-to-optical (EO) conversions. A solution to achieve power-efficient and high-speed signal processing in an optical network is to implement signal processing directly in the optical domain using a photonic signal processor to avoid the need for electronic sampling, OE and EO conversions^{1–3}. Numerous photonic signal processors have so far been reported based on either discrete components or photonic integrated circuits^{1–10}. Photonic signal processors based on discrete components usually have decent programming abilities but are more bulky and less power efficient, whereas a photonic integrated signal processor has a much smaller footprint and a higher power efficiency. A photonic signal processor can be used to implement fundamental signal generation and processing functions such as optical pulse shaping and arbitrary waveform generation¹, optical dispersion compensation⁷, temporal integration⁸, temporal differentiation⁹ and Hilbert transformation¹⁰. These functions are basic building blocks of a general-purpose signal processor for signal generation and fast computing. Fast computing processes such as temporal integration, temporal differentiation and Hilbert transformation have important applications^{11–22}. For example, a photonic integrator is a device that is able to perform the time integral of an optical signal, which has applications in dark soliton generation¹², optical memory¹³ and optical analog–digital conversion¹⁴. One of the most important characteristic parameters of a photonic integrator is the integration time. A long integration time means a better integration capability. An ideal photonic temporal integrator should have an infinite integration time. An on-chip all-optical integrator compatible with complementary metal oxide–semiconductor (CMOS) technology was reported¹⁵, based on an add-drop ring resonator with an integration time of 800 ps. For many applications, however, an integration time as long as a few nanoseconds is needed. To achieve such a long integration time, the insertion loss must be

precisely compensated to obtain a high Q -factor, which is very challenging, particularly for stable operation without causing lasing. In addition, an integrator with a fractional or higher order is also needed, which is more difficult to implement¹⁶. A photonic temporal differentiator¹⁷ is a device that performs temporal differentiation of an optical signal, and has applications in all-optical Fourier transform^{18,19}, temporal pulse characterization²⁰ and the demultiplexing of an optical time division multiplexed (OTDM) signal²¹, for example. A photonic Hilbert transformer is a device that derives the analytic representation of a signal¹⁰, and has been widely used for single-sideband (SSB) modulation. Optical SSB modulation is particularly useful in a radio-over-fibre (ROF) link to avoid dispersion-induced power fading²². Although the photonic implementations of these functions have been reported^{18–10,15,17}, a signal processor is usually designed to perform a specific function with no or very limited reconfigurability. For general-purpose signal processing, however, a photonic signal processor should be able to perform multiple functions with high reconfigurability.

In this Article, we report the design, fabrication and experimental demonstration of a fully reconfigurable photonic integrated signal processor to perform the three signal processing functions introduced above. The photonic signal processor consists of three active microring resonators (R1, R2, and R3) and a bypass waveguide as a processing unit cell, as shown in Fig. 1a,b. To obtain on-chip reconfigurability, we incorporate nine semiconductor optical amplifiers (SOAs) and twelve current-injection phase modulators (PMs) in the unit cell, as shown in Fig. 1b. The tunable coupling between two neighbouring rings and between the outer ring and the bypass waveguide is realized using four tunable couplers (TCs) with each consisting of two multi-mode interference (MMI) couplers and two PMs, as shown in the inset in Fig. 1b. The coupling ratio in each TC can be tuned by adjusting the injection currents to the two PMs in the TC. Within each ring there are two SOAs used to compensate for the waveguide propagation loss and the MMI splitting loss and insertion loss. When an SOA is forward biased it can create an optical gain. On the

¹Microwave Photonics Research Laboratory, University of Ottawa, Ottawa, Ontario K1N 6N5, Canada. ²Department of Electrical and Computer Engineering, University of California Santa Barbara, Santa Barbara, California 93116, USA. [†]Present address: State Key Laboratory on Integrated Optoelectronics, Institute of Semiconductors, Chinese Academy of Sciences, Beijing 100083, China. [‡]These authors contributed equally to this work.

*e-mail: jpyao@eecs.uottawa.ca

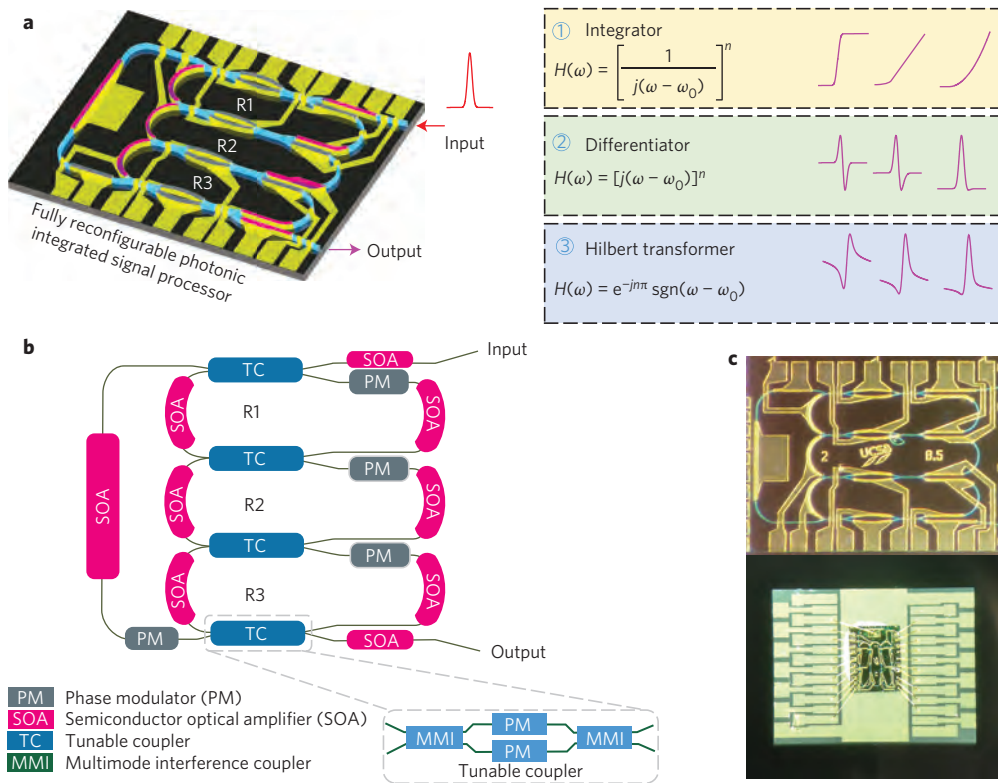


Figure 1 | The schematics of the proposed photonic integrated signal processor. **a**, The schematic diagram of the processor as a unit cell. **b**, A schematic representation of the processor consisting of three coupled rings and a bypass waveguide. **c**, The fabricated on-chip photonic signal processor prototype. The lower image shows the chip wire bonded to a carrier for experimental test.

other hand, an SOA can operate as an optical absorber when it is reverse biased, which is the key to achieving the configurability of the processor. Consequently, with the SOAs used in this design, a waveguide path could be on or off to facilitate the synthesis of various circuit geometries. By reverse biasing one SOA in each of the three ring resonators, for example, the three mutually coupled rings are reduced to a single optical path. With the bypass waveguide incorporated in the design, the chip can be reconfigured as a Mach-Zehnder interferometer (MZI). The signal processing functions can be implemented by reconfiguring the unit cell with a specific geometry (see Supplementary Section 1). In addition, there is a current-injection PM in each ring resonator, and a PM in the bypass waveguide, which are used to achieve wavelength tunability. Furthermore, the order of the signal processor, either a fractional or higher order, can be tuned by tuning the coupling ratio of the TC. The fabricated device, shown in Fig. 1c, is wire-bonded to a carrier to enable easy access to the SOAs and PMs with the assistance of a customized probe station. In the following, the proposed integrated photonic signal processor reconfigured to achieve three different functions for fast signal processing is discussed.

Photonic temporal integrator

An n th-order temporal integrator is a linear time-invariant (LTI) system with a transfer function given by¹⁶

$$H_n(\omega) = \left[\frac{1}{j(\omega - \omega_0)} \right]^n \quad (1)$$

where $j = \sqrt{-1}$, ω is the optical angular frequency and ω_0 is the carrier frequency of the signal to be processed. A first-order photonic temporal integrator can be implemented using an optical resonator, for example, an add-drop ring resonator¹⁶ (see Supplementary

Section 3-I). If the input and drop ports are used, the ring resonator would have a spectral response that is close to that given in (equation (1)) for $n = 1$, and it is a first-order temporal integrator. A higher-order (with $n = 2, 3, \dots$) temporal integrator can be implemented by cascading or coupling n first-order integrators¹⁶. An n th-order temporal integrator is capable of calculating the n th time integral of an arbitrary optical waveform.

The photonic integrated signal processor shown in Fig. 1 can be configured to operate as a temporal integrator with an order of 1, 2 or 3, depending on the number of rings used. In the unit cell, there are three mutually coupled ring resonators with two active SOAs in each ring resonator. If one SOA in a ring resonator is reverse-biased to shut off the waveguide, the ring resonator simply becomes a waveguide. By controlling the number of rings in the unit cell to be 1, 2 or 3, a temporal integrator with an order of 1, 2 or 3 is achieved (see Supplementary Sections 3-II, III). For example, a temporal integrator with an order of 1 is configured by shutting off two ring resonators, as shown in Fig. 2a. In each ring resonator, a current injection PM is incorporated that is used to tune the resonance frequency of the ring resonator, thus achieving wavelength tunability. In addition, the tunable coupling between two adjacent rings, and between an outer ring (R1 or R3) and the bypass waveguide, can offer tunable spectral response of the coupled-ring resonator, which can be used to achieve higher-order integrators.

Photonic temporal differentiator

An n th-order temporal differentiator provides the n th-order time derivative of the envelope of an optical signal. An n th-order temporal differentiator can be considered as an LTI system with a transfer function given by

$$H_n(\omega) = [j(\omega - \omega_0)]^n = \begin{cases} e^{jn(\pi/2)} |\omega - \omega_0|^n & \omega > \omega_0 \\ e^{-jn(\pi/2)} |\omega - \omega_0|^n & \omega < \omega_0 \end{cases} \quad (2)$$

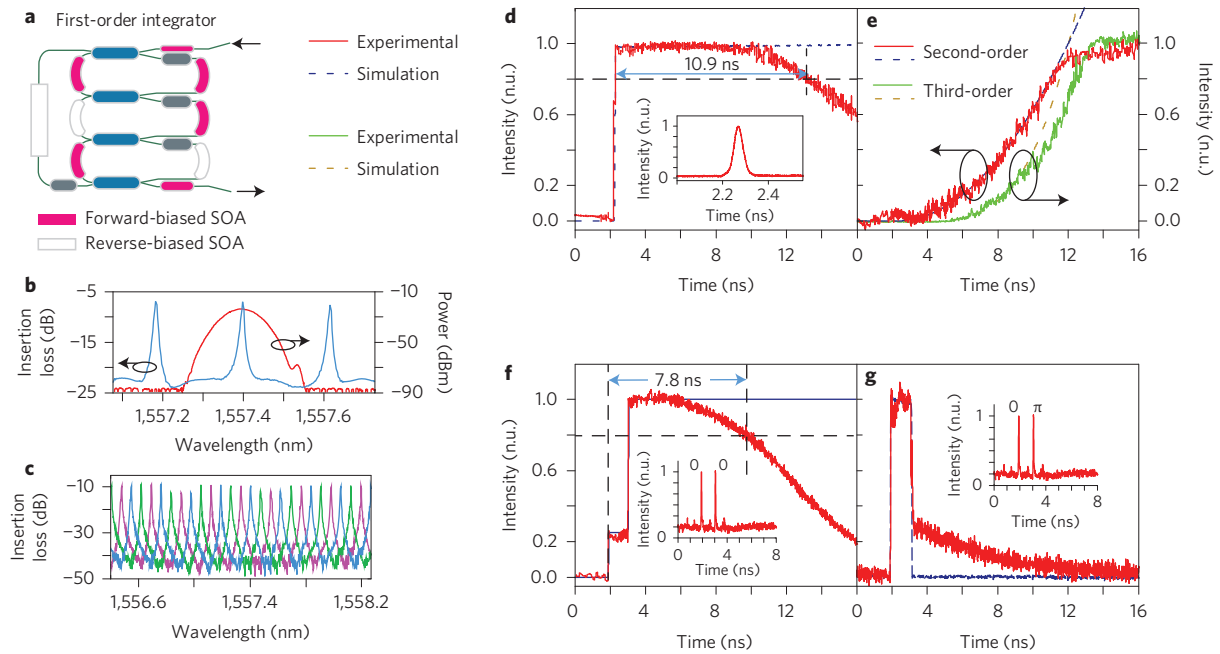


Figure 2 | Experimental results when the photonic integrated signal processor is configured as a temporal integrator. a, The configuration of the first-order integrator. **b**, The spectral response without injection current to the PM in the working ring resonator. **c**, The spectral response of the integrator when the injection current to the PM in the ring is tuned at three different values. **d**, The first-order integration of the Gaussian pulse with an integration time of 10.9 ns. Inset: The input Gaussian pulse with a temporal width of 54 ps. **e**, The second-order and third-order integration of the Gaussian pulse. **f**, The first-order integration of an in-phase doublet pulse, which is shown in the inset. **g**, The first-order integration of an out-of-phase doublet pulse. n.u., normalized unit.

As can be seen an n th-order temporal differentiator has a magnitude response of $|\omega - \omega_0|^n$ and a phase jump of $n\pi$ at ω_0 . An optical filter with a frequency response given by (equation (2)) can be implemented using an MZI²³ (see Supplementary Section 3-V). By controlling the coupling coefficients of the input and output couplers in an MZI, a tunable phase shift from 0 to 2π can be achieved, thus a temporal differentiator with a tunable fractional order can be implemented. The photonic integrated signal processor shown in Fig. 1 can be configured to have an MZI structure as shown in Fig. 3a. One arm of the MZI is formed by shutting off the three ring resonators in the unit cell, by applying a reverse bias to one of the two SOAs in each of the three ring resonators. The other arm is the bypass waveguide. The tuning of the fractional order is achieved by changing the coupling coefficients at both the input and output couplers. The operation wavelength can also be tuned by adjusting the injection current applied to the PM in one of the MZI arms.

Photonic temporal Hilbert transformer

A n th-order Hilbert transformer is an LTI system with a transfer function given by²⁴

$$H_n(\omega) = \begin{cases} e^{-jn(\pi/2)} & \omega > 0 \\ e^{jn(\pi/2)} & \omega < 0 \end{cases} \quad (3)$$

As can be seen, an n th-order Hilbert transformer has a magnitude response of 1 and a phase jump of $n\pi$ at ω_0 . A fractional Hilbert transformer becomes a conventional Hilbert transformer when $n = 1$. For $n = 0$, we have $H_0(\omega) = 1$, which is an all-pass filter. For $0 < n < 1$, the output is a weighted sum of the input signal and its conventionally Hilbert transformed signal²⁴. In addition, a fractional Hilbert transformer with an order of n is equivalent to two cascaded fractional Hilbert transformers with fractional orders of α and β if $\alpha + \beta = n$. A ring resonator can be used to implement a Hilbert transformer if the Q-factor is high (see Supplementary Section 3-IV). For a ring resonator with a high Q-factor, the spectral response is close to all pass, except for a narrow notch that is small enough and would contribute negligible

error to the transform²⁵. Figure 4a shows the configuration. Although the three ring resonators in the processor can be independently enabled or disabled, they are coupled in series. As a result, only one fractional Hilbert transformer or two cascaded fractional Hilbert transformers can be configured in the unit cell corresponding to a single-ring or two-cascaded-ring structure with all-pass configuration.

Results

The proposed signal processor is fabricated in an InP-InGaAsP material system that is wire-bonded to a carrier for experimental demonstration, as shown in Fig. 1c. The SOAs in each ring are measured to have a peak gain of 9.6 dB per SOA, which can be used to compensate for the insertion loss or to shut off the ring. The coupling coefficients of the TCs are measured at different injection currents to the PMs, which can be controlled from 0 to 100% when one of the PMs in each of the TCs is injected with a current from 0 to 3.5 mA (for injection currents applied to each active component, see Supplementary Section 2). There are twenty-one active components (SOAs and PMs) in a unit cell. When injection currents are applied, they will generate heat, which will shift the resonance wavelengths of the ring resonators and degrade the system stability. In the experiment, a temperature control unit is used to ensure the working temperature of the chip is 22 °C, to maintain stable operation.

Integrator. We first test the operation of the signal processor that is configured as a photonic temporal integrator with an order of $n = 1$. As a first-order integrator, the photonic integrated signal processor is configured to operate as a single ring resonator (R1 is on, R2 and R3 are off), as shown in Fig. 2a, where the output optical signal is converted to an electrical signal at a photodetector and monitored by an oscilloscope. The free spectral range (FSR) is measured by an optical vector analyser (OVA, Luna) to be 0.22 nm, as shown in Fig. 2b. By changing the injection current to the PM in the ring (the PM in R1), the spectral response of the ring is laterally shifted, thus the peak location is also shifted, as shown in Fig. 2c,

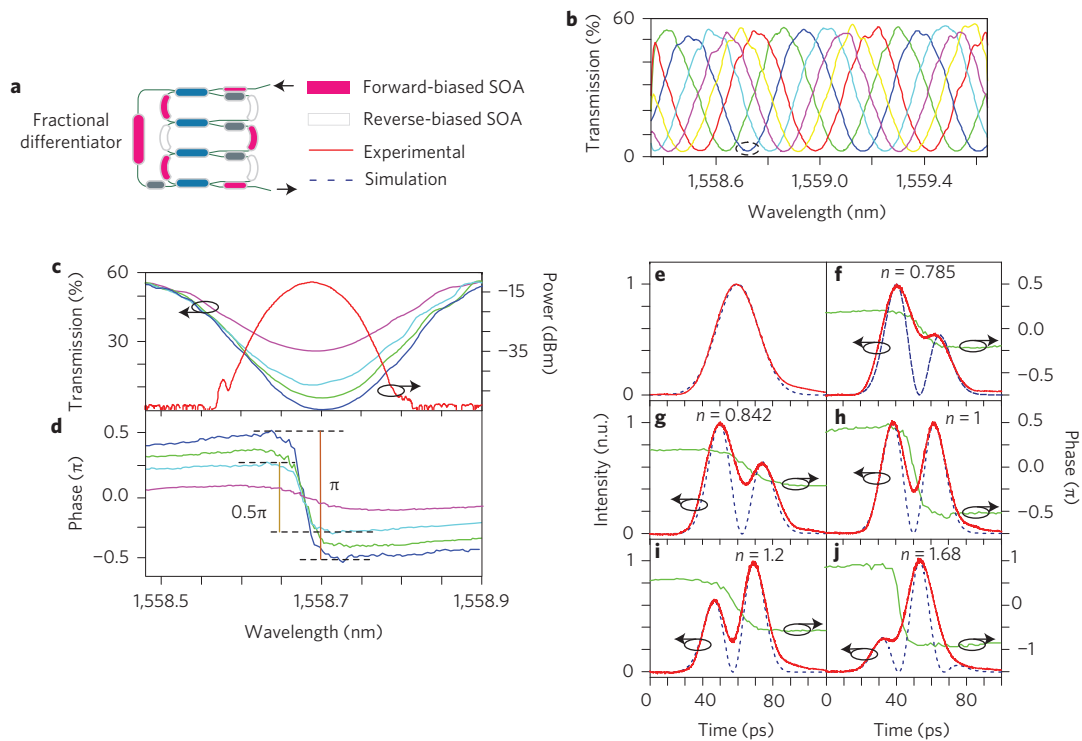


Figure 3 | Experimental results when the photonic integrated signal processor is configured as a fractional differentiator. **a**, The configuration. **b**, The spectral response with six different injection currents to the PM in the input tunable coupler of the MZI. **c,d**, The spectral response (**c**) and phase response (**d**) of the differentiator when the injection current to the PM in the MZI is tuned at four different values. **e**, The input Gaussian pulse with a temporal width of 33 ps. **f-j**, The fractional differentiation of the input Gaussian pulse with a fraction order of 0.785 (**f**), 0.842 (**g**), 1 (**h**), 1.2 (**i**) and 1.68 (**j**). n.u., normalized unit.

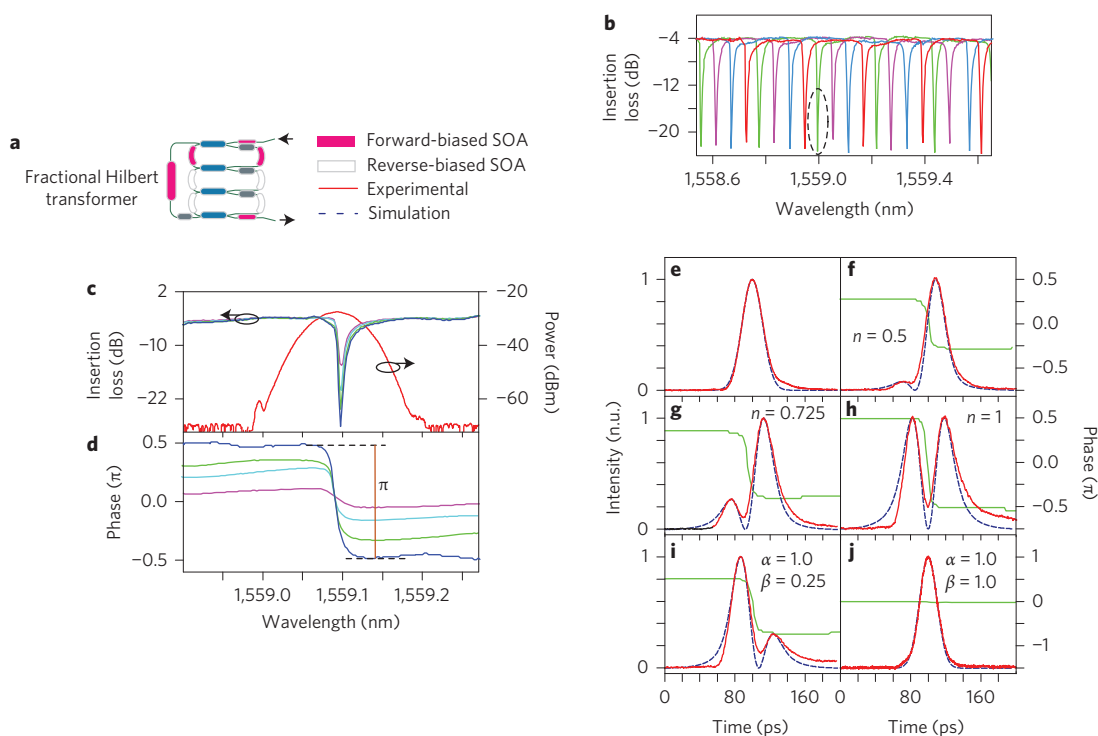


Figure 4 | Experimental results when the photonic integrated signal processor is configured as a Hilbert transformer. **a**, The configuration. **b**, The spectral response with four different injection currents to the PM in working ring resonator. **c,d**, The spectral response (**c**) and phase response (**d**) of the differentiator when the injection current to the PM in the working ring is tuned at four different values. **e**, The input Gaussian pulse with a temporal width of 33 ps. **f-h**, The fractional Hilbert transform of the input Gaussian pulse with a fraction order of 0.5 (**f**), 0.725 (**g**) and 1 (**h**). **ij**, The results of the cascaded Hilbert transformers with fraction orders of (1.0, 0.25) and (1.0, 1.0). n.u., normalized unit.

which confirms the tuning of the working wavelength. In the experiment, an optical Gaussian pulse generated by a mode-locked laser (MLL) source and spectrally shaped by an optical bandpass filter (Finisar, WaveShaper 4000S) with a full width at half maximum (FWHM) of 46 ps centred at 1,557.4 nm, as shown as the red curve in Fig. 2b and the inset in Fig. 2d, is then coupled into the temporal integrator via a lensed fibre. Figure 2d shows the first-order temporal integral of the input Gaussian pulse. The integration time is measured to be 10.9 ns, which is more than one order of magnitude longer than the result reported in ref. 15. With a rising time of 48 ps, the proposed photonic integrator offers a time–bandwidth product¹⁵ (TBWP, a principal figure of merit, represents the throughput limit for an optical system determined by the product of the bandwidth and the time–bandwidth of the optical system) of 227, which is much higher than an advanced electronic integrator (TBWP < 10)²⁶, and also more than two-times greater than the previously reported photonic integrator (TBWP ~ 100)¹⁵. The Q-factor is also calculated based on the integration time, which is ~50 million.

Then, the photonic integrated signal processor is configured as a second-order (where R1 and R2 are on and R3 is off), and a third-order (where R1, R2 and R3 are all on) temporal integrator with two and three coupled ring resonators on the chip. The integration of the input Gaussian pulse at the outputs of the second- and third-order temporal integrator is then obtained (Fig. 2e). A higher order integrator, such as a second- and third-order integrator, can be used, for example, to solve higher-order ordinary differential equations^{15,16}. A second-order integrator can also be used for arbitrary waveform generation¹¹. The first-order integral of an in-phase and out-of-phase doublet pulse is also computed by the proposed first-order temporal integrator. An in-phase/out-of-phase doublet consists of two temporally separated in-phase/out-of-phase Gaussian waveforms with identical amplitude profile. As shown in Fig. 2f,g, the temporal integrator sums up the area under the two field amplitude waveforms for the case of in-phase doublet pulse. As the phase relationship between the two pulses of the in-phase doublet is not maintained during repeated round-trips in the ring resonator due to the dynamic intensity-dependent refractive index variations, the magnitude of the integration output is not well maintained, which leads to a reduced integration time of 7.8 ns. For the case of out-of-phase doublet pulse, the time integral of the second waveform in the doublet pulse cancels that of the first waveform, leading to a square-like profile with the duration determined by the time delay between the two waveforms of the doublet pulse. As shown in Fig. 2g, the two out-of-phase pulses do not subtract completely, this is because the two pulses are not perfectly identical in amplitude and phase due to a slight asymmetry of the MZI used to generate the two pulses (the two pulses are generated by splitting a single pulse to two pulses and recombining the time-delayed pulses at the output of the MZI). These results suggest important applications of a photonic integrator as a memory unit, such as ‘write’ and ‘erase’ operations¹⁵. Simulations are also performed to calculate the temporal integral of the input pulse and the results are plotted with dashed line as shown in Fig. 2d–g. As can be seen, the experimental results agree well with the simulation results. The active components such as the SOAs and PMs in the processor offer a precise control of the resonance peak and the Q-factor of each ring resonator, which is indispensable for achieving higher-order integration⁸. This is the first time that a higher order (up to 3) photonic temporal integrator is implemented on an integrated chip.

Differentiator. We test the operation of the signal processor configured to have an MZI structure to operate as a fractional-order temporal differentiator (where R1, R2 and R3 are all off, forming one arm of the MZI, the bypass waveguide forms another arm of the MZI), as shown in Fig. 3a. Again, a photodetector is connected at

the output of the chip to convert the optical signal to an electrical signal. The spectral response of the MZI is shown in Fig. 3b. It has an FSR of 0.44 nm. By changing the injection current to the PM in one of the two arms, the spectral response is then laterally shifted, as shown in Fig. 3b. By changing the injection current to the PMs in the tunable couplers at the input or output of the MZI, the coupling coefficient can be tuned to achieve tunable phase shift at the transmission notch. Figure 3c,d shows the measured transmission notch with a phase jump from 0 to π by an optical vector network analyser (OVA, Luna). A Gaussian pulse with a temporal width of 33 ps centred at 1,558.7 nm, shown in Fig. 3c,e, is coupled into the chip. Five differentiated pulses corresponding to five differentiation orders of 0.785, 0.842, 1, 1.2, and 1.68 are obtained, which are shown in Fig. 3f–j, respectively. The phase information of the differentiated pulses is also shown. Again, simulations are also performed to calculate the temporal differentiation of the input Gaussian pulse with five differentiation orders of 0.785, 0.842, 1, 1.2, and 1.68. The results are also shown in Fig. 3f–j. As can be seen, the experimental results agree well with the simulation results. The slight mismatch in the dip between the simulation and experimental output waveforms is due to the limited bandwidth of the photodetector. The proposed differentiator can provide an analog processing bandwidth of 55 GHz, as can be seen from Fig. 4c, which is significant larger than an electronic microwave differentiator²⁷. With such a large bandwidth, the photonic differentiator can provide fast signal processing and signal coding²³. In addition, the differentiation order is also tunable, which provides better flexibility in signal processing, such as tunable image enhancement²⁸ (see Supplementary Section 4-1).

Hilbert transformer. The photonic integrated signal processor can also be configured to have a single ring or two cascaded ring structure to operate as a fractional Hilbert transformer or two cascaded fractional Hilbert transformers. Figure 4a shows the configuration as a single-ring fractional Hilbert transformer (R1 is on, R2 and R3 are off). The spectral response of the single-ring fractional Hilbert transformer is measured and shown in Fig. 4b with an FSR of 0.22 nm. By changing the injection current to the PM in the ring, the notch location is tuned and the FSR is slightly changed as shown in Fig. 4b. The phase response which determines the fractional order of the Hilbert transform can also be tuned by changing the coupling coefficient between the ring and the bypass waveguide, as shown in Fig. 4c,d, which is achieved by changing the injection current to the PMs in the TCs. To validate the operation of the processor as a fractional Hilbert transformer, an optical Gaussian pulse with a central wavelength at 1,559.1 nm and a temporal width of 33 ps, shown in Fig. 4e, is coupled into the chip. The fractional order of the Hilbert transformer is continuously tunable from 0 to 1 by changing the coupling coefficient through controlling the injection currents to the PMs in the TC. Figure 4f–h shows the fractionally Hilbert transformed pulses with a tunable fractional order from 0.5 to 1. The fractional order Hilbert transformer can be used to construct a secure communication system²⁴, in which the fractional order n is used as a secret key for demodulation. If the order n is unknown in the demodulation, the signal cannot be recovered. The proposed fractional order Hilbert transformer can also provide fast tunability of the fractional order, which can find applications in secure communication systems.

The signal processor can also be configured as two cascaded Hilbert transformers (R1 and R3 are on, and R2 is off). Figure 4h,i shows the output pulses with the fractional orders of (1.0, 0.25) and (1.0, 1.0) which are equivalent to a single Hilbert transformer with a fractional order of 1.25 and 2. Again, the tuning is achieved by changing the coupling coefficients through controlling the injection currents to the PMs in the tunable couplers. Comparing to the most

recently reported tunable fractional Hilbert transformer in a chip-scale device¹⁰, the proposed Hilbert transformer offers a much easier control of the tunable fractional order through tuning the injection current instead of changing the polarization states of the input signal.

Discussion and summary

The proposed photonic signal processor can be reconfigured as a photonic temporal integrator, differentiator, and Hilbert transformer, which are basic building blocks for general-purpose signal processing (application examples are given in Supplementary Section 4, and performance evaluation is given in Supplementary Section 5). The proposed photonic signal processor can be used to provide high-speed processing to break the speed and bandwidth bottleneck of an electronic processor. For example, a photonic temporal integrator is one of the most important components in a delta-sigma converter for optical analog-to-digital conversion¹⁴. A photonic temporal differentiator can be used in demultiplexing an OTDM signal²¹ and performing real-time amplitude and phase measurement of an optical signal. A Hilbert transformer can be used to generate a wideband SSB modulated signal (see Supplementary Section 4-II), which is useful in a radio-over-fibre (RoF) link to avoid dispersion-induced power penalty²². If the designed photonic signal processor is employed in an optical network, the above-mentioned functionalities can be achieved with a single integrated photonic chip. More importantly, with the development of all-optical networks, photonic signal processors can be incorporated into an optical network to perform fast signal processing without digital sampling, and OE and EO conversions. Thus, the proposed photonic signal processor can provide a potential cost-effective solution for signal processing in future all-optical networks.

In summary, we have designed, fabricated and demonstrated a fully reconfigurable photonic integrated signal processor based on a photonic integrated circuit. The operation of the signal processor reconfigured as a temporal integrator, a temporal differentiator and a Hilbert transformer with a tunable order and a tunable operation wavelength was demonstrated experimentally. In particular, a temporal integrator over a bandwidth of 0.22 nm with an integration time of 10.9 ns was achieved, which is the longest integration time ever reported. Although some photonic signal processing functions, such as arbitrary waveform generation and optical dispersion compensation, are not implemented with the current design, this work represents an important step towards the realization of a fully programmable high speed and wideband general-purpose photonic signal processor that can overcome the inherent speed limitation of electronic signal processors.

Methods

Methods and any associated references are available in the [online version of the paper](#).

Received 7 April 2015; accepted 28 December 2015;
published online 15 February 2016

References

- Kahn, M. *et al.* Ultrabroad-bandwidth arbitrary radiofrequency waveform generation with a silicon photonic chip-based spectral shaper. *Nature Photon.* **4**, 117–122 (2010).
- Yu, R. *et al.* A scalable silicon photonic chip-scale optical switch for high performance computing systems. *Opt. Express* **21**, 32655–32667 (2013).
- Willner, A. E., Khaleghi, S., Chitgarha, M. R. & Yilmaz, O. F. All-optical signal processing. *J. Lightw. Technol.* **32**, 660–680 (2014).
- Koos, C. *et al.* All-optical high-speed signal processing with silicon-organic hybrid slot waveguides. *Nature Photon.* **3**, 216–219 (2009).

- Weiner, A. M. Ultrafast optical pulse shaping: a tutorial review. *Opt. Commun.* **284**, 3669–3692 (2011).
- Almeida, V. R., Barrios, C. A., Panepucci, R. & Lipson, M. All-optical control of light on a silicon chip. *Nature* **431**, 1081–1084 (2004).
- Doerr, C. R. & Okamoto, K. Advances in silica planar lightwave circuits. *J. Lightw. Technol.* **24**, 4763–4789 (2006).
- Slavík, R. *et al.* Photonic temporal integrator for all-optical computing. *Opt. Express* **16**, 18202–18214 (2008).
- Ngo, N. Q., Yu, S. F., Tjin, S. C. & Kam, C. H. A new theoretical basis of higher-derivative optical differentiators. *Opt. Commun.* **230**, 115–129 (2004).
- Shahoei, H., Dumais, P. & Yao, J. P. Continuously tunable photonic fractional Hilbert transformer using a high-contrast germanium-doped silica-on-silicon microring resonator. *Opt. Lett.* **39**, 2778–2781 (2014).
- Ashrafi, R. *et al.* Time-delay to intensity mapping based on a second-order optical integrator: application to optical arbitrary waveform generation. *Opt. Express* **23**, 16209–16223 (2015).
- Ngo, N. Q. & Binh, L. N. Optical realization of Newton-Cotes-based integrators for dark soliton generation. *J. Lightw. Technol.* **24**, 563–572 (2006).
- Hill, M. T. *et al.* A fast low power optical memory based on coupled micro-ring lasers. *Nature* **432**, 206–209 (2004).
- Reeves, E., Costanzo-Caso, P. & Siahmakoun, A. Theoretical study and demonstration of photonic asynchronous first-order delta-sigma modulator for converting analog input to NRZ binary output. *Microw. Opt. Technol. Lett.* **57**, 574–578 (2015).
- Ferrera, M. *et al.* On-chip CMOS-compatible all-optical integrator. *Nature Commun.* **1**, 1–5 (2010).
- Ferrera, M. *et al.* All-optical first and second-order integration on a chip. *Opt. Express* **19**, 23153–23161 (2011).
- Liu, F. *et al.* Compact optical temporal differentiator based on silicon microring resonator. *Opt. Express* **16**, 15880–15886 (2008).
- Hillerkuss, D. *et al.* Simple all-optical FFT scheme enabling Tbit/s real-time signal processing. *Opt. Express* **18**, 9324–9340 (2010).
- Hillerkuss, D. *et al.* 26 Tbit s⁻¹ line-rate super-channel transmission utilizing all-optical fast Fourier transform processing. *Nature Photon.* **5**, 364–371 (2011).
- Li, F., Park, Y. & Azaña, J. Complete temporal pulse characterization based on phase reconstruction using optical ultrafast differentiation (PROUD). *Opt. Express* **32**, 3364–3366 (2007).
- Slavík, R. *et al.* Demultiplexing of 320 Gbit/s OTDM data using ultrashort flat-top pulses. *IEEE Photon. Technol. Lett.* **19**, 1855–1857 (2007).
- Sima, C. *et al.* Phase controlled integrated interferometric single-sideband filter based on planar Bragg gratings implementing photonic Hilbert transform. *Opt. Express* **38**, 727–729 (2013).
- Park, Y., Azaña, J. & Slavík, R. Ultrafast all-optical first- and higher-order differentiators based on interferometers. *Opt. Lett.* **32**, 710–712 (2007).
- Tseng, C. C. & Pei, S. C. Design and application of discrete-time fractional Hilbert transformer. *IEEE Trans. Circ. Syst. II* **47**, 1529–1533 (2000).
- Liu, W. *et al.* in *Proceedings of the Optical Fiber Communications Conference (OFC) paper Tu2A.6* (Optical Society of America, 2014).
- Tsai, L.-C. & Fang, H.-S. Design and implementation of second-order microwave integrators. *Microw. And Opt. Tech. Lett.* **53**, 1983–1986 (2011).
- Hsue, C.-W., Tsai, L.-C. & Chen, K.-L. Implementation of first-order and second-order microwave differentiator. *IEEE Trans. Microw. Theory Tech.* **52**, 1443–1447 (2004).
- Mathieu, B., Melchior, P., Oustaloup, A. & Ceyral, C. Fractional differentiation for edge detection. *Signal Process.* **83**, 2421–2432 (2003).

Acknowledgements

This work was sponsored by the Natural Sciences and Engineering Research Council of Canada (NSERC). The authors also acknowledge support from the Nanofabrication Center at UCSB.

Author contributions

W.L. analysed the data. W.L., M.L., R.S.G. and J.Y. conceived and designed the experiments. W.L., R.S.G., E.J.N., J.S.P., M.L. and L.C. contributed materials and analysis tools. W.L. performed the experiments. W.L., M.L. and J.Y. wrote the paper.

Additional information

Supplementary information is available in the [online version of the paper](#). Reprints and permissions information is available online at www.nature.com/reprints. Correspondence and requests for materials should be addressed to J.Y.

Competing financial interests

The authors declare no competing financial interests.

Methods

Device fabrication. The designed chip with a single unit cell has a size of 1.5×2 mm. In the unit cell, the length of each ring resonator is 3 mm. Two 400- μm SOAs with a confinement tuning layer offset quantum well (CTL-OQW) structure are fabricated in each ring to provide a peak gain of 9.6 dB per SOA to compensate for the insertion loss or to shut off the ring. With the ring length of 3 mm subtracting the length of the two SOAs (400 μm each) in each ring resonator and 7.4 dBcm^{-1} of passive waveguide loss, the total waveguide propagation loss is 1.6 dB for each ring resonator. In addition, each MMI coupler in the ring resonator has 0.5 dB insertion loss. Thus the total round-trip loss is ~ 3.6 dB, which can be compensated by the SOAs. In the bypass waveguide, there is an SOA with a length of 600 μm to compensate for the insertion loss or to shut off the bypass waveguide. Two additional active SOAs are incorporated into the processor at the input and output waveguides to compensate for the fibre coupling losses, as shown in Fig. 1. In addition, the facets of the bypass waveguides are angled at 7° to minimize the reflections. The peak power of the input optical signal should be below ~ 13 dBm to avoid damaging the input/output facets. The phase modulation in the ring and the tuning of the coupler are accomplished by forward bias currents via current injection and free carrier absorption through the carrier plasma effect in the PMs. The PMs in the chip are fabricated with a length of 300 μm .

The chip was fabricated on a quarter of a wafer that was grown at UCSB. At the beginning, the areas in the chip for the SOAs, passive (low loss waveguide propagation), and phase modulator, are defined by using semiconductor wet-etching

techniques. After regrowth, the deeply-etched waveguides are defined. The waveguide etch is performed using a 200 $^\circ\text{C}$ ICP-RIE dry etch. To make contact to SOAs and PMs, vias need to be constructed and metallization applied to the device. First, the newly-etched sample is coated in 300 nm of silicon nitride using PECVD. This provides the electrical insulation required such that metal traces and pads can be placed on the surface of the photonic integrated chip (PIC). Then, a partial exposure is performed on sections of waveguide where vias are desired.

To ease testing, the chips need to be cleaved apart and made secure on a carrier for wire bonding. The carrier provides structural integrity and large pads for probing with probe cards. The individual devices are mounted with solder onto an aluminum nitride carrier and then wire-bonded to the carrier pads.

Pulse generation and measurement. We used a mode-locked laser source with a repetition rate of 48.6 MHz and a central wavelength at 1,558.7 nm to generate an optical pulse, and the pulse width is controlled by a programmable optical filter (Finisar, WaveShaper 4000S) connected at the output of the mode-locked laser source. The in-phase and out-of-phase doublet pulses are generated using an unbalanced MZI by launching an optical Gaussian pulse into the MZI with a length difference between the two arms of 25 cm. As a result, two closely separated pulses with a temporal separation of 1.14 ns are generated. Depending on the phase shift applied to one pulse by a phase modulator in one arm of the MZI, an in-phase (no phase shift) or out-of-phase (π phase shift) doublet pulse is generated.

A Wavelength Tunable Optical Buffer Based on Self-Pulsation in an Active Microring Resonator

Weilin Liu, *Student Member, IEEE*, Bruno Romeira, Ming Li, Robert S. Guzzon, Erik J. Norberg, John S. Parker, Larry A. Coldren, *Fellow, IEEE*, and Jianping Yao, *Fellow, IEEE, Fellow, OSA*

Abstract—A wavelength tunable optical buffer with the ability to achieve data recovery based on self-pulsation in an active microring resonator is proposed and experimentally demonstrated. The key component in the optical buffer is the microring resonator which is implemented based on an InP–InGaAsP material system incorporating two semiconductor optical amplifiers and a phase modulator, ensuring an ultrahigh Q -factor and a tunable resonance wavelength for fast self-pulsation operating at gigahertz frequencies. An optical carrier modulated by an arbitrary pulse sequence is used to trigger the self-pulsation in the microring resonator, while its output is coupled to a fiber-optic delay line in an optoelectronic delayed feedback configuration, a recursive system for data storage. Optical buffering and data recovery at 1 Gb/s are experimentally demonstrated, which is the fastest optical buffer ever reported based on self-pulsation in a microring resonator. The proposed optical buffer can be employed to perform critical telecommunication buffer functions including writing, storage, re-shaping, healing, and erasing.

Index Terms—Optical buffering, optical pulse generation, optical resonators.

I. INTRODUCTION

AN optical buffer, which stores optical signals for a short period of time, can find numerous applications such as optical storage [1], optical packet switching [2], and all-optical signal processing [3]. As one of the fundamental building blocks in an all-optical system, an all-optical buffer can provide optical storage directly in the optical domain without the need for optical-to-electrical and electrical-to-optical conversions, which will increase the signal processing speed and reduce the power consumption as compared with an electronic buffer. In the last few years, numerous approaches have been proposed to implement optical buffers. At present, five major approaches have been employed for the implementation of optical buffers. The first approach is to use an optical delay-line with a long time

delay for the storage of an optical signal [4], [5], the second is to use the slow light effect in an optical medium to decrease the group velocity for optical buffering [6]–[10], the third is to use the optical Kerr effect to copy and sustain an optical bit as a temporal soliton in an optical cavity [11], the fourth is to use the class II excitability [12] in an array of cascaded microring resonators to achieve optical delay [13], and the fifth is to use the two stable states as ‘0’ and ‘1’ in photonic crystal nanocavities for optical buffering [14].

Specifically, in the first approach, a length of optical fiber or waveguide is used to provide a desired time delay for data buffering. In 2004, Yeo *et al.* experimentally demonstrated an optical fiber delay-line buffer with an adjustable time delay to provide dynamical reconfigurability of optical buffering within nanoseconds [4]. In such a delay-line-based optical buffer, the time delay is offered by the physical length of the optical fiber; as a result, the size of the buffering system is inevitably large if a considerable amount of delay is needed. Recent advances in photonic integrated circuits (PICs) have led to the development of ultra-long optical delay line on a silicon chip for optical buffering. At present, a delay line as long as 250 m has been demonstrated on a silicon chip over an area of $9.5 \text{ cm} \times 9.5 \text{ cm}$ [5]. Delay line buffers provide a practical solution for all-optical buffering with a large bandwidth. However, these delay-line buffers need optical switches to route the light in the delay-line structure to achieve a reconfigurable time delay, which would increase system complexity and introduce extra losses.

In the second approach, an optical buffer is implemented based on the slow light effect in an optical material that has strong dispersion. In such a material, optical waves with different wavelengths propagate at different speeds and thus the group velocity of the optical waves can be reduced. By making the dispersion of the material sufficiently strong, the group velocity can be significantly reduced, to be less than the speed of light in vacuum, which can be used to provide the time delay in an optical buffer. To date, numerous techniques to implement optical buffers based on slow light effects in various materials have been reported. These slow light mechanisms include electromagnetically induced transparency [6], coherent population oscillations [7], stimulated Brillouin scattering effects [8], optical parametric amplifying [9], and resonating in an optical waveguide [10]. Although slow light effects open up great opportunities to manipulate the speed of light and thus implement optical buffers, there are challenges such as small bandwidth and large losses.

In the third approach, an optical buffer is implemented by exciting temporal cavity solitons in a resonator. Temporal

Manuscript received February 01, 2016; revised April 15, 2016; accepted May 11, 2016. Date of publication May 25, 2016; date of current version June 22, 2016. This work was supported by the Natural Sciences and Engineering Research Council of Canada.

W. Liu and J. P. Yao are with the Microwave Photonics Research Laboratory, School of Electrical Engineering and Computer Science, University of Ottawa, Ottawa, ON K1N 6N5, Canada (e-mail: jpyao@eecs.uottawa.ca).

B. Romeira is with the COBRA Research Institute, Eindhoven University of Technology, 5600 MB Eindhoven, The Netherlands.

M. Li is with the Institute of Semiconductors, Chinese Academy of Sciences, Beijing 100044, China.

R. S. Guzzon, E. J. Norberg, J. S. Parker, and L. A. Coldren are with the Department of Electrical and Computer Engineering, University of California Santa Barbara, Santa Barbara, CA 93116 USA.

Color versions of one or more of the figures in this paper are available online at <http://ieeexplore.ieee.org>

Digital Object Identifier 10.1109/JLT.2016.2567456

cavity solitons exist as temporally localized pulses in a resonator pumped by an externally driving field, which can be excited through a phase-insensitive and wavelength-insensitive process [11]. By modulating the data bits on the driving optical beam, the temporal cavity solitons are excited in a sequence corresponding to the data bits. Leo *et al.* demonstrated an optical buffer based on temporal cavity solitons, which could capture a 40 kbit sequence from a 25 Gb/s optical data stream and provide continuously looped optical read-out of the data at the original data rate of 25 Gb/s [11]. However, this approach can only enable optical buffering for optical wavelengths close to the resonance wavelength of the cavity. Additionally, this optical buffer requires a strong optical input signal to excite the Kerr nonlinearity and the writing procedure is very complicated. Furthermore, erasing of the data was not experimentally demonstrated.

In the fourth approach, the time delay for achieving optical buffering can be obtained by an excitable photonic neural circuit [13]. A microring resonator can be excitable if it is pumped by a continuous-wave (CW) light wave with a sufficiently high power at the blue side of its resonance due to the thermal and free-carrier nonlinearities [13]. Van Vaerenbergh *et al.* proposed an optical delay line based on an array of excitable silicon-on-insulator (SOI) microring resonators. With a time delay of 200 ns obtained by simulation, the proposed delay line can be employed for information buffering at a speed of MHz in a spiking neural network. However, the buffering speed is limited to MHz frequencies.

In the fifth approach, photonic crystal nanocavities are used to store optical signals based on the transmittance bistability [14]. In a photonic crystal nanocavity, the cavity resonance wavelength can be shifted by varying the input optical power due to optical nonlinearity. As a result, the transmittance of optical signals via the cavity can be switched by changing the input optical power, and the transmittance exhibits bistability as a function of the input power. By assigning the two bistable states as ‘0’ and ‘1’, an optical buffer is obtained. An optical pulse can then be used to change the bistable states for memory operation allowing writing and erasing of data. This approach can provide a large bandwidth for optical buffering, and a buffering speed as high as 40 Gb/s was experimentally demonstrated in [14]. However, since a nanocavity offers only one bit storage, multi-bits have to be stored in an array of nanocavities. Consequently, the writing, erasing, and reading are very difficult since selective coupling of an optical pulse to a specific cavity in the nanocavity array is needed.

In this paper, we propose a novel approach to the implementation of a wavelength tunable optical buffer based on self-pulsation in an active microring resonator at a high bit rate (up to GHz). Self-pulsation oscillations in the MHz range based on slow thermal oscillations have been demonstrated [12]. To increase the speed of self-pulsation oscillations for optical buffering, slow thermal oscillations should be suppressed to allow pure and fast coupled electron-photon oscillations at GHz range [14]. In this work, we demonstrate the generation of GHz oscillations based on coupled electron-photon dynamics in an ultrahigh- Q resonator with a buffering data rate of 1 Gb/s. To our knowledge,

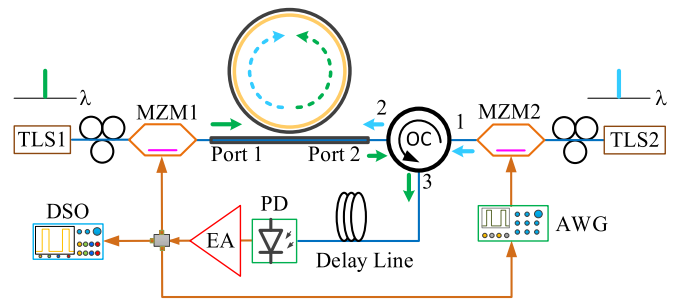


Fig. 1. Schematic of the proposed optical buffer based on a ring resonator. TLS: tunable laser source; MZM: Mach-Zehnder modulator; OC: optical circulator; PD: photodetector; AWG: arbitrary waveform generator; EA: electric amplifier; DSO: digital storage oscilloscope.

this is the fastest pure GHz oscillations in the absence of slow thermal oscillations reported to date using microring resonators [12]. The proposed optical buffer is experimentally evaluated. Optical buffering and data recovery at 1 Gb/s are demonstrated. As the buffering time is determined by the length of the optical delay line in the system, a desired buffering time can be obtained by choosing the length of the optical delay line. However, since the buffering capacity, which is the maximum number of bits that can be stored in the buffer, is determined by the ratio between the loop delay time and the self-pulsation time, for a fixed delay line we can store a data sequence with the number of bits equal to or smaller than the buffering capacity. Compared with other optical buffers reported in [4]–[14], the proposed optical buffer offers a few advantages. 1) There is no need to use multiple cascaded integrated devices to realize an optical memory with a bit storage higher than one bit. 2) The proposed optical buffer offers a GHz-range optical buffering speed with a tunable wavelength. 3) Data erasing and data recovery capabilities are also available with the proposed optical buffer which are demonstrated experimentally.

II. PRINCIPLE

The schematic of the proposed optical buffer is shown in Fig. 1. As can be seen, a microring resonator is incorporated in an optoelectronic delay-line loop to provide self-pulsation for optical buffering. In the proposed configuration, the microring resonator works as a nonlinear node that is triggered to generate a self-pulsating signal in response to an incoming signal, enabling to write, reshape and restore the information in the optical buffer, while the delay line in the configuration is used as a temporal buffer to store the information. The self-pulsation in the proposed system is a result of strong nonlinearities in the resonator, and a result from the balance between the nonlinear response and the photon cavity lifetime [15]–[18]. In our system, when a light wave with a high power density is coupled into the microring resonator, free carriers are generated as a result of two-photon absorption (TPA) [17], which changes the effective refractive index of the ring resonator. Since the free carriers have very short lifetimes, the resonance wavelength change of the ring resonator caused by the interaction between the free-carrier dispersion and the TPA is unstable [18]. As a result,

self-pulsation is triggered, and the achievement of a self-sustained oscillation requires a positive feedback mechanism which is provided by the dynamical tuning of the cavity resonance as a function of the carrier density that modulates the stored energy in the cavity. The frequency of the self-pulsation, which in our case is in the GHz range, is determined by the lifetime of the free-carriers generated by two-photon absorption in the ring resonator [15]. This differs substantially from the self-oscillations created by the competition between thermal and free carrier effects, which is limited to MHz frequencies [12]. By using the InP–InGaAsP material system, which is reported to be very efficient in suppressing heat accumulation [14], thermal-optic induced low speed self-pulsation is absent in our microring resonators. Taking advantage of the fast self-pulsating oscillations, a fast optical buffer can be achieved using the self-pulsation in an active microring resonator triggered by the input optical signal carrying data with its wavelength close to one resonance wavelength of the microring resonator. The self-pulsation in the microring resonator can be controlled according to the data in the input optical signal, and thus the generated pulse train is used to re-shape, restore and heal the incoming data bits whereas a recursive optoelectronic loop is employed for signal storage as shown in Fig. 1. To enable wavelength tunable optical buffering, a phase modulator (PM) is also incorporated inside the ring resonator to laterally shift the resonance wavelength to make it close to the wavelength of the input optical signal.

As shown in Fig. 1, the output of an active microring resonator is coupled to a long delay line in an optoelectronic delayed feedback configuration, which consists of a tunable laser source (TLS1), a Mach–Zehnder modulator (MZM1), a microring resonator, an optical delay line, a photodetector (PD), and an electronic amplifier. The data buffering is realized as follows. By tuning the wavelength of TLS1 close to one resonance wavelength of the microring resonator, a self-pulsation signal can be triggered and stored in the closed loop configuration in response to an incoming signal, therefore, data buffering can be achieved in this recursive system, and the buffering time is determined by the length of the optical delay line. The optical signal from TLS2 with a wavelength close to the resonance wavelength of the ring resonator is modulated by a data sequence and injected into the optical buffer to provide the initial excitation of self-pulsation in the microring resonator. Without injection of the binary pulse sequence, the microring resonator operates in an unlocking regime without nonlinear self-oscillations being observed. Then, by modulating the injected optical signal with a sequence of data, the microring resonator starts to operate in the nonlinear self-oscillation regime if the incoming modulated data sequence has a sufficiently high energy. The first output pulse excited by the optical signal is fed back to the input (Port 1 shown in Fig. 1) after being delayed by a long delay time which initiates another self-pulsation pulse at the output. This recursive process results in a train of output pulses encoded by the modulated data sequence at a fixed interval determined by the length of the delay-line. We would like to highlight that the data sequence is successfully written after only a single roundtrip.

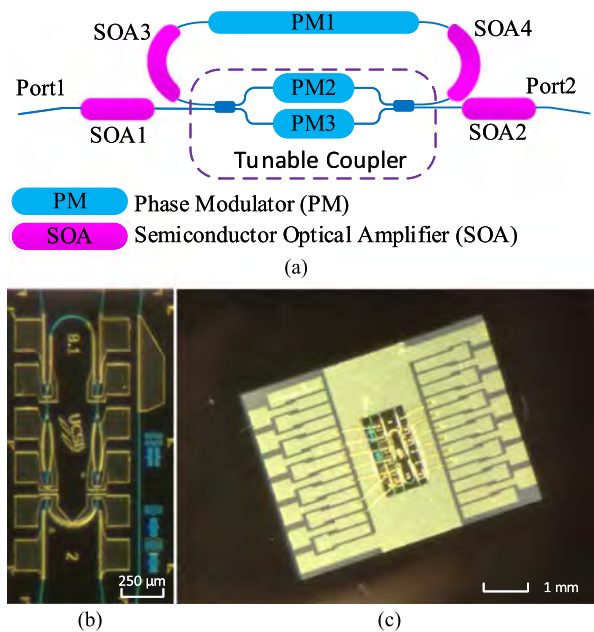


Fig. 2. (a) Schematic of the active microring resonator. (b) Fabricated microring resonator prototype (c) with wire bonding to a carrier.

The key component in the proposed optical buffer is the active microring resonator, as shown in Fig. 2(a), since it provides the nonlinear node of the buffering system. The output of which is coupled to a bus waveguide by a tunable coupler. Since the self-pulsation of the microring resonator can be triggered even with a strongly degraded pattern, the optical buffer is able to perform reshaping and restoring of a degraded data sequence. The tunable coupler is implemented by an MZI with a PM in each of the two arms. Two multimode interference couplers are used to combine and split optical power at the two ends of the MZI. By injecting a current to one of the two PMs, the coupling ratio of the tunable coupler can be tuned from 0 to 100%. There are also two semiconductor optical amplifiers (SOAs) at the input and output of the microring resonator to compensate for the coupling loss between the optical fiber and the resonator. Two additional SOAs are incorporated in the microring resonator to manage the insertion loss and thus achieve a high Q -factor. To achieve a tunable resonance wavelength, a PM is also incorporated inside the microring resonator. By changing the current injected into the PM, the resonance wavelength of the microring resonator can be laterally shifted. In this way, the designed microring resonator can provide an ultrahigh Q -factor and a tunable resonance wavelength. Since the resonance wavelength of the microring resonator is tunable due to the PM in the microring resonator, the incorporation of the active ring resonator in the proposed optical buffer would enable high speed and wavelength tunable optical data buffering.

III. EXPERIMENTAL RESULTS

The microring resonator is fabricated in an InP–InGaAsP material system, as shown in Fig. 2(b) and wire bonded to a carrier for easy accessing to the SOAs and PMs in the microring resonator, as shown in Fig. 2(c). The epitaxial structure for

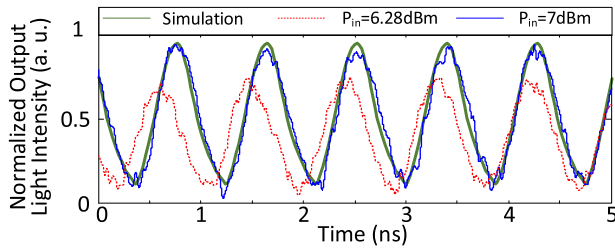


Fig. 3. Simulation and experimental results. Green solid line shows the simulation self-pulsation in the microring resonator. Red dashed line and blue solid line show the self-pulsation with a CW signal of 6.28 dBm and 7 dBm, respectively.

an SOA in the device includes an InP substrate, an n -dopant layer, a 300 nm waveguide layer, a ~ 250 nm confinement tuning layer (CTL), 5 quantum wells (QWs), a $1.7 \mu\text{m}$ Zn p -dopant layer, a 150 nm contact layer, and a metal layer. In such an epitaxial structure, the CTL pushes the QWs away from the waveguide layer to reduce the confinement factor and improve the saturation power. For a PM in the device, a p -dopant layer is grown on top of the waveguide layer without the CTL and QWs. For a passive waveguide, the contact layer is covered by a p -cap layer. In the InP–InGaAsP material system, heat can escape effectively [14], which would minimize the temperature increase due to the thermal effect. In addition, the device has a heterostructure, which allows the generated carriers to be confined in the InGaAsP region due to the band gap difference between the waveguide layer and the cladding layers. Therefore, a strong interplay between the carriers generated in the waveguide and the propagation light wave is obtained, which would enhance the self-pulsation effect. The length of the ring resonator is 3 mm, which provides a free spectral range (FSR) of 27.2 GHz or 0.22 nm at 1550 nm. The 3-dB bandwidth of the resonance notch is 22 pm, which is also tunable by tuning the gain in the ring resonator and the coupling coefficient between the ring resonator and the bus waveguide.

The self-pulsation in the fabricated microring resonator is first experimentally demonstrated. To do so, a CW light wave from a TLS (Agilent, N7714A) centered at 1558.775 nm is coupled into the microring resonator, which has a wavelength that is 25 pm apart from one of the resonance wavelengths of the microring resonator at 1558.8 nm. As shown in Fig. 3, a pulse train with a pulse width of 536.7 ps and a repetition rate of 1.12 GHz is generated when the input optical power is 7 dBm, which is close to the theoretically calculated pulse train by simulation with a free-carrier lifetime of 890 ps. Therefore, an on-off keying (OOK) data sequence with a rate less than 1.12 Gb/s can be used to trigger the self-pulsation in the ring resonator, meaning that the speed of the self-pulsation oscillations sets an upper limit of the bit rate that can be supported in the buffer. Due to the injection currents to the two SOAs inside the ring resonator, the insertion loss is largely compensated, which enables the resonator to have an ultrahigh Q -factor up to 31 million [19]. In the experiment, the Q -factor of the ring resonator is measured to be ~ 1 million, which is good enough to achieve effective self-pulsation. The pulse duration and magnitude can be slightly tuned by changing the input optical power [12]. When the input

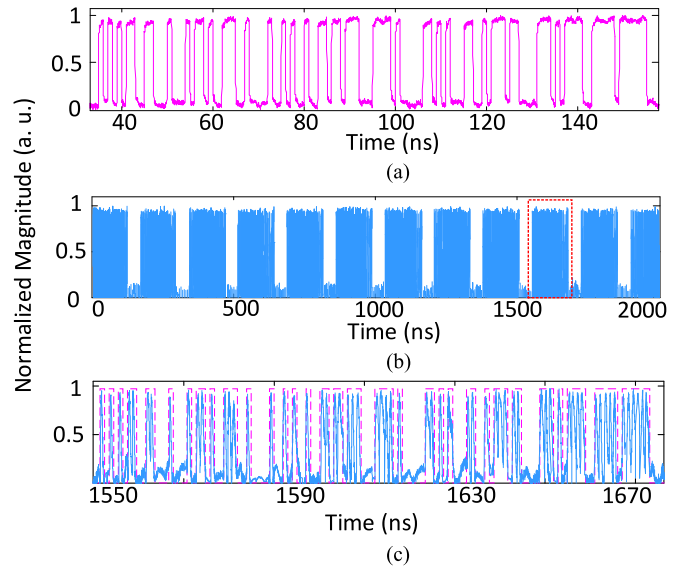


Fig. 4. Experimental results. (a) Input 1 Gb/s 2^7 -1 PRBS data sequence generated by an AWG. (b) Observed pulse train at the output of the optical buffer. (c) Solid line represents the detailed data sequence marked in (b) by a dashed box, and the dashed line represents the data used to generate the 2^7 -1 PRBS.

optical signal is tuned to 6.28 dBm, the pulse width is reduced to 583.6 ps, and the peak magnitude of the pulse is dropped by 20%. To ensure stable operation, a thermoelectric cooler is used to improve the temperature stability of the device and thus to achieve stable optical buffering. In the experiment, no drifting in the central wavelength of the ring resonator is observed after the system is warmed up which takes about 10 minutes.

In what follows, the experimental investigation of the incorporation of the active ring resonator in the proposed optical buffer, shown in Fig. 1, to achieve optical buffering is discussed. The output of the microring resonator is coupled to a 30-m optical delay line in the optoelectronic delayed feedback configuration to ensure a loop delay larger than the length of the input signal, where a TLS (TLS1, Anritsu, MG9638A), an MZM, the microring resonator, a PD (Newfocus, 25 GHz), and an electronic amplifier in addition to the 30-m optical delay line are used. The optical delay line loop can provide a buffering time of 172 ns. With a self-pulsation pulse repetition rate of 1.12 GHz, the proposed optical buffer can store a 2^7 -1 PRBS data sequence with a data rate of 1 Gb/s. The wavelength of the light wave from TLS1 is tuned at 1558.825 nm which is 25 pm apart from one of the resonance wavelengths of the microring resonator which is 1558.8 nm. A 1-Gb/s 2^7 -1 PRBS data sequence generated by an arbitrary waveform generator (Tektronix, AWG7102), shown in Fig. 4(a), is modulated on the light wave from TLS2 at 1558.775 nm with a power of 4 dBm, which is injected into the microring resonator through an optical circulator. The signal at the output of the optical buffer is observed by a real-time oscilloscope (Agilent DSO, X93204A), as shown in Fig. 4(b), and the signal is stored in the buffer for ~ 100 round trips. Due to the use of two SOAs in the ring resonator and an electrical amplifier in the system, the signal-to-noise ratio (SNR) is decreasing when the signal is recirculating in the loop. After a certain number of

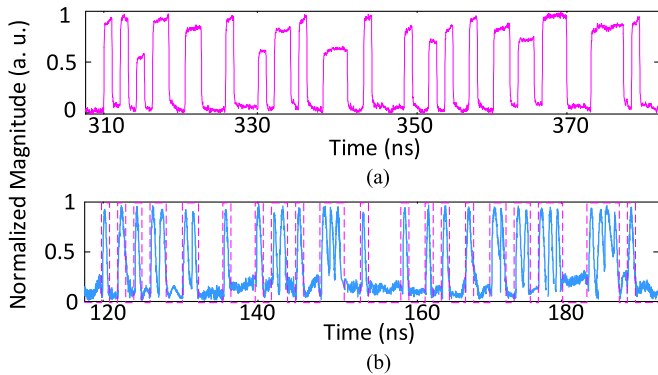


Fig. 5. Experimental results showing self-healing in the proposed optical buffer. (a) Input deteriorated 1 Gb/s data sequence generated by an AWG. (b) Solid line represents the observed pulse train in the optical buffer, and the dashed line represents the data used to generate the 2^7-1 PRBS.

round trips, the SNR will become too low and the signal may not be detected correctly. In Fig. 4(b), it can be seen that the buffering interval is 172 ns which is determined by the length of the optical delay line. Fig. 4(c) shows one of the buffered pulse sequences which carries the same data as those in the input optical signal. However, each buffered signal bit is a triggered self-pulsation pulse which has a fixed pulse shape determined by the self-pulsation instead of the input signal. This unique operation principle of an optical buffer based on self-pulsation limits its application in maintaining data format but enables new applications such as data recovery.

Since the self-pulsation has a fixed pulse shape, it can be used for data recovery. For a bit sequence where the amplitude of the bits is not evenly distributed, as shown in Fig. 5(a), the proposed system will also perform single-pass healing by restoring and self-adjusting the received bits to a fixed amplitude, as shown in Fig. 5(b). By using such an optical buffer, the bit error rate (BER) performance can be improved. In the experiment, a distorted signal as shown in Fig. 5(a) is modulated on an optical carrier and transmitted over a 25-km optical fiber with a BER of 7×10^{-3} at the receiver measured by a bit error rate tester (BERT, Agilent N4901B). By using the proposed optical buffer, an error free transmission ($\text{BER} < 10^{-13}$) of the recovered signal over the same optical fiber has been achieved. Therefore, the proposed optical buffer is insensitive (in a certain range) to the exact shape or amplitude of the addressing signal.

To demonstrate the data erasing functionality, a reversed data sequence, as shown in Fig. 6(a), which is synchronized with the pulse train in the optical buffer, is modulated on the light wave from TLS2 to reset the data in the optical buffer [20]. As shown in Fig. 6(b), the stored data in the optical buffer is erased. For the above mentioned operations of optical buffering, self-healing, and data erasing, the ring resonator is working under the same conditions with the injection currents given in Table I. An experiment to validate the wavelength tunability of the proposed optical buffer is also implemented. By changing the injection current of the PM in the ring, the notch location of the FSR is tuned as shown in Fig. 7(a), which enables the wavelength tunability of the optical buffer. For example, the optical buffering is validated when the wavelength of TLS2 is

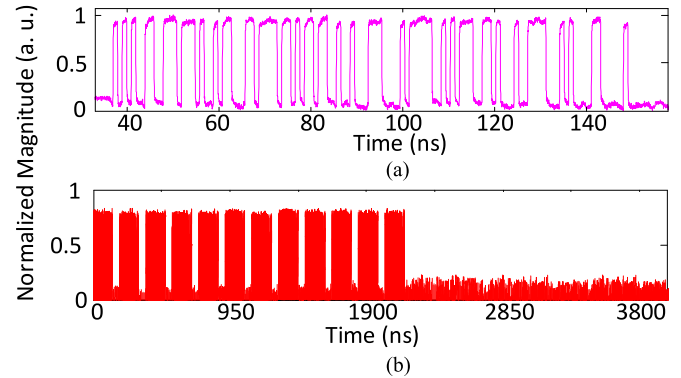


Fig. 6. Experimental results showing data erasing in the proposed optical buffer. (a) The reversed data sequence used to erase the stored data in the optical buffer. (b) Data erasing is observed when the reversed sequence is synchronized with the pulse train in the optical buffer and modulated on the optical wave from TLS2.

TABLE I
INJECTION CURRENTS OF THE SOAs AND THE PMs

Component	Injection Current	Gain
SOA1	24.904 mA	~ 3.6 dB
SOA2	24.952 mA	~ 3.6 dB
SOA3	19.583 mA	~ 1.1 dB
SOA4	19.654 mA	~ 1.1 dB
PM1	0.133 mA	N/A
PM2	0	N/A
PM3	1.325 mA	N/A

tuned to 1558.95 nm, 1559.0 nm, and 1559.05 nm as shown in Fig. 7(b), (c) and (d).

In the experiment, a 1-Gb/s 2^7-1 PRBS data sequence is successfully buffered in the proposed optical buffer, which is the fastest optical buffer ever reported based on self-pulsation in a microring resonator. The highest speed is limited by the speed of self-pulsation in the ring resonator, which sets the upper speed limit of writing two consecutive bits in the buffer. Nevertheless, microring resonators based on materials with a shorter free carrier lifetime can provide a higher speed [15], which opens up the possibility of even higher bit rates. The total power consumption of the microring resonator is 173 mW including 99 mW by the input/output SOAs (SOA1 and SOA2), which can be avoided in an integrated system where all units can be fabricated on a single chip; thus the fiber coupling loss for a ring resonator is eliminated. In this case, the total power consumption for such a ring resonator can be reduced to below 70 mW. For real applications, a single SOA in a ring resonator is enough to compensate for the total roundtrip loss. As a result, the total power consumption can be further reduced. In addition, the optical delay line can also be integrated in the chip [5], which can further reduce the foot print of the proposed optical buffer.

The ultrahigh- Q ring resonator can also be implemented in other material systems such as a SOI platform with III-V SOAs either bonded or grown on the silicon substrate to provide the required optical gains [21]. The silicon platform can provide more compact waveguide structures as compared with the

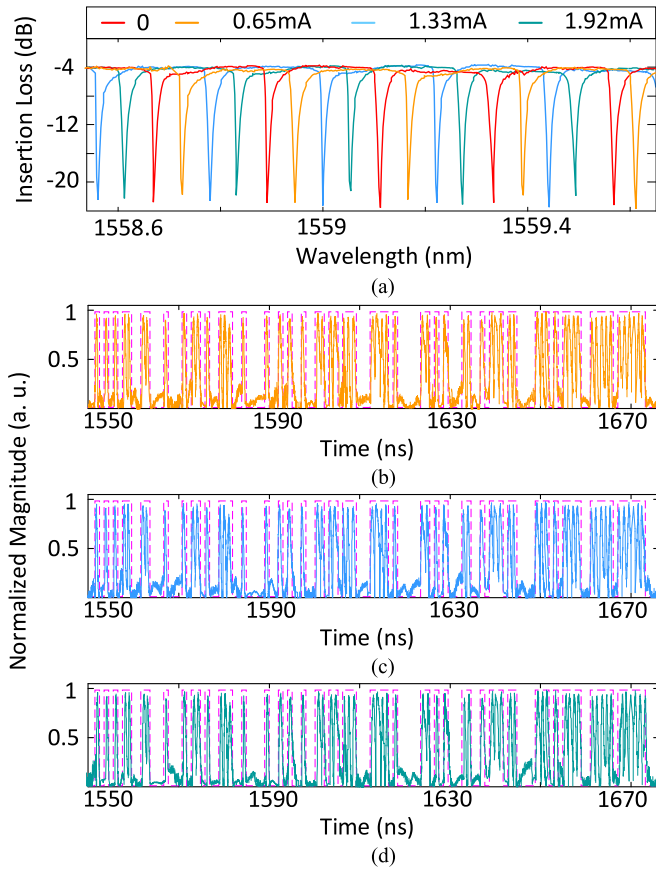


Fig. 7. Experimental results. (a) Tunable resonance wavelength of the microring resonator when different injection currents are applied to PM1. The solid line represents the data sequence in the optical buffer when the wavelength of TLS2 is tuned to (b) 1558.95 nm, (c) 1559.0 nm, and (d) 1559.05 nm, in which the injection currents applied to PM1 are 0.65 mA, 1.33 mA, and 1.92 mA, respectively. The dashed line represents the data used to generate the 2^7-1 PRBS.

III–V material system due to the large refractive index contrast between silicon and silica, which leads to a smaller foot print.

IV. CONCLUSION

We have proposed and experimentally demonstrated a novel wavelength tunable optical buffer based on self-pulsation in an active microring resonator that functions as a nonlinear node in the buffering system to enable writing, restoring, reshaping and regeneration (after a delay line) of stored bits of information. The key component in the proposed optical buffer is the active microring resonator. Since four SOAs were incorporated, the insertion losses can be effectively compensated, which ensures an ultrahigh Q factor to make the self-pulsation to be easily started. In addition, a PM was also incorporated in the ring resonator and by adjusting the injection current to the PM, the FSR of the ring resonator is laterally shifted, which was used to adjust a resonance wavelength close to the wavelength of the input optical signal, thus ensuring wavelength tunable optical buffering. The proposed microring resonator was fabricated in an InP–InGaAsP material system. The incorporation of the fabricated microring resonator in the proposed optical buffer was experimentally evaluated. By applying a 1-Gb/s optical data sequence

to the system, optical buffering of the sequence was experimentally demonstrated. This is, to the best of our knowledge, the fastest self-pulsation optical buffer ever reported to date. In addition, the use of the buffer system to perform data recovery and data erasing was also demonstrated. The proposed wavelength tunable optical buffer suggests high potential for fast optical storage and data healing in optical communications.

ACKNOWLEDGMENT

The authors would like to thank J. Javaloyes, University of Illes Balears, Spain, for the valuable discussions regarding signal buffering in nonlinear delayed systems.

REFERENCES

- [1] L. Tančevski, L. Tamil, and F. Callegati, “Nondegenerate buffers: An approach for building large optical memories,” *IEEE Photon. Technol. Lett.*, vol. 11, no. 8, pp. 1072–1074, Aug. 1999.
- [2] T. Tanemura, I. Murat Soganci, T. Oyama, T. Ohyama, S. Mino, K. A. Williams, N. Calabretta, H. J. S. Dorren, and Y. Nakano, “Large-capacity compact optical buffer based on InP integrated phased-array switch and coiled fiber delay lines,” *J. Lightw. Technol.*, vol. 29, no. 4, pp. 396–402, Dec. 2010.
- [3] A. E. Willner, S. Khaleghi, M. R. Chitgarha, and O. F. Yilmaz, “All-optical signal processing,” *J. Lightw. Technol.*, vol. 32, no. 4, pp. 660–680, Feb. 2014.
- [4] Y.-K. Yeo, J. Yu, and G.-K. Chang, “A dynamically reconfigurable folded-path time delay buffer for optical packet switching,” *IEEE Photon. Technol. Lett.*, vol. 16, no. 11, pp. 2559–2561, Dec. 2004.
- [5] H. Lee, T. Chen, J. Li, O. Painter, and K. J. Vahala, “Ultra-low-loss optical delay line on a silicon chip,” *Nature Commun.*, vol. 3, no. 867, pp. 1–7, May 2012.
- [6] A. H. Safavi-Naeini, T. P. M. Alegre, J. Chan, M. Eichenfield, M. Winger, Q. Lin, J. T. Hill, D. E. Chang, and O. Painter, “Electromagnetically induced transparency and slow light with optomechanics,” *Nature*, vol. 472, no. 7341, pp. 69–73, Mar. 2011.
- [7] H.-Y. Tseng, J. Huang, and A. Adibi, “Expansion of the relative time delay by switching between slow and fast light using coherent population oscillation with semiconductors,” *Appl. Phys. B*, vol. 85, no. 4, pp. 493–501, Oct. 2006.
- [8] K. Y. Song and K. Hotate, “25 GHz bandwidth Brillouin slow light in optical fibers,” *Opt. Lett.*, vol. 32, no. 3, pp. 217–219, Feb. 2007.
- [9] D. Dahan and G. Eisenstein, “Tunable all optical delay via slow and fast light propagation in a Raman assisted fiber optical parametric amplifier: A route to all optical buffering,” *Opt. Express*, vol. 13, no. 16, pp. 6234–6249, Aug. 2005.
- [10] H. Takesue, N. Matsuda, E. Kuramochi, W. J. Munro, and M. Notomi, “An on-chip coupled resonator optical waveguide single-photon buffer,” *Nature Commun.*, vol. 4, no. 2725, pp. 1–7, Nov. 2013.
- [11] F. Leo, S. Coen, P. Kockaert, S.-P. Gorza, P. Emplit, and M. Haelterman, “Temporal cavity solitons in one-dimensional Kerr media as bits in an all-optical buffer,” *Nature Photon.*, vol. 4, no. 5, pp. 471–476, May 2010.
- [12] T. Van Vaerenbergh, M. Fiers, P. Mechet, T. Spuesens, R. Kumar, G. Morthier, B. Schrauwen, J. Dambre, and P. Bienstman, “Cascadable excitability in microrings,” *Opt. Express*, vol. 20, no. 18, pp. 20292–20308, Aug. 2012.
- [13] T. Van Vaerenbergh, M. Fiers, J. Dambre, and P. Bienstman, “An optical delayline based on excitable microrings,” in *Proc. IEEE Photon. Conf.*, Oct. 12–16, 2014, pp. 118–119.
- [14] K. Nozaki, A. Shinya, S. Matsuo, Y. Suzuki, T. Segawa, T. Sato, Y. Kawaguchi, R. Takahashi, and M. Notomi, “Ultralow-power all-optical RAM based on nanocavities,” *Nature Photon.*, vol. 6, pp. 248–252, Feb. 2012.
- [15] M. Soltani, S. Yegnanarayanan, Q. Li, A. A. Eftekhari, and A. Adibi, “Self-sustained gigahertz electronic oscillations in ultrahigh- Q photonic microresonators,” *Phys. Rev. A*, vol. 85, no. 5, pp. 1–5, May 2012.
- [16] N. Cazier, X. Checoury, L.-D. Haret, and P. Boucaud, “High-frequency self-induced oscillations in a silicon nanocavity,” *Opt. Express*, vol. 21, no. 11, pp. 13626–13638, May 2013.
- [17] S. Malaguti, G. Bellanca, A. de Rossi, S. Combré, and S. Trillo, “Self-pulsing driven by two-photon absorption in semiconductor nanocavities,” *Phys. Rev. A*, vol. 83, no. 5, pp. 051802-1–051802-4, May 2011.

- [18] K. Ikeda and O. Akimoto, "Instability leading to periodic and chaotic self-pulsations in a bistable optical cavity," *Phys. Rev. Lett.*, vol. 48, no. 9, pp. 617–620, Mar. 1982.
- [19] W. Liu *et al.*, "Photonic temporal integrator with an ultra-long integration time window based on an InP-InGaAsP integrated ring resonator," *J. Lightw. Technol.*, vol. 32, no. 20, pp. 3654–3659, Oct. 2014.
- [20] B. Garbin, J. Javaloyes, G. Tissoni, and S. Barland, "Topological solitons as addressable phase bits in a driven laser," *Nature Commun.*, vol. 6, no. 5915, pp. 1–7, Nov. 2014.
- [21] Z. Wang, B. Tian, M. Pantouvaki, W. Guo, P. Absil, J. Van Campenhout, C. Merckling, and D. Van Thourhout, "Room-temperature InP distributed feedback laser array directly grown on silicon," *Nature Photon.*, vol. 9, no. 10, pp. 837–842, Oct. 2015.

Weilin Liu (S'10) received the B.Eng. degree in electronic information engineering from the University of Science and Technology of China, Hefei, China, in 2009, and the M.A.Sc. degree in electrical and computer engineering from the School of Electrical Engineering and Computer Science, University of Ottawa, Ottawa, ON, Canada, in 2011.

He is currently working toward the Ph.D. degree at the Microwave Photonics Research Laboratory, School of Electrical Engineering and Computer Science, University of Ottawa, Ottawa. His research interests include microwave/terahertz generation, optical signal processing, fiber Bragg grating and their applications in microwave photonic systems.

Bruno Romeira (M'13) received the five-year Diploma degree in physics and chemistry from the University of the Algarve, Faro, Portugal, in 2006, and the Ph.D. degree in physics (*summa cum laude*) and the title of European Ph.D. from the same university, jointly with the University of Glasgow, Glasgow, U.K., and the University of Seville, Seville, Spain, in 2012. He was then engaged in a postdoctoral fellowship at the same university and at the Microwave Photonics Research Laboratory, University of Ottawa, Canada. He is currently a Marie Skłodowska-Curie Research Fellow at the Applied Physics Department, Eindhoven University of Technology, Eindhoven, The Netherlands. His research interests include semiconductor physics, nonlinear dynamics and solid-state optoelectronic and photonic devices. He is currently devoted to the theoretical and experimental investigation of the dynamics of nanolasers.

Dr. Romeira received the Young Researchers Incentive Programme Award from the Calouste Gulbenkian Foundation, Portugal, in 2009, and the IEEE Photonics Society Graduate Student Fellowship from the IEEE Photonics Society, USA, in 2011. His Ph.D. thesis entitled "Dynamics of Resonant Tunneling Diode Optoelectronic Oscillators" received the Best Ph.D. Thesis in Optics and Photonics in Portugal in 2012 by the Portuguese Society of Optics and Photonics.

Ming Li (S'08–M'09) received the Ph.D. degree in electrical and electronics engineering from the University of Shizuoka, Hamamatsu, Japan, in 2009.

In April 2009, he joined the Microwave Photonics Research Laboratory, School of Electrical Engineering and Computer Science, University of Ottawa, Ottawa, ON, Canada, as a Postdoctoral Research Fellow. In June 2011, he joined the Ultrafast Optical Processing Group, INRS-EMT, Montreal, Canada, as a Postdoctoral Research Fellow. In February 2013, he successfully got a high-level government-funded program ("Thousand Young Talents" program) in China. And then, he joined the Institute of Semiconductor, Chinese Academy of Sciences as a Full Professor. He has published more than 110 international conference and top-level journal papers. His current research interests include advanced FBGs and their applications to microwave photonics, ultrafast optical signal processing, arbitrary waveform generation, and optical MEMS sensing.

Robert S. Guzzon received the Ph.D. degree in electrical engineering from the University of California, Santa Barbara, CA, USA, in 2011 (where this work was performed). At the same university, he developed high dynamic range photonic integrated microwave filter systems, and investigated the spurious free dynamic range of amplified optical systems. He is currently working at the Aurrion, Inc., Goleta, CA, on silicon photonic systems.

Erik J. Norberg received the Ph.D. degree in electrical engineering from the University of California, Santa Barbara (UCSB) in 2011 (where this work was performed). At UCSB, he developed integrated photonic microwave filters and a high dynamic range integration platform on InP. He is author/co-author of more than 30 papers.

He is currently an Optoelectronic Design Engineer at the Aurrion Inc., Goleta, CA, USA.

John S. Parker received the Ph.D. degree in electrical engineering from the University of California, Santa Barbara, CA, USA, in 2012 (where this work was performed). At UCSB, he developed integrated photonic frequency combs with optical PLLs for sensing and coherent communication. He is currently a Photonic Device Scientist at Freedom Photonics, Santa Barbara, CA.

Larry A. Coldren (S'67–M'72–SM'77–F'82–LF'12) received the Ph.D. degree in electrical engineering from the Stanford University, Stanford, CA, USA, in 1972.

He is currently a Fred Kavli Professor of Optoelectronics and Sensors at the University of California at Santa Barbara (UCSB), Santa Barbara, CA, USA. For 13 years, he worked with the Bell Laboratories prior to joining UCSB, in 1984, where he holds appointments in electrical and computer engineering and materials. He cofounded Optical Concepts (acquired as Gore Photonics), to develop novel vertical-cavity surface-emitting laser (VCSEL) technology, and later Agility Communications (acquired by JDSU), to develop widely tunable integrated transmitters. With Bell Laboratories, he was involved with surface acoustic wave (SAW) filters and tunable coupled-cavity lasers using novel reactive ion etching (RIE) technology. With UCSB, he has continued his involvement on multiple-section lasers, in 1988 inventing the widely tunable multi-element mirror concept that is now used in numerous commercial products. He has also made seminal contributions to efficient VCSEL designs. His group continues efforts on high-performance InP-based PICs and high-speed VCSELs. He has authored or coauthored more than 1000 journal and conference papers, a number of book chapters, and a textbook. He holds 64 patents.

Dr. Coldren is a Fellow of Optical Society of America and the Institution of Electrical Engineers. He is a Member of the National Academy of Engineering. He received the John Tyndall Award in 2004 and the Aron Kressel Award in 2009.

Jianping Yao (M'99–SM'01–F'12) received the Ph.D. degree in electrical engineering from the Université de Toulon et du Var, France, in December 1997. From 1998 to 2001, he was with the School of Electrical and Electronic Engineering, Nanyang Technological University, Singapore. In December 2001, he joined the School of Electrical Engineering and Computer Science, University of Ottawa, as an Assistant Professor, where he became an Associate Professor in 2003, and a Full Professor in 2006. He was appointed the University Research Chair in Microwave Photonics in 2007. From July 2007 to June 2010, he was the Director of the Ottawa-Carleton Institute for Electrical and Computer Engineering. He was re-appointed as the Director of the Ottawa-Carleton Institute for Electrical and Computer Engineering in 2013. He is a Professor and University Research Chair at the School of Electrical Engineering and Computer Science, University of Ottawa, Ottawa, Ontario, Canada.

He has authored or co-authored more than 510 research papers, including more than 300 papers in peer-reviewed journals and 210 papers in conference proceedings. He is the Topical Editor for *the Optics Letters*, and serves on the Editorial Boards of the IEEE TRANSACTIONS ON MICROWAVE THEORY AND TECHNIQUES, *the Optics Communications*, *the Frontiers of Optoelectronics*, and *the Science Bulletin*. He was as a Guest Co-editor for a Focus Issue on Microwave Photonics in *Optics Express* in 2013 and a Lead-editor for a Feature Issue on Microwave Photonics in *Photonics Research* in 2014. He is the Chair of numerous international conferences, symposia, and workshops, including the Vice Technical Program Committee (TPC) Chair of the IEEE Microwave Photonics Conference in 2007, the TPC Co-Chair of the Asia-Pacific Microwave Photonics Conference in 2009 and 2010, the TPC Chair of the high-speed and broadband wireless technologies subcommittee of the IEEE Radio Wireless Symposium in 2009–2012, the TPC Chair of the microwave photonics subcommittee of the IEEE Photonics Society Annual Meeting in 2009, the TPC Chair of the IEEE Microwave Photonics Conference in 2010, General Co-Chair of the IEEE Microwave Photonics Conference in 2011, the TPC Co-Chair of the IEEE Microwave Photonics Conference in 2014, and the General Co-Chair of the IEEE Microwave Photonics Conference in 2015. He is also a Committee Member of numerous international conferences, such as IPC, OFC, BGPP, and MWP. He received the 2005 International Creative Research Award of the University of Ottawa. He received the 2007 George S. Glinski Award for Excellence in Research. In 2008, he received the Natural Sciences and Engineering Research Council of Canada Discovery Accelerator Supplements Award. He was selected to receive an inaugural OSA Outstanding Reviewer Award in 2012. He is currently an IEEE MTT-S Distinguished Microwave Lecturer for 2013–2015.

Prof. Yao is a registered Professional Engineer of Ontario. He is a Fellow of the Optical Society of America (OSA) and the Canadian Academy of Engineering.